WDL-TR2623
15 October 1965

THE FEASIBILITY OF A PROGRAMMED HEAT SHIELD FOR SOLAR CELL PERFORMANCE CONTROL

by

Michael W. Cobb, W. Scott Cummings, and John W. Fairbanks

Contract NAS 2-2564

Submitted to

National Aeronautics and Space Administration
Ames Research Center
Moffett Field, California

WDL-TR2623
October 15, 1965

THE FEASIBILITY OF A PROGRAMMED HEAT SHIELD FOR SOLAR CELL PERFORMANCE CONTROL

Prepared by

PHILCO CORPORATION
A Subsidiary of Ford Motor Company
WDL Division
Palo Alto, California

by

Michael W. Cobb, W. Scott Cummings, and John W. Fairbanks

Contract NAS 2-2564

Submitted to

National Aeronautics and Space Administration
Ames Research Center
Moffett Field, California

ABSTRACT

PHILCO WDL-TR2623 UNCLASSIFIED
THE FEASIBILITY OF A PROGRAMMED HEAT SHIELD FOR SOLAR CELL PERFORMANCE CONTROL 75 Pages
15 October 1965 N67-17867 NAS 2-2564

An analytical study has been performed on the feasibility of using a positionable despun thermal shield to control the temperature and power of a solar array used for spacecraft on-board power during a 0.2 AU mission. The results of the study indicate that such a mission is feasible using body-mounted N/P silicon solar cells with blue-red full-cell-response bandwidth filters. A cylindrical spacecraft with a Pioneer configuration, spinning about its centerline at 60 RPM, was used in the study; the thermal shield consisted of two counter-rotating cylindrical surfaces with a radius only slightly larger than the spacecraft and rotating about the spacecraft spin axis. A minimum power output of 60 watts was maintained; the maximum temperature of the solar array was 190°F at 0.2 AU.

Author

FOREWORD

This report was prepared by the Philco WDL Thermal Technology Section in partial fulfillment of the requirements of Contract NAS 2-2564. It satisfies the requirements of the revised contract work statement for Phase II.

Some of the information contained herein is in addition to the statement of work for the contract. This information, pertaining to the area of solar array power generation, has been included in the interest of a complete and thorough presentation.

TABLE OF CONTENTS

TABLE OF CONTENTS - Continued

LIST OF ILLUSTRATIONS

LIST OF ILLUSTRATIONS - Continued

LIST OF TABLES

SUMMARY

An analytical study has been performed to determine the feasibility of using a positionable despun thermal shield to control the temperature and power of a solar array used for spacecraft on-board power during a 0.2 AU mission. The results of the study indicate that such a mission is feasible using body-mounted N/P silicon solar cells with blue-red full-cell-response bandwidth filters.

A cylindrical spacecraft with a Pioneer configuration, spinning about its axis at 60 RPM, was used in the study; the selected thermal shield consisted of two counter-rotating cylindrical surfaces with a radius only slightly larger than the spacecraft and rotating about the spacecraft spin axis.

Solar array temperature, thermal shield temperature, and system power output are given as a function of shield position and solar distance for N/P silicon solar cells with three different filters. Voltage-current curves are given as a function of solar distance for each cell-filter combination.

It is shown that the required power generation level of 60 watts can be maintained throughout the mission. With the solar shield opening programmed to optimize power, a minimum power of 72 watts is available at 1.0 AU and a maximum power of 325 watts obtains at 0.2 AU. The solar array reaches a maximum temperature of 88°C (190°F) at 0.2 AU.

Both the cell and the filter selected on the basis of this study are production items available at relatively low cost.

NOMENCLATURE

Symbols

A	Area
A_p	Projected Area
h	Axial Dimension of Cylindrical Spacecraft
I	Current
k	Thermal Conductivity
P	Power
q	Heat Flux
R	Thermal Resistance
r	Radius of Cylindrical Spacecraft
r_λ	Solar Cell Spectral Response
S	Solar Constant
T	Temperature
V	Voltage
Z	Solar Cell Packing Factor
α	Absorptance
ϵ	Emissivity
η	Efficiency
2θ	Shield Angle
λ	Wavelength
ρ	Reflectivity
σ	Stefan-Boltzmann Constant $= 0.1714 \times 10^{-8}$ Btu/hr ft^2 $^\circ$R^4
τ_λ	Filter Spectral Transmittance

Subscripts

i,j	Numerical subscripts refer to specific nodes or cases used in the analysis.
S	Solar
λ	Denotes spectral dependence.

1.0 INTRODUCTION

Near solar space probe missions are desirable for the purpose of collecting needed scientific data. However, during such a mission, spacecraft temperatures will be high.

Solar cells are the conventional power source for extended space missions. However, solar cells do not operate efficiently at high temperatures -- in fact, they have a temperature limit beyond which no power is produced.

The purpose of the present investigation is to determine the feasibility of extending the useful range of solar cells to include near solar missions. The suggested means for accomplishing this end -- a close-mounted despun heat shield -- is applicable only to a spinning spacecraft with body-mounted cells.

The feasibility of this technique will be established on the basis of the results of a combined thermal and photovoltaic analysis. This analysis will consider a spinning cylindrical spacecraft with a Pioneer configuration. Solar array temperature, thermal shield temperature, and system power output will be predicted as a function of shield position and solar distance; voltage-current curves will be estimated as a function of solar distance.

2.0 PROBLEM DEFINITION

A detailed problem statement is given below, including a description of the system and the requirements of the study.

2.1 PROBLEM STATEMENT

The purpose of this study is to analytically determine the feasibility and operating characteristics of a programmed, despun, heat shield positioned around the periphery of a spacecraft to control the electrical performance of a solar cell power system designed for operation on a 0.20 AU perihelion trajectory. The highly reflective and thermally insulated shield is to be actively positioned on the solar irradiated side of the spacecraft to maintain a proper balance between the average temperature and effective solar illumination of the solar cell array to continuously provide about 60 watts of electrical power to the spacecraft.

Nominal dimensions of the solar cell covered cylindrical spacecraft are 36 inches in diameter by 30 inches in length. The cylindrical surface is spinning at 60 $\pm$10 RPM and is normal to the incident solar radiation at all times during flight. The spacecraft/shield system is illustrated in Figure 2-1.

A description of the physical, thermal, and electrical characteristics of a spacecraft power system for the stated conditions and mission is to be provided. Specific results for solar distances of 1.0, 0.4, and 0.2 AU are required.

Details of the system analyzed in this study are described below. Assumptions, performance characteristics, and physical properties are as specified by NASA Ames in the re-defined work statement for contract NAS 2-2564.

FIGURE 2-1

SCHEMATIC OF SPACECRAFT/SHIELD SYSTEM

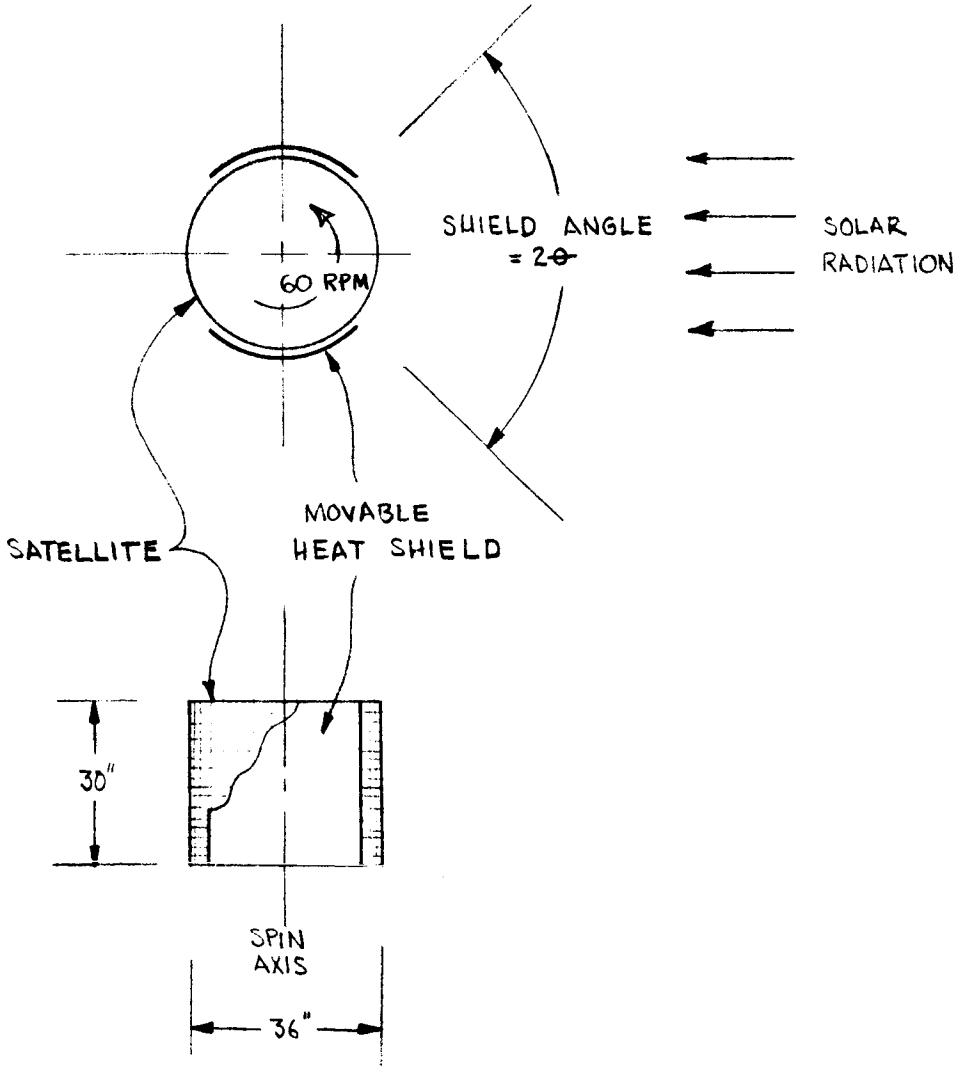

(a) Heat Shield

The thermal shield will consist of a non-magnetic framework supporting a typical 1/4-inch thick multilayer insulation blanket. The properties of the insulation will be:

$$\text{density} = 5\ \text{lb/ft}^3$$
$$\text{thermal cond.} = 0.005\ \text{Btu/hr} \cdot \text{ft} \cdot (^{\circ}\text{F/in})$$

The shield will be bearing supported at one end and will rotate independently of, but parallel to, the spacecraft cylindrical axis.

Surface properties of the shield will be:

- Externally exposed surface (space side)

$$\left.\begin{aligned} \alpha_S &= 0.10 \\ \epsilon_H &= 0.80 \end{aligned}\right\} \quad 70\ ^{\circ}\text{F} \le T \le 500^{\circ}\text{F}$$

- Surfaces facing spacecraft

$$\epsilon_H = 0.05$$

The shield is to be considered thermally isolated from the spacecraft, excepting radiation coupling.

(b) Solar Cell Power Supply

The solar cell array is thermally isolated from the spacecraft structure. A total of 10,368 silicon solar cells are arranged uniformly on the cylindrical surface of the vehicle. They are connected in 48 strings of 4 (parallel) x 54 (series) cells. All 54 cells of a given series will be in a single line parallel to the vehicle axis. Both N/P silicon and gallium arsenide solar cells will be considered.

The study is to include, but is not limited to, 6 mil fused silica cover glasses with 0.4 - 1.1 micron interference filters. Degradation effects of ultraviolet and penetrating radiation are of interest, but are not to be considered at the expense of stated requirements for the study.

2.2 REQUIREMENTS

The requirements of the study, as specified by the contract, are the following:

(a) Determine the feasibility of the proposed heat shield, as described above.

(b) Determine the physical characteristics of the heat shield.

(c) Predict temperatures of the solar cells and the heat shield as a function of shield position and solar distance -- specifically, for 0.2, 0.4, and 1.0 AU.

(d) Investigate the influence of incident solar angle, shield position, and spacecraft spin direction on solar cell temperature profiles. The interaction of reflected or trapped solar radiation should be considered.

(e) Characterize solar cell current-voltage as a function of solar flux, temperature, and shield position.

(f) Determine a shield position program to maintain solar array output at 60 watts and 24-33 volts between 1.0 and 0.2 AU (or the closest solar approach for which these values can be maintained).

(g) Determine maximum power level and voltage attainable at 0.2 AU keeping within stated levels at 1.0 AU. Report shield programs for these cases.

3.0 THERMAL ANALYSIS

A general thermal analysis of the spacecraft/shield system was performed for the purpose of establishing temperature levels and ranges. The resulting thermal model is also used in the detailed analysis of the power system (Section 6.0). The thermal analysis treats both spacecraft and shield as isothermal; this assumption is shown to be valid for the spacecraft by considering the effect of its spin rate. Radial and circumferential gradients in the shield are also considered; as a result, the analysis is shown to be conservative.

3.1 ANALYSIS

Both spacecraft and shield are assumed to be isothermal in the thermal analysis which follows. Figure 3-1 is a schematic description of the thermal model. The following assumptions were made in the development of the thermal model:

(i) The heat shield is attached to the spacecraft by a thermally nonconducting support.

(ii) The shield may be interposed between the spacecraft and the sun to any extent desired.

(iii) Both spacecraft and shield are isothermal bodies.

(iv) The shield is mounted in close proximity to the spacecraft.

(v) The total surface area of the shield is equal to the area of the cylindrical surface of revolution of the spacecraft.

(vi) The solar absorptance of any surface is independent of the incidence angle of the solar vector.

(vii) The effective temperature of deep space is absolute zero.

FIGURE 3-1

SPACECRAFT AND SHIELD
SCHEMATIC OF THERMAL MODEL

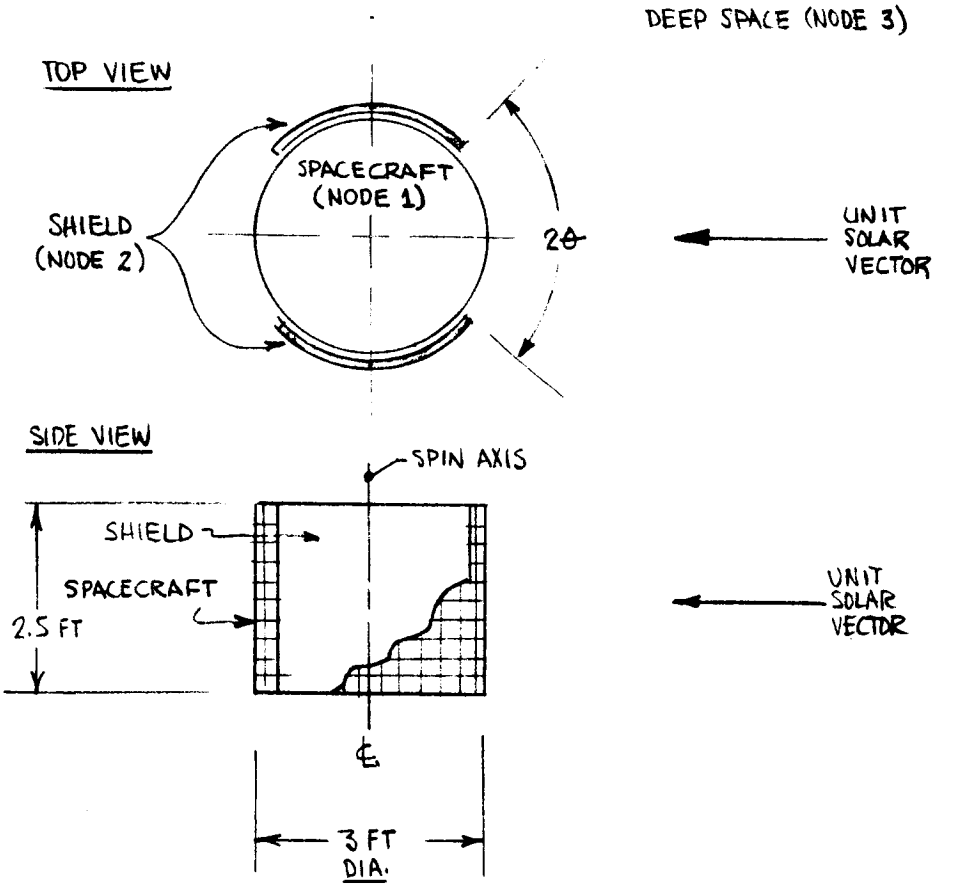

The solar energy absorbed by node i is

$$q_{si} = A_{pi} S_d \alpha_{si} \qquad (3\text{-}1)$$

where

A_{pi} = projected area of node i as seen by the sun

= 2rh sin θ for node 1, the spacecraft

= 2rh (1 - sin θ) for node 2, the shield.

S_d = solar contant at distance d from the sun

= 442 Btu/hr · ft^2 at 1 AU

= 2760 Btu/hr · ft^2 at 0.4 AU

= 11000 Btu/hr · ft^2 at 0.2 AU

α_{Si} = solar absorptance of node i

The equivalent thermal resistance network for this system is shown below

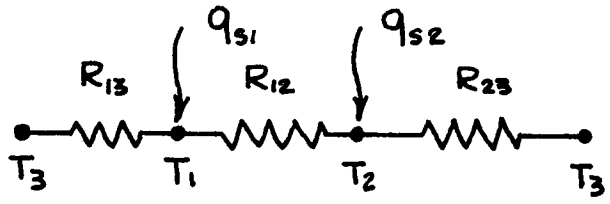

where

T_1 = temperature of spacecraft

T_2 = temperature of shield

R_{13} = radiation resistance from the spacecraft to space

R_{12} = radiation resistance from the spacecraft to the shield

R_{23} = radiation resistance from the shield to space.

T_1 and T_2 are desired as functions of the shield angle (2θ), the solar distance, and the surface properties of the spacecraft and shield. The analysis yielding this result is given in Appendix A; the resulting equations are:

$$\sigma T_2^4 = \frac{\epsilon_E A q_{S1} + \left[A(\epsilon_{13} + \epsilon_E) + \epsilon'_{13} A'\right] q_{S2}}{A\left\{A\left[\epsilon_E(\epsilon_{13} + \epsilon_{23}) + \epsilon_{13}\epsilon_{23}\right] + \epsilon'_{13} A'(\epsilon_E + \epsilon_{23})\right\}} \qquad (3\text{-}2)$$

$$\sigma T_1^4 = \frac{(\epsilon_E + \epsilon_{23}) A \sigma T_2^4 - q_{S2}}{\epsilon_E A} \qquad (3\text{-}3)$$

where:

$\epsilon_E = \left[\frac{1}{\epsilon_1} + \frac{1}{\epsilon_2} - 1\right]^{-1}$ = effective emittance between nodes 1 and 2.

ϵ_{ij} = emittance of that portion of A_i that "sees" node j.

ϵ'_{13} = emittance of ends of cylinder.

$A = \pi rh$ = one-half the area of the cylindrical surface of revolution. Also, either surface of the shield.

$A' = 2\pi r^2$ = total area of the ends of the cylinders.

Temperatures for the spacecraft and shield were evaluated using equations 3-2 and 3-3. The cases considered are tabulated below; cases I and II include a top and bottom surface for the cylinder, while cases III and IV assume no top or bottom surface.

Case No.	Total Spacecraft Radiative Area	Solar Cell - Filter Combination Solar Absorptance
I	$2\pi r(r + h)$	0.56
II	$2\pi r(r + h)$	0.20
III	$2\pi rh$	0.56
IV	$2\pi rh$	0.20

The following surface properties are common to all cases:

$\epsilon_{13} = \epsilon_{12} = 0.875$ (solar cells with 0.4 to 1.1 μ filters).

$\epsilon'_{13} = 0.875$ (arbitrarily taken equal to ϵ_{13})

$\left.\begin{aligned} \epsilon_{21} &= 0.05 \\ \epsilon_{23} &= 0.80 \\ \alpha &= 0.10 \end{aligned}\right\}$ (as defined in contract)

Calculated quantities are:

$\epsilon_E = 0.0496$

$A = \pi rh = 11.78 \text{ ft}^2$

$A' = 2\pi r^2 = 14.14 \text{ ft}^2$ (cases I and II)

$A' = 0$ (cases III and IV).

The results of this analysis are presented graphically in Figures 3-2, 3-3, 3-4, and 3-5.

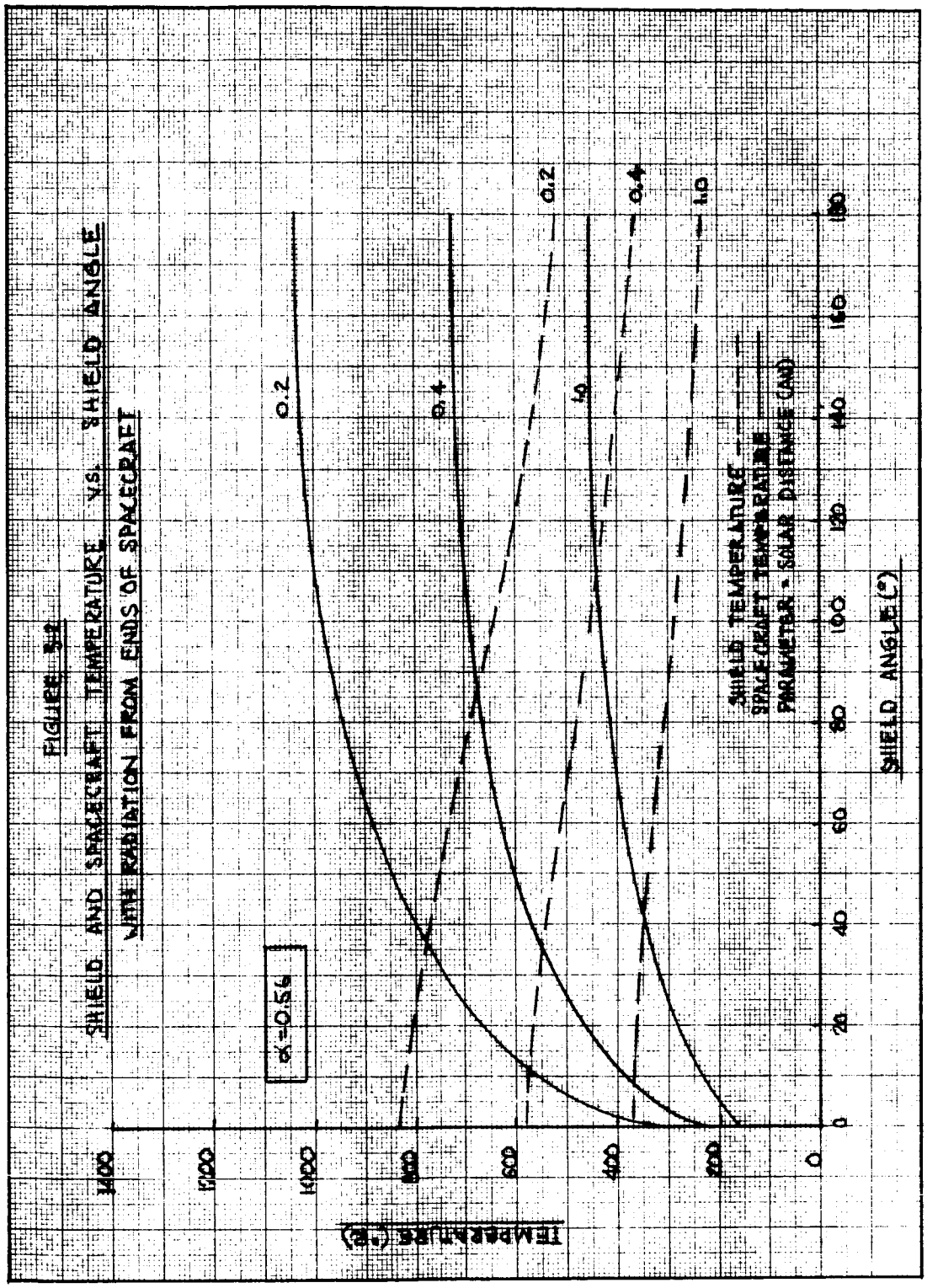
FIGURE 3-2
SHIELD AND SPACECRAFT TEMPERATURE VS. SHIELD ANGLE
WITH RADIATION FROM ENDS OF SPACECRAFT
α=0.56
0.2
0.4
1.0
0.2
0.4
1.0
SHIELD TEMPERATURE
SPACECRAFT TEMPERATURE
PARAMETER - SOLAR DISTANCE (AU)
TEMPERATURE (°R)
SHIELD ANGLE (°)
1400
1200
1000
800
600
400
200
0
0
20
40
60
80
100
120
140
160
180

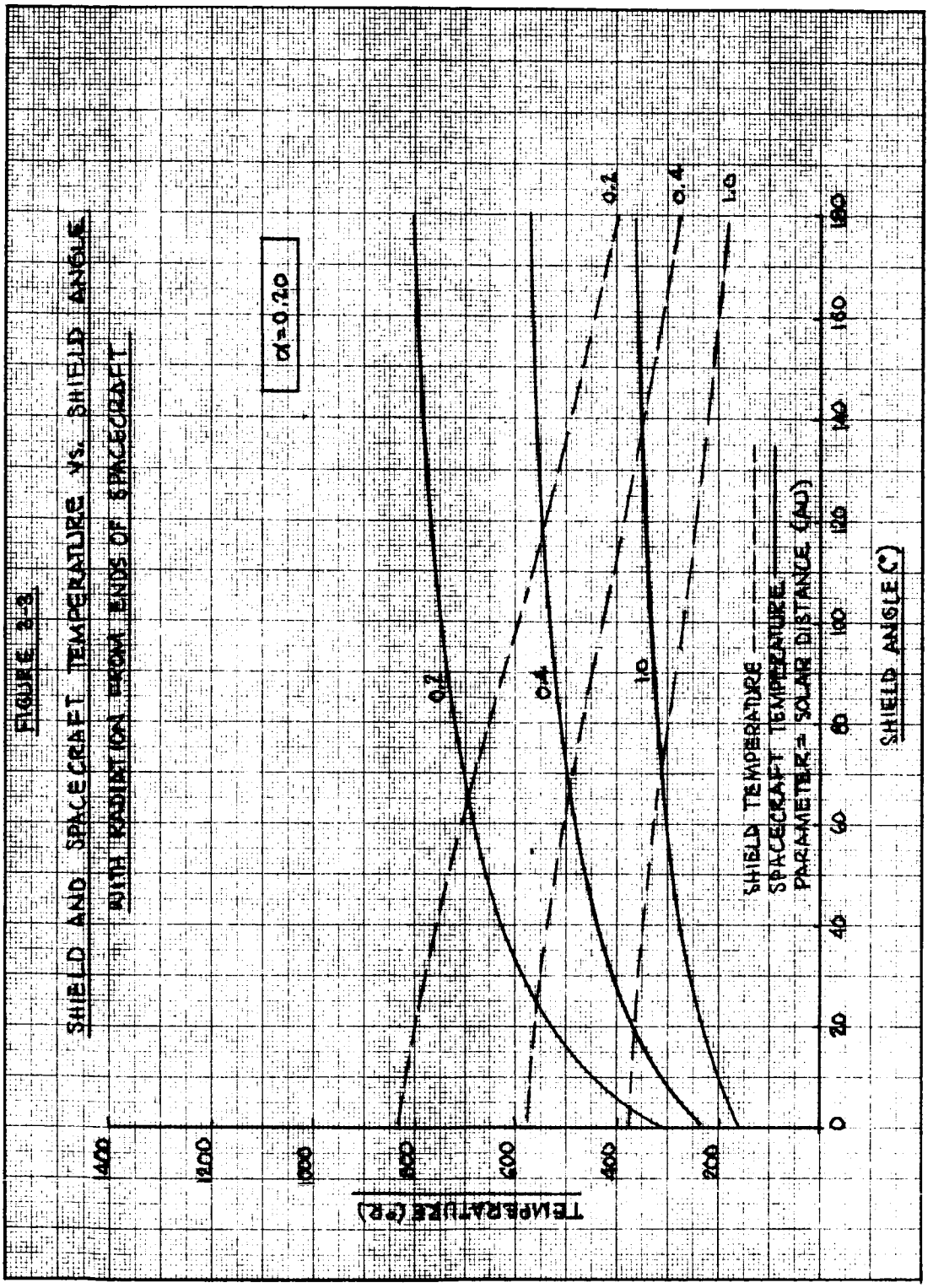
FIGURE 3-3
SHIELD AND SPACECRAFT TEMPERATURE VS. SHIELD ANGLE
WITH RADIATION FROM ENDS OF SPACECRAFT
α=0.20
TEMPERATURE (°R)
1400
1200
1000
800
600
400
200
0.2
0.4
1.0
SHIELD TEMPERATURE
SPACECRAFT TEMPERATURE
PARAMETER = SOLAR DISTANCE (AU)
0
20
40
60
80
100
120
140
160
180
SHIELD ANGLE (°)

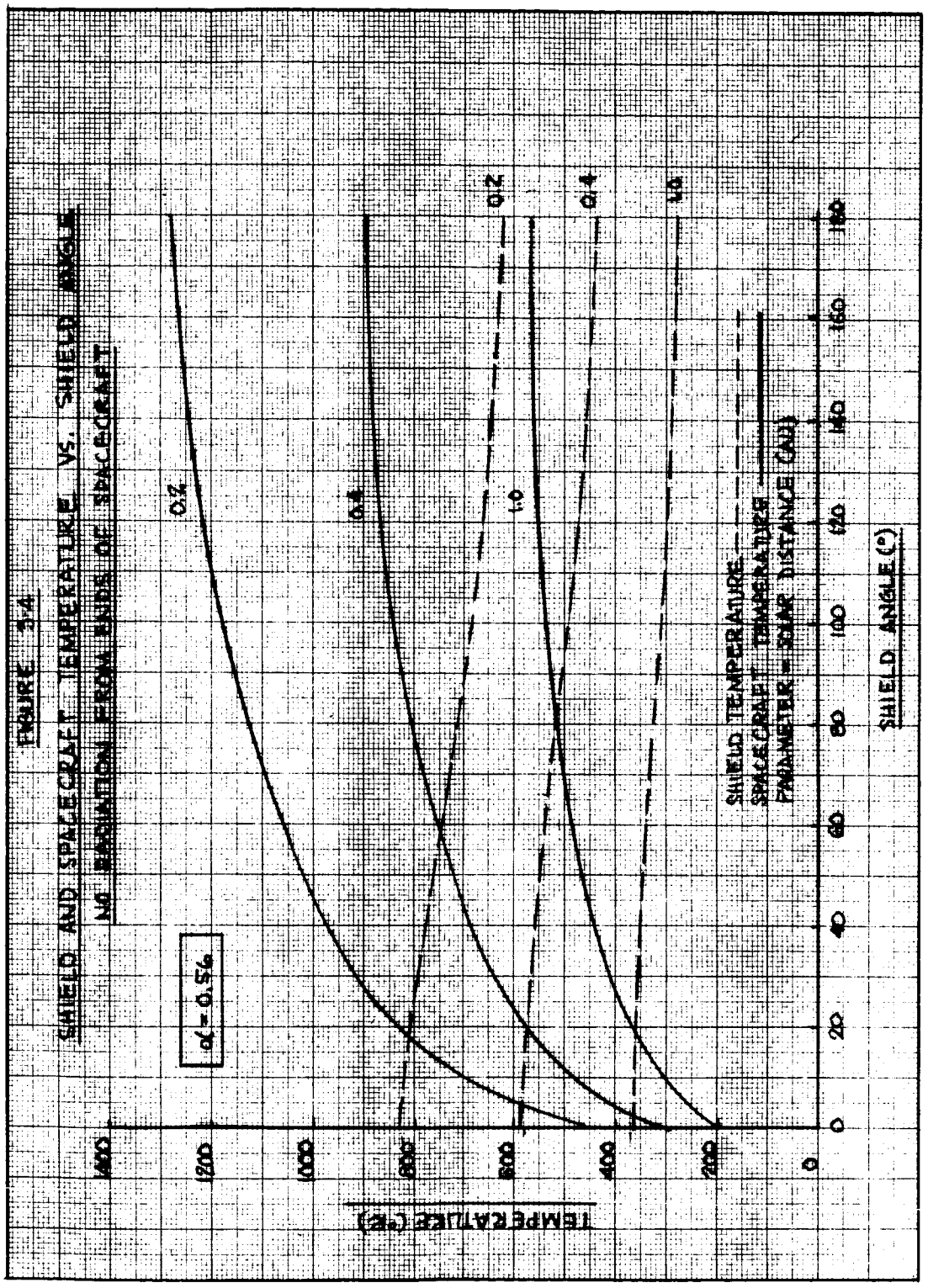
FIGURE 3-4
SHIELD AND SPACECRAFT TEMPERATURE VS. SHIELD ANGLE
NO RADIATION FROM ENDS OF SPACECRAFT
α = 0.5
0.2
0.4
1.0
0.2
0.4
1.0
SHIELD TEMPERATURE
SPACECRAFT TEMPERATURE
PARAMETER - SOLAR DISTANCE (AU)
TEMPERATURE (°R)
SHIELD ANGLE (°)
0
200
400
600
800
1000
1200
1400
0
20
40
60
80
100
120
140
160
180

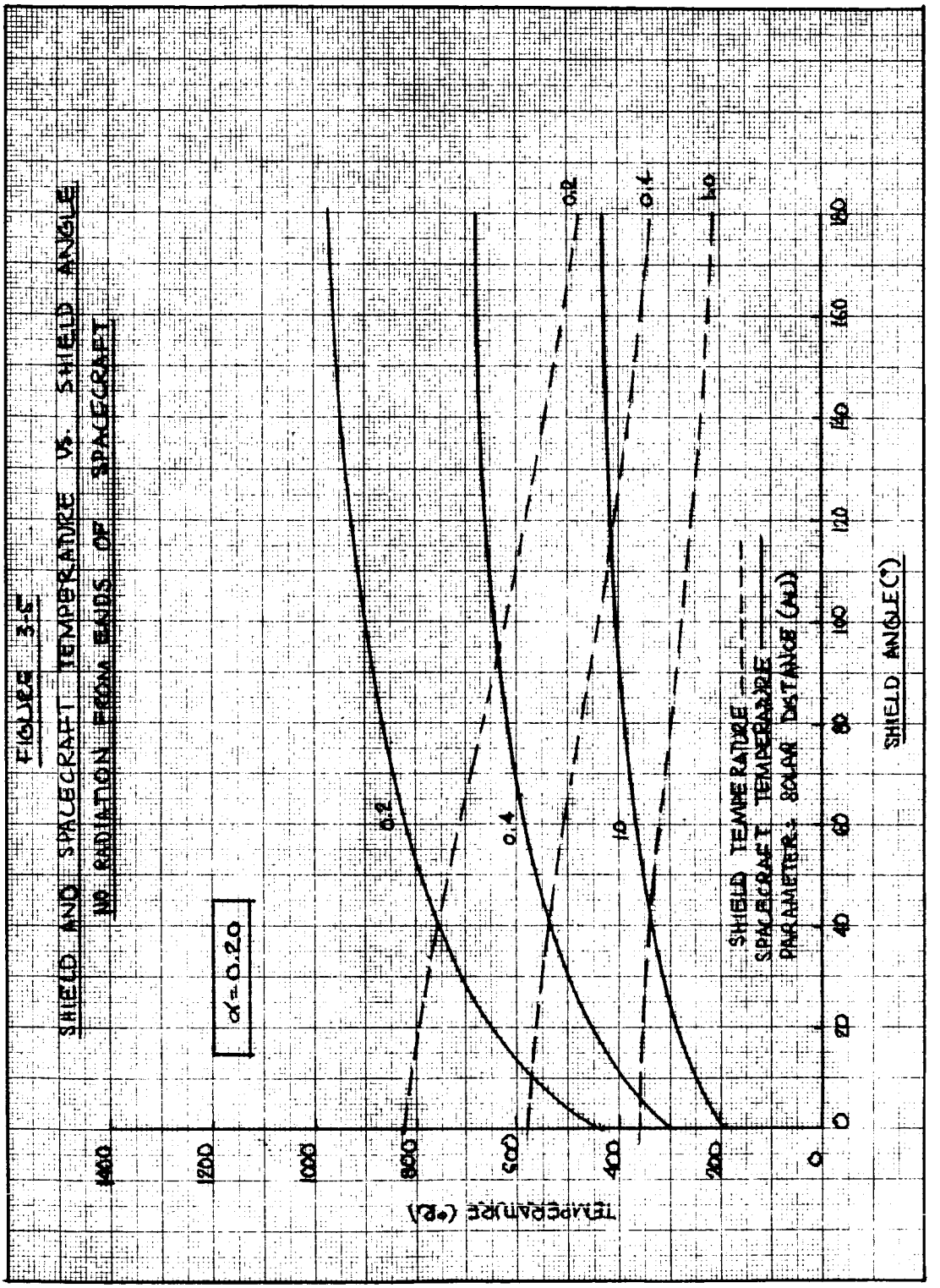
FIGURE 3-5
SHIELD AND SPACECRAFT TEMPERATURE VS. SHIELD ANGLE
W/O RADIATION FROM BANDS OF SPACECRAFT
α = 0.20
0.2
0.4
1.0
SHIELD TEMPERATURE
SPACECRAFT TEMPERATURE
PARAMETER: SOLAR DISTANCE (AU)
TEMPERATURE (°R)
SHIELD ANGLE(°)
1400
1200
1000
800
600
400
200
0
20
40
60
80
100
120
140
160
180

3.2 EFFECT OF SPACECRAFT SPINNING

In order to simplify the thermal model of the spacecraft, it was assumed that the spacecraft was isothermal. This assumption is examined below to determine its validity.

(a) Assumptions

The following assumptions are made in this analysis:

(i) Solar cells are mounted on a cylinder composed of aluminum honeycomb sandwich construction. The facings are 10-mil aluminum sheets; the core is 1-mil aluminum foil; and the sandwich is 0.250-in. thick.

(ii) It is assumed that axial temperature gradients are negligible and all circumferential heat transfer occurs in the facings (this assumption will cause larger gradients).

(iii) The heat capacity of the facings is assumed to be that of the aluminum facings. (This assumption will also give circumferential gradients larger than actual since the heat path is considered to be entirely within the facings. This neglects the capacity of the core and its bonding agent; thus, giving a lower capacity than actually obtains.)

(iv) The surface of the cylinder is assumed to be thermally isolated from the interior of the spacecraft.

(b) Analysis

Solar heating of a rotating cylindrical space vehicle has been considered analytically by Charnes and Raynor[1]. The following analysis is based on their work.

The reference analysis provides an expression for the temperature of the spinning cylinder in terms of the parameters: ρ_o, V_o, T_o, and η. η is a coordinate fixed with respect to the sun-spacecraft line and measured in a plane perpendicular to the cylinder axis as shown in Figure 3-6.

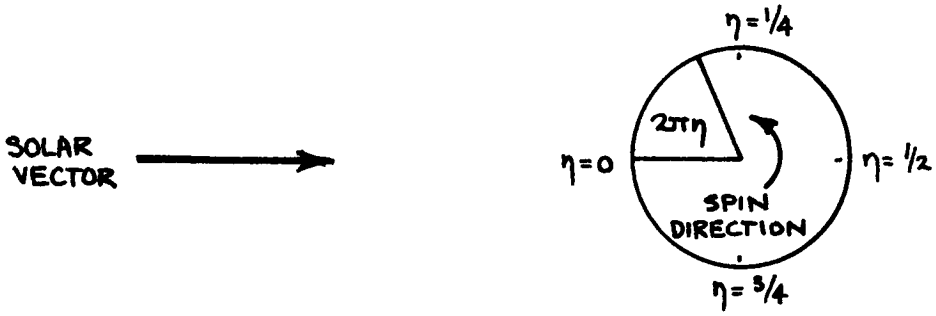

Figure 3-6 Top View of Spinning Cylinder Showing Coordinate System

ρ_o, V_o, and T_o are defined as follows:

$$\rho_o = \left[\frac{16\, r^2\, \pi \alpha S}{t k T_o}\right]^{1/2} \tag{3-4}$$

$$V_o = \frac{V \pi r}{d \rho_o} \tag{3-5}$$

$$T_o = \left[\frac{\alpha S}{\pi \epsilon \sigma}\right]^{1/4} \tag{3-6}$$

where:

r = cylinder radius

α = absorptance of cell/filter combination

S = solar constant

t = cylinder wall thickness

k = thermal conductivity of wall

T_o = equilibrium temperature of isothermal cylinder

V = tangential velocity of cylinder wall

d = thermal diffusivity of cylinder wall

ϵ = total hemispherical emissivity of cylinder wall.

When $V = 0$, T_{max} occurs at $\eta = 0$; as V increases, T_{max} is shifted in the direction of rotation to a maximum displacement of approximately 71.46° from the sun-satellite line. The form of the temperature forcing function over the surface of the cylinder (a rectified cosine function) dictates that the solution of the differential equation for $T(\eta)$ must be in three parts:

$$\text{I} \quad 0 < \eta < \frac{1}{4}$$

$$\text{II} \quad \frac{1}{4} < \eta < \frac{3}{4}$$

$$\text{III} \quad \frac{3}{4} < \eta < 1$$

Determination of the difference $T_{max} - T_o$ will indicate the extent of the temperature gradient around the cylinder. We are concerned with a spinning cylinder which causes T_{max} to lie within the region for which $\frac{3}{4} < \eta < 1$. The solution in this region will be simplified considerably if $V_o^2 >> 1$ and $V_o \rho_o >> \pi^2$.

Numerical evaluation of the system parameters and the appropriate solution will be found in Appendix B. The resulting expression for the temperature of the spinning spacecraft is

$$T = T_o \left\{ 1 + 7.4 \times 10^{-4} (\eta - 1) + 1.1 \times 10^{-6} (\eta - 1)^2 - 3.7 \times 10^{-4} \sin 2\pi\eta \right\} \qquad (3\text{-}7)$$

where T is the temperature of the spacecraft as a function of the position variable, η.

Examination of equation (3-7) indicates that T differs from T_o by less than 1% throughout the region for which $\frac{3}{4} < \eta < 1$. It can be concluded that, in the real case -- with the thermal shield, increased capacitance of the spacecraft, heat transfer in the honeycomb, etc. -- circumferential temperature gradients in the spacecraft surface are negligible. This result obtains at all solar distances of interest in the present study.

3.3 RADIAL TEMPERATURE GRADIENTS IN THE SHIELD

The analysis of Section 3.1 assumed an isothermal heat shield. In fact, a radial temperature drop will exist in the shield which will have the effect of lowering the temperatures of the solar cell surfaces (node 1).

Radial* temperature gradients in the shield have been considered for two extreme cases: a shield angle of $2\theta = 0^{\circ}$ (shield fully closed), and a shield angle of $2\theta = 180^{\circ}$ (shield completely open). Details of the analysis are given in Appendix C; results are tabulated in Table 3-1, below.

TABLE 3-1

EFFECT OF RADIAL THERMAL GRADIENT IN HEAT SHIELD

Case	α_{s_1}	Solar Distance (AU)	Shield Angle (2θ)	Spacecraft Temperature, T_1 (°R)	
				Isothermal Shield	Non-isothermal Shield
III	0.56	1.0	0°	190	102
			180°	562	569
		0.4	0°	300	160
			180°	889	899
		0.2	0°	423	227
			180°	1257	1273
IV	0.20	1.0	0°	190	101
			180°	435	440
		0.4	0°	300	160
			180°	687	695
		0.2	0°	424	227
			180°	972	983

*Radial is defined herein as in the direction of the radius of the cylindrical spacecraft.

Table 3-1 shows that the maximum effect of radial thermal gradients in the shield occurs at 0.2 AU with the shield closed ($2\theta = 0^{o}$). In this case, solar cell temperatures will be reduced about 45%. The general effect is to increase the temperature extremes experienced by the spacecraft; upper limits increase only slightly, and lower limits drop significantly.

Since thermal problems associated with solar cells operating in a near-solar environment have to do with temperatures that are too high, not too low, the assumption of an isothermal shield provides conservatism in the photovoltaic calculations which are a function of cell temperature.

3.4 CIRCUMFERENTIAL TEMPERATURE GRADIENTS IN THE SHIELD

Circumferential* thermal gradients in the heat shield have not been studied in detail. However, the effect of these gradients will be similar to the results discussed above.

The effect will only be significant with the shield closed, or near-closed. Consideration of radial gradients will reduce the lower limit of the predicted temperatures. As a result, a further degree of conservatism is included in the analysis of the system.

3.5 DISCUSSION

The thermal analysis in this study is essentially conservative in the sense that predicted solar array and thermal shield temperatures are higher than those which actually will occur. This conservatism results from the assumption of an isothermal shield where, in fact, the shield will have both radial and circumferential thermal gradients.

The assumption of an isothermal spacecraft (i.e., solar array) appears to be valid.

---

*Circumferential is defined herein as on the circumference of the thermal shield (or spacecraft), and in a plane perpendicular to the centerline of the spacecraft.

Multiple reflections of solar radiation between the shield and the spacecraft have not been considered in this analysis. However, the geometry of the selected configuration (Figure 4-2) is such that very little solar radiation will enter the space separating the shield and the spacecraft.

4.0 THERMAL SHIELD CONCEPTUAL DESIGN

The purpose of the thermal shield is to control the temperature of the solar cells by minimizing the effective number of cells exposed to the incident flux during a near-solar mission. Figures 4-1 and 4-2 suggest two possible configurations which could be used to satisfy the thermal shield requirements.

Configuration 1, (shown in Figure 4-1) consists of a single hemicylindrical surface which rotates with respect to the cylindrical spacecraft. This configuration is probably the simplest and most direct method of effecting the shield. However, this concept has a serious drawback. Power produced by the solar cells on the cylindrical surface of the spacecraft is an inverse function of the angle of incidence between the solar flux and the normal to the surface of each cell; at large incidence angles, the cell power drops rapidly to zero. (This phenomenon is described in detail in Section 5.) Also, the large shifts that occur in the spectral transmission of filters when the incidence angle is large affects both heating and adhesive degradation. With this configuration, a relatively large number of cells must be exposed at any given power level; as a result, cell temperatures will be higher and, consequently, photovoltaic performance will be degraded. Also, a large number of exposed cells will receive solar energy at large incidence angles and will thus be operating inefficiently or not at all.

Configuration 2, (shown in Figure 4-2) consists of two counterrotating cylindrical surfaces which rotate with respect to the spacecraft. This method eliminates the drawbacks cited for configuration 1. Incidence angle effects are virtually eliminated. The cells first exposed with a small opening of the shield (as would be the case near the sun) are at an incidence angle close to zero. Thus, cell performance can be maximized with a minimum effective exposure. This is the recommended configuration, and it will be used in the remainder of this report as the reference concept.

In both of the above cases, the shield configuration is compatible with the physical description cited in Section 2.1a.

FIGURE 4-1
CONFIGURATION SCHEMATIC-
SINGLE ACTIVE THERMAL SHIELD
(CONFIGURATION 1)

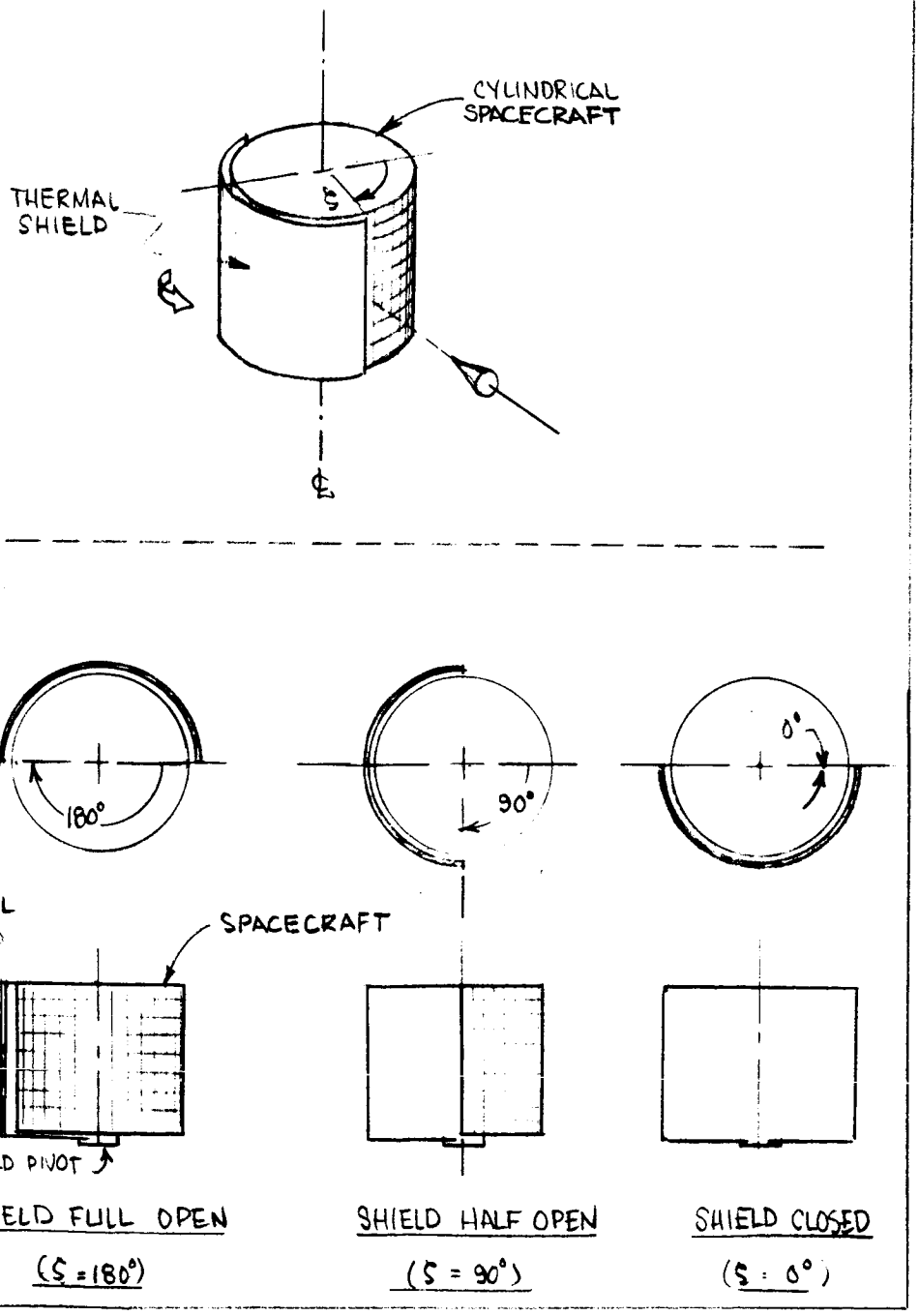

FIGURE 4-2
CONFIGURATION SCHEMATIC -
ACTIVE SHIELD CONSISTING OF TWO COUNTER-ROTATING SHIELDS
(CONFIGURATION 2)

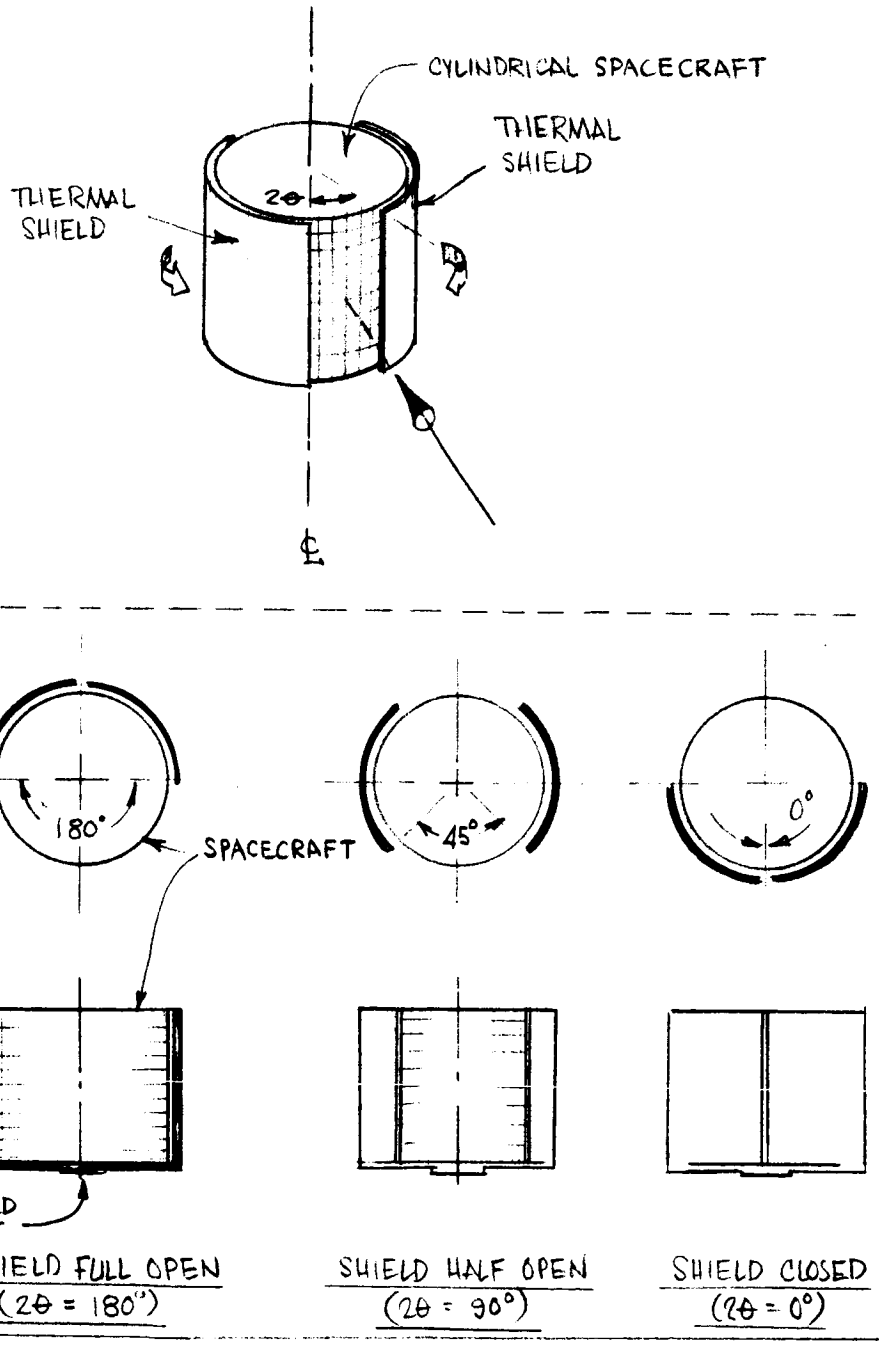

5.0 PHOTOVOLTAIC ANALYSIS

Parameter investigation and system design of solar cell arrays have been primarily concerned with operation in near-earth environments. Consequently, there is a paucity of data regarding high-temperature photovoltaic operation under conditions of intense solar illumination. Several parameters that can be neglected for near-earth missions become quite significant for a near-solar mission. For example, silicon solar cells, body-mounted on an unshielded cylindrical spacecraft, approach zero power output between 0.5 and 0.4 AU because of temperature limitations.

In the following sections, the performance of silicon solar cells is discussed, with an emphasis on near-sun operation. The discussion includes consideration of spectrally selective filters, cover glass adhesives, and particle radiation damage. In addition, the current state-of-the-art of single-crystal gallium arsenide solar cells is presented. State-of-the-art components and techniques are stressed throughout (with the possible exception of two special filters which are considered).

5.1 SILICON SOLAR CELLS

Performance characteristics and selection criteria of silicon solar cells are discussed below. A specific N/P cell is selected.

a. Solar Cell Selection. Solar cell selection was based on the following criteria:

- Performance Reliability
  - (1) Elevated temperatures
  - (2) Very high intensity
  - (3) Particle radiation resistance
- Flight Quantity Availability
- Cost
- Utilization of existing Pioneer spacecraft tooling
- Current state-of-the-art.

A 1 x 2 cm, 10 Ω-cm N/P silicon solar cell with 10.7 percent conversion efficiency at 28°C and air mass zero was selected.

b. Radiation Resistance. The radiation resistance of the N/P silicon cell is so superior[2,3,4] to the P/N that virtually all major solar cell manufacturers have changed their production lines to the N/P cells. Thus, only the N/P type will be considered here. Radiation resistances for the two types of silicon solar cell are compared in Appendix E.

c. Base Material Resistivity. Another factor involved in the selection of silicon solar cells is the specification of the nominal base material resistivity. This resistivity is essentially an impurity level, and is expressed in units of ohm-centimeters.

Initial reports on the investigation of N/P cells with base resistivities between 1 and 25 Ω-cm indicate an improvement in radiation resistance with increasing base resistivity[4].

d. Cell Manufacturing Capability. Flight quantity solar cell production capability is a primary criterion for spacecraft photovoltaic system design. Manufacture of the higher base resistivity cell necessitated improvements in the manufacturing process -- particularly with respect to quality control. A typical yield distribution from one manufacturer is shown in Figure 5-1 for 10 Ω-cm N/P 2 x 2 cm cells. However, some manufacturers have yet to maintain consistent yields of this type. The cost of large order 1 x 2 cm 10 Ω-cm N/P silicon cells is between $2.00 and $3.00 apiece.

e. Connections. Earth-orbiting spacecraft utilizing photovoltaic power systems generally employ tin-lead solders for sintered connections between cells and modules (specifically: 62% tin, 36% lead, and 2% silver). This solder, with a 190°C melting point, is temperature limited. However, high temperature connections should be attainable using a high-temperature solder or, possibly, a welded connection[5].

f. Grid Lines. Solar cell internal series resistance influences the voltage-current characteristic curve; increased internal series resistance causes a "rounding" of the output characteristics. Since the solar cell maximum power output is the area of the largest rectangle inside the characteristic curve, "rounding" severely affects the cell performance. This effect is more pronounced under high solar intensities.

FIGURE 5-1

TYPICAL YIELD FOR ONE MANUFACTURER: N/P 10 Ω-CM SILICON SOLAR CELLS

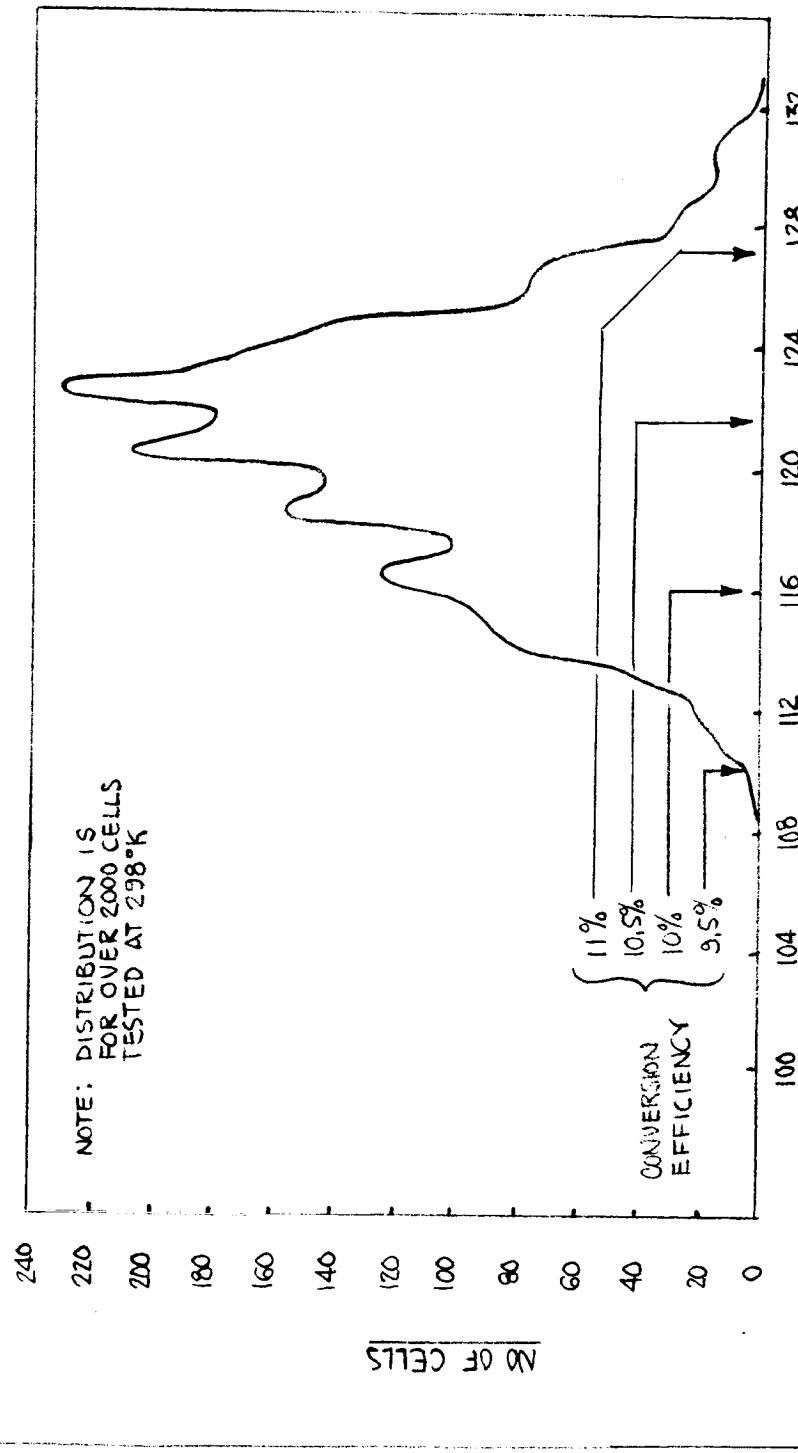

Wolf and Rauschenbach[6] indicate that the internal series resistance can be considered essentially as two equivalent resistances: one corresponding to the combined bulk resistance, contact resistance, and a portion of the diffused sheet resistance near the electrode; the other corresponding to the remainder of the sheet resistance. The diffused sheet resistances can be decreased by adding electrically conducting grid lines to the active cell surface. The spacing of these grids requires a trade-off between the decreased series resistance contribution obtained by an increased number of grid lines and the penalty of decreased active cell surface area by the amount of area covered by the grid lines. Experimental work indicates that an 11 grid line configuration on 1 x 2 in. N/P silicon cells is optimum over an illumination range of 300 to 1400 mw/cm^2. This testing was performed with bare cells at low temperatures.

The cells evaluated in this study were of the conventional 4 grid line configuration. This approach was taken because the critical low power condition was near earth where the 4 grid line configuration is optimum.

It should be noted that several manufacturers of solar cells rate their cells conversion efficiency by considering only the exposed active cell surface area instead of the total surface area of the cell. The difference between these two areas is comprised of the portion of the cell surface covered by the grid lines and the top contact solder strip (sometimes referred to as the bus bar). This covered surface area varies slightly with manufacturer, but is generally about 3 to 5% of the total cell surface area.

In the present analysis, the 10.7% conversion efficiency is applied to the total surface area of the cell. For example, the 10.7% efficient 1 x 2 cm cell normal to the near earth solar intensity of 140 mw/cm^2 would have a maximum power point of 29.96 mw at 28°C.

g. Large Area Silicon Cells. Should a new photovoltaic design be contemplated, it is recommended that the cell size be increased from 1 x 2 cm to 2 x 2 cm. This size increase has the following advantages:

- One 2 x 2 cm cell costs roughly 80% of two equivalent 1 x 2 cm cells[7].
- Fewer connections -- hence, greater reliability.
- Fewer cover glass slides to attach, thus decreasing labor.
- Increased packing factor, since one internal space will be saved with each 2 x 2 cell.
- Increased cell active area.
- Reduction of handling costs by nearly a factor of 2.

Currently, 3 x 3 cm cells are being extensively evaluated at the Goddard Space Flight Center. Present fabrication costs of these 3 x 3 cm cells are high. However, if a breakthrough in this area occurs, the larger cell might well be considered for the close-in solar approach mission for reasons similar to those above.

5.2 GALLIUM ARSENIDE SOLAR CELLS

Gallium arsenide (GaAs) solar cells are an alternative to the silicon cells discussed in the preceding section. The advantages and disadvantages of GaAs are discussed below.

a. Advantages. Single-crystal GaAs solar cells have been thoroughly investigated by RCA and fabricated in pilot line quantities. These cells have demonstrated one definite and another possible advantage over comparable silicon cells. Conversion efficiencies of GaAs cells are superior to production quantity silicon cells at high temperatures, as illustrated by Figure 5-2. However, it should be noted that the 10 percent efficient cell indicated by the figure may not be typical. Further, the temperature range in the present problem is below the level at which this advantage is manifest.

GaAs solar cells have a higher radiation resistance than silicon cells up to a certain dosage. The relative radiation resistance of the two types of solar cell is compared in Appendix E.

b. Disadvantages. The overwhelming disadvantage of single-crystal GaAs solar cells is their very high cost. The only investigating company to reach the potential production stage discontinued work with single-crystal GaAs to concentrate on research with thin film cells.

It has been indicated that a previous quote on flight quantity single-crystal cells was still valid; stated prices were as follows for 72,000 uncoated 1 x 2 cm cells:

Efficiency	First 36,000	Second 36,000
9% minimum	$63.00 ea	$36.00 ea
7% minimum	$25.00 ea	$18.00 ea

FIGURE 5-2

MAXIMUM POWER vs TEMPERATURE

GaAs and SILICON SOLAR CELLS

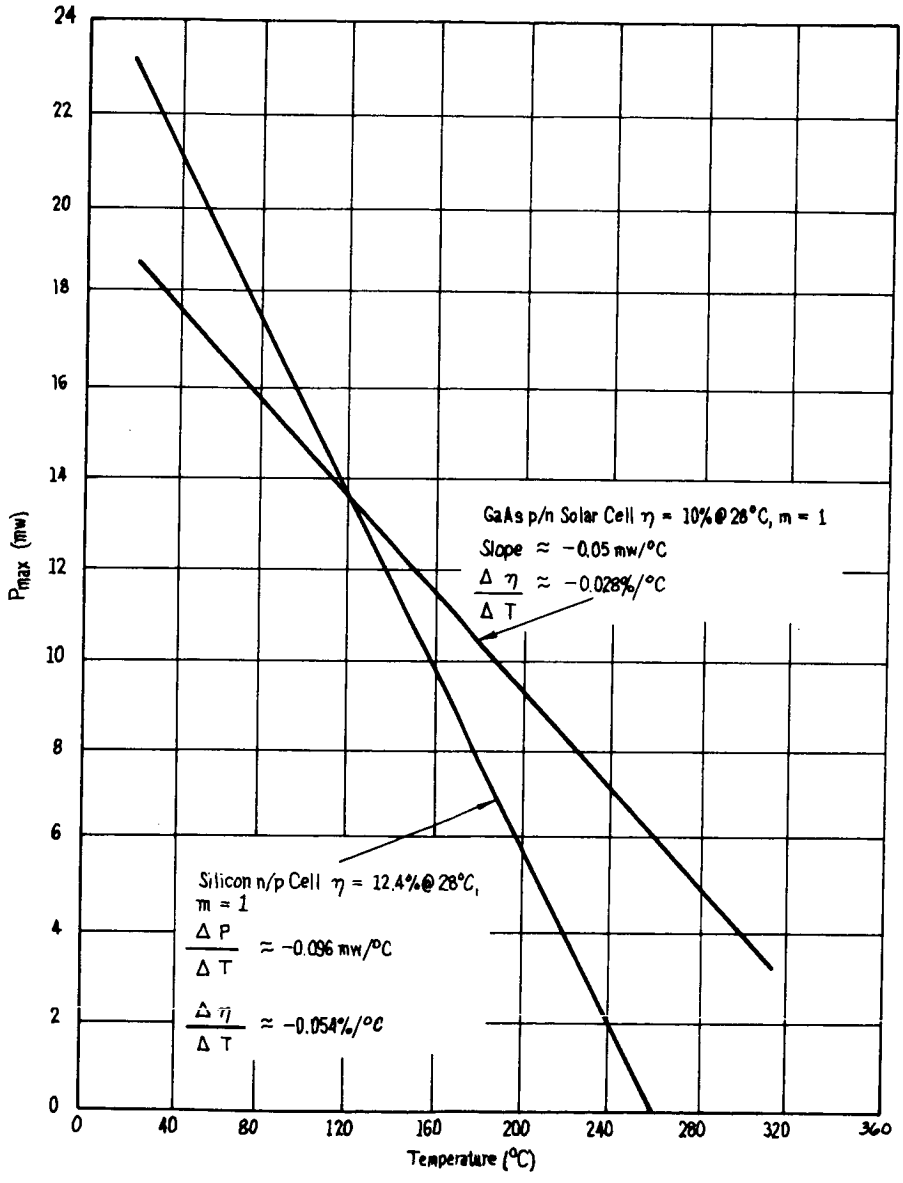

These prices should be compared to the N/P silicon solar cells at about $2.00 each in large quantities.

Preliminary calculations indicate that 9 percent efficient GaAs solar cells will not provide adequate power at 1 AU on the spacecraft configuration under consideration. Thus, in the present study GaAs cells will not be considered further because of deficient performance and excessive cost.

5.3 SOLAR CELL SPECTRALLY SELECTIVE FILTERS

Solar cell conversion efficiency is essentially inversely proportional to the cell's temperature; silicon cells approach zero efficiency at approximately 868° R (209° C). Hence, it is desirable to operate a solar array at as low a temperature as possible.

The most successful solar cell thermal control technique is the installation of cover glass slides with spectrally selective multi-layer interference filters and anti-reflective coatings which selectively reflect wavelengths not photovoltaicly convertible. The cover glass mounting of these filters also increases the solar array emissivity from 0.37 for the silicon to 0.86 for the glass.

a. Filter Characteristics. An ideal filter would transmit solar radiation only in the wavelength region corresponding to the bell shaped spectral response of the solar cell. Unfortunately, real filters include undesirable characteristic transmission bands in the near-IR and IR regions beyonds the cell's response region; this is illustrated in Figure 5-3. Additional filter layers can, to a large extent, be used to suppress these secondary transmission bands.

Most earth-orbiting spacecraft utilize a filter which rejects solar energy on the shorter wavelength side of the cell's response bandwidth. These filters -- commonly referred to as "blue filters" -- are generally made by vacuum depositing 20 thin-film layers.

Suppression of both the shorter wavelengths and some of the solar energy just beyond the cell's long wavelength response can be accomplished by using a filter with a larger number of layers; this filter is called the "blue-red filter". Figure 5-4 illustrates the reflectivity characteristics* of this type of filter. Thelan[8] identifies this

* Note: The filter absorptivity is negligible, hence:
Transmission = 1 - Reflectivity.

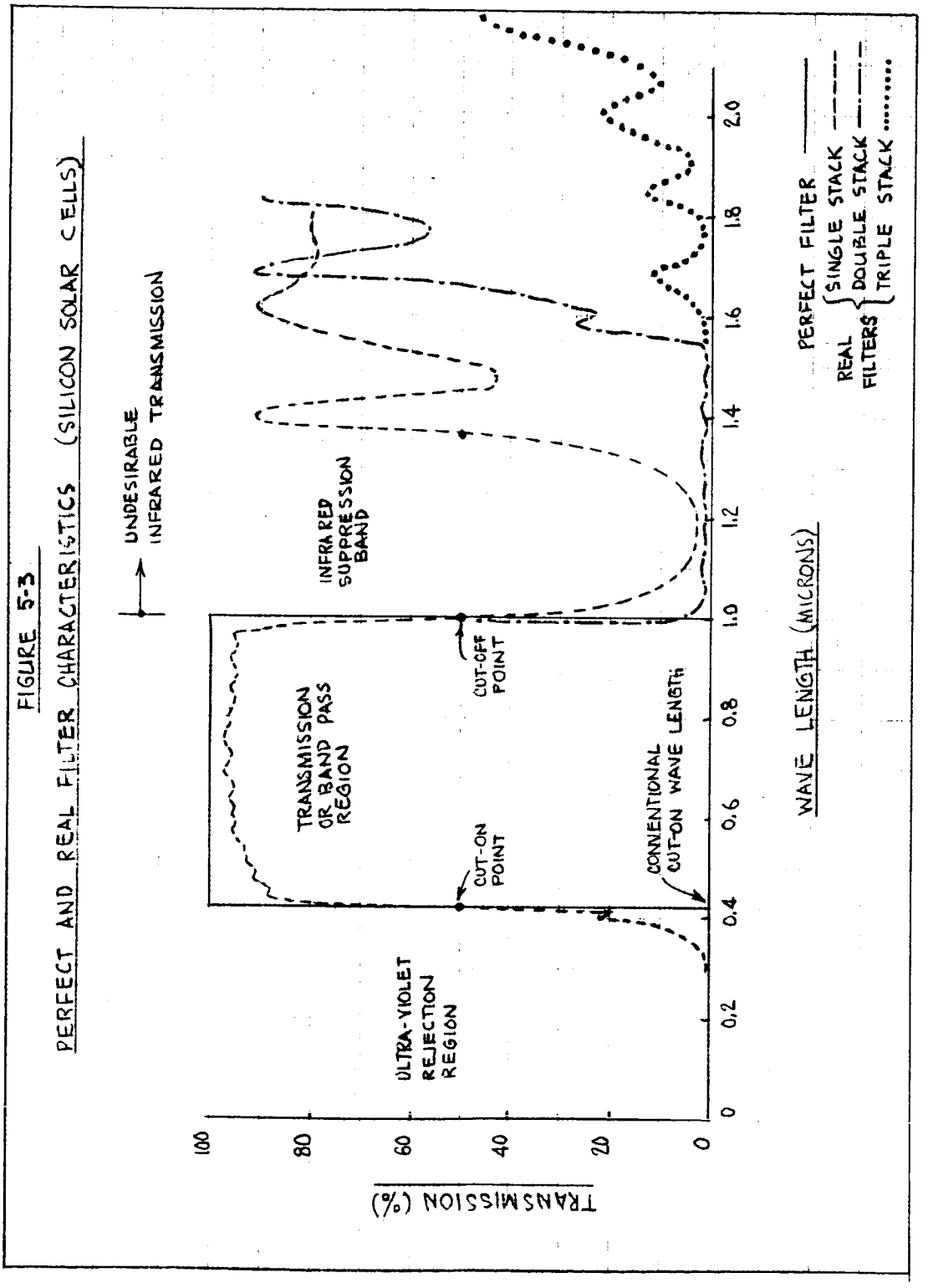
FIGURE 5-3
PERFECT AND REAL FILTER CHARACTERISTICS (SILICON SOLAR CELLS)
UNDESIRABLE INFRARED TRANSMISSION
INFRA RED SUPPRESSION BAND
TRANSMISSION OR BAND PASS REGION
CUT-OFF POINT
CUT-ON POINT
CONVENTIONAL CUT-ON WAVE LENGTH
ULTRA-VIOLET REJECTION REGION
TRANSMISSION (%)
100
80
60
40
20
0
0
0.2
0.4
0.6
0.8
1.0
1.2
1.4
1.6
1.8
2.0
WAVE LENGTH (MICRONS)
PERFECT FILTER
REAL FILTERS
SINGLE STACK
DOUBLE STACK
TRIPLE STACK

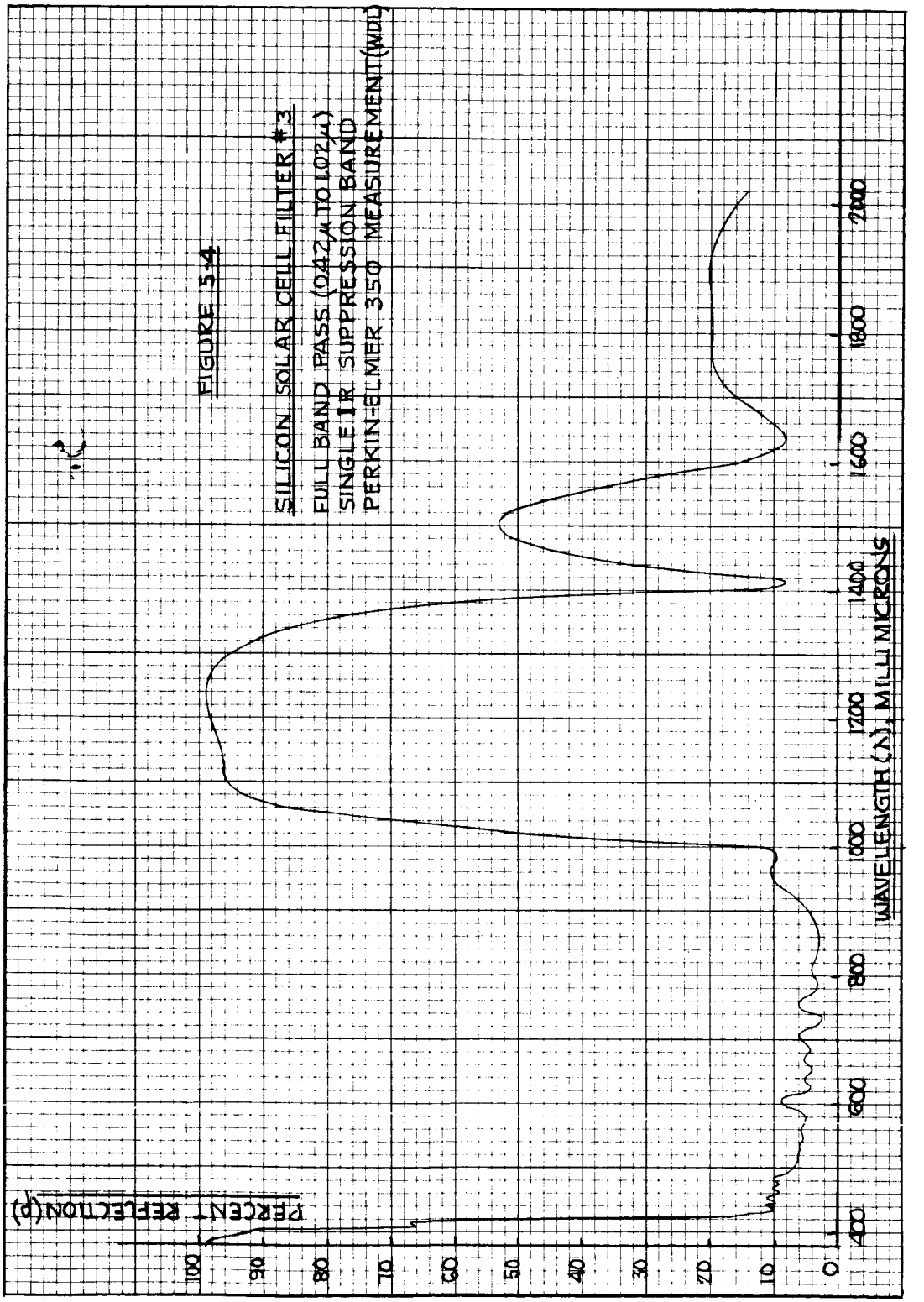

characteristic as a single suppression band. This filter is used extensively in the present analysis, and is identified as filter 3.

Optical Coating Laboratory, Inc., (OCLI) has designed some special blue-red filters in conjunction with Philco's work on photovoltaic power subsystems. These filters include a bandpass more narrow than the total cell response bandwidth, and triple IR suppression bands; performance of these filters is shown in Figures 5-5 and 5-6. Energy transmitted to the cell, but not converted to useful electrical power, is converted to heat. Thus, the narrow bandpass concept was designed to admit energy only in the more efficient cell response wavelengths -- thereby lowering the cell operating temperature. A net power gain is anticipated as a result of the higher efficiency obtained over the smaller range even though part of the cell conversion efficiency is blocked. The filters described above, and designated herein as filters 1 and 2, are compared to filter 3 in Table 5-1.

Clearly, the triple suppression band reduces the cell's operating temperature by reflecting energy at wavelengths beyond the cell's response. Based on the analysis described in Section 6, the best filter for the present mission would be a full-cell-response-bandwidth filter similar to filter 3, with a triple suppression band characteristic.

b. Angle of Incidence Effects. As the angle of incident illumination (i.e., the angle between the incident illumination and a normal to the solar cell filter surface) increases, filters exhibit a characteristic shift to shorter wavelengths accompanied by decreased transmission. This effect is shown in Figure 5-7 for a blue-red filter similar to filter 3. It should be noted that a sharp decrease in transmission occurs above approximately 45^{o}; this is

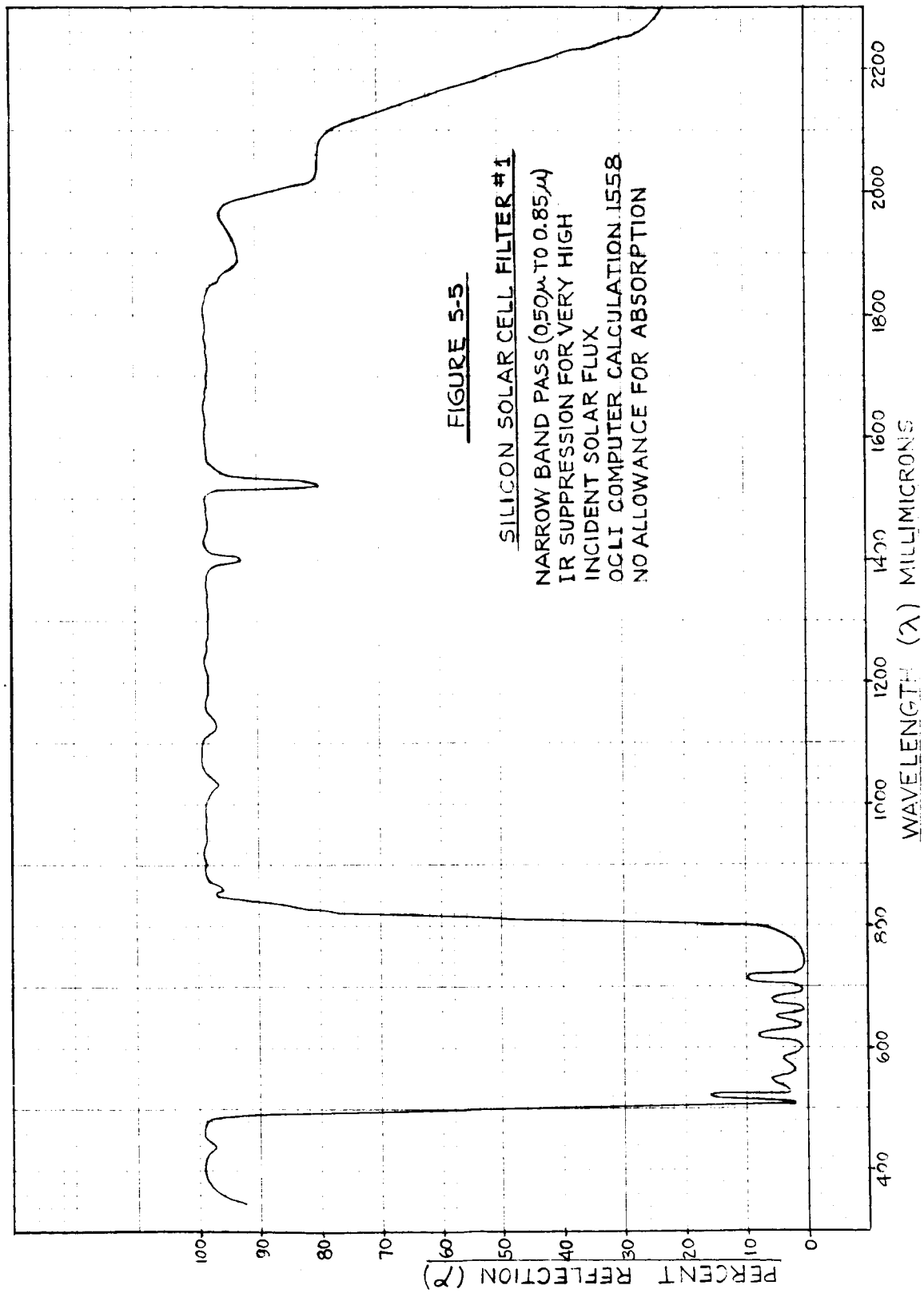
FIGURE 5-5
SILICON SOLAR CELL FILTER #1
NARROW BAND PASS (0.50μ TO 0.85μ)
IR SUPPRESSION FOR VERY HIGH
INCIDENT SOLAR FLUX
OCLI COMPUTER CALCULATION 1558
NO ALLOWANCE FOR ABSORPTION
PERCENT REFLECTION (%)
0
10
20
30
40
50
60
70
80
90
100
WAVELENGTH (λ) MILLIMICRONS
400
600
800
1000
1200
1400
1600
1800
2000
2200

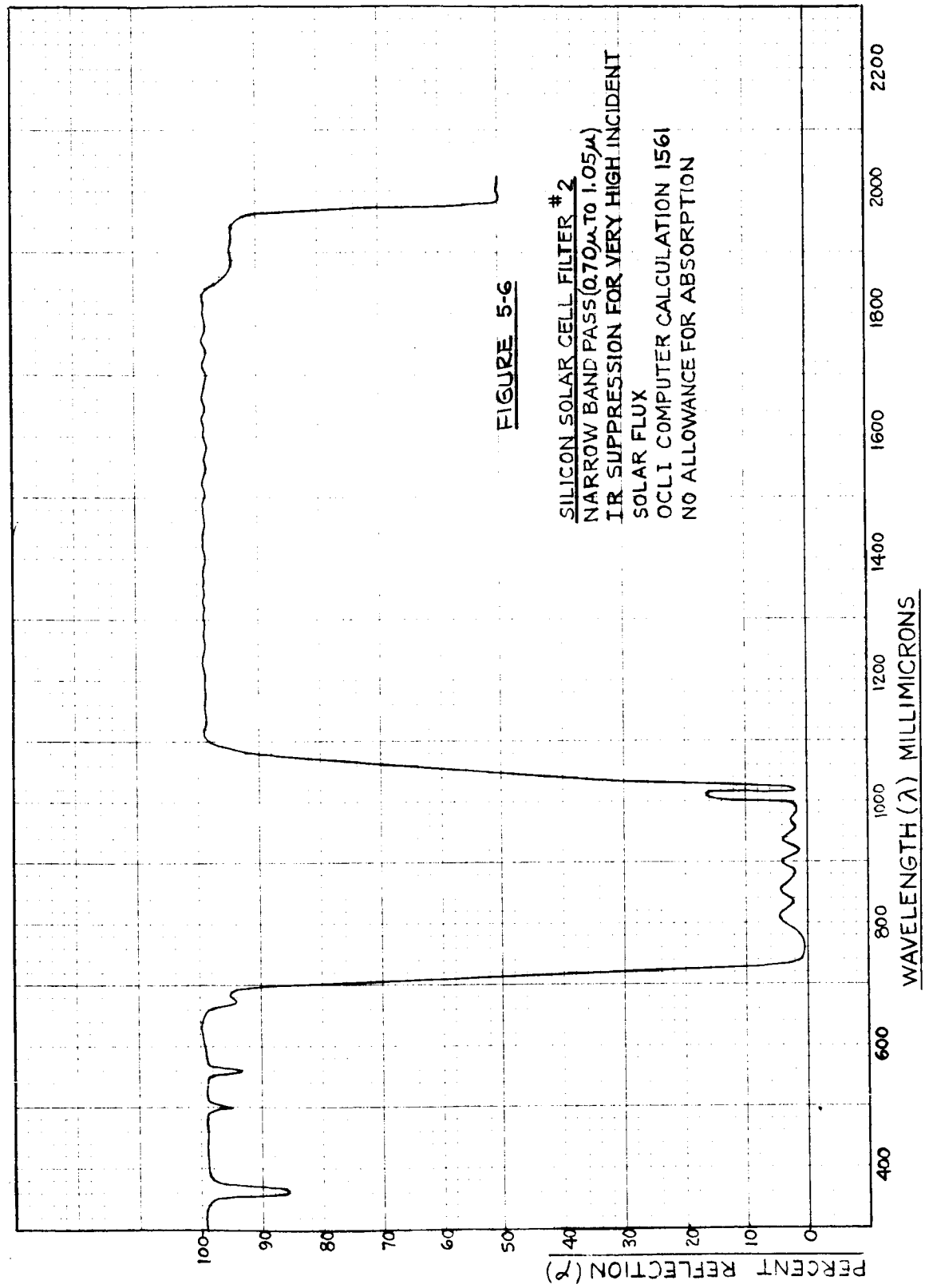
FIGURE 5-6
SILICON SOLAR CELL FILTER #2
NARROW BAND PASS (0.70μ TO 1.05μ)
IR SUPPRESSION FOR VERY HIGH INCIDENT
SOLAR FLUX
OCLI COMPUTER CALCULATION 1561
NO ALLOWANCE FOR ABSORPTION
PERCENT REFLECTION (ρ)
100
90
80
70
60
50
40
30
20
10
0
400
600
800
1000
1200
1400
1600
1800
2000
2200
WAVELENGTH (λ) MILLIMICRONS

FIGURE

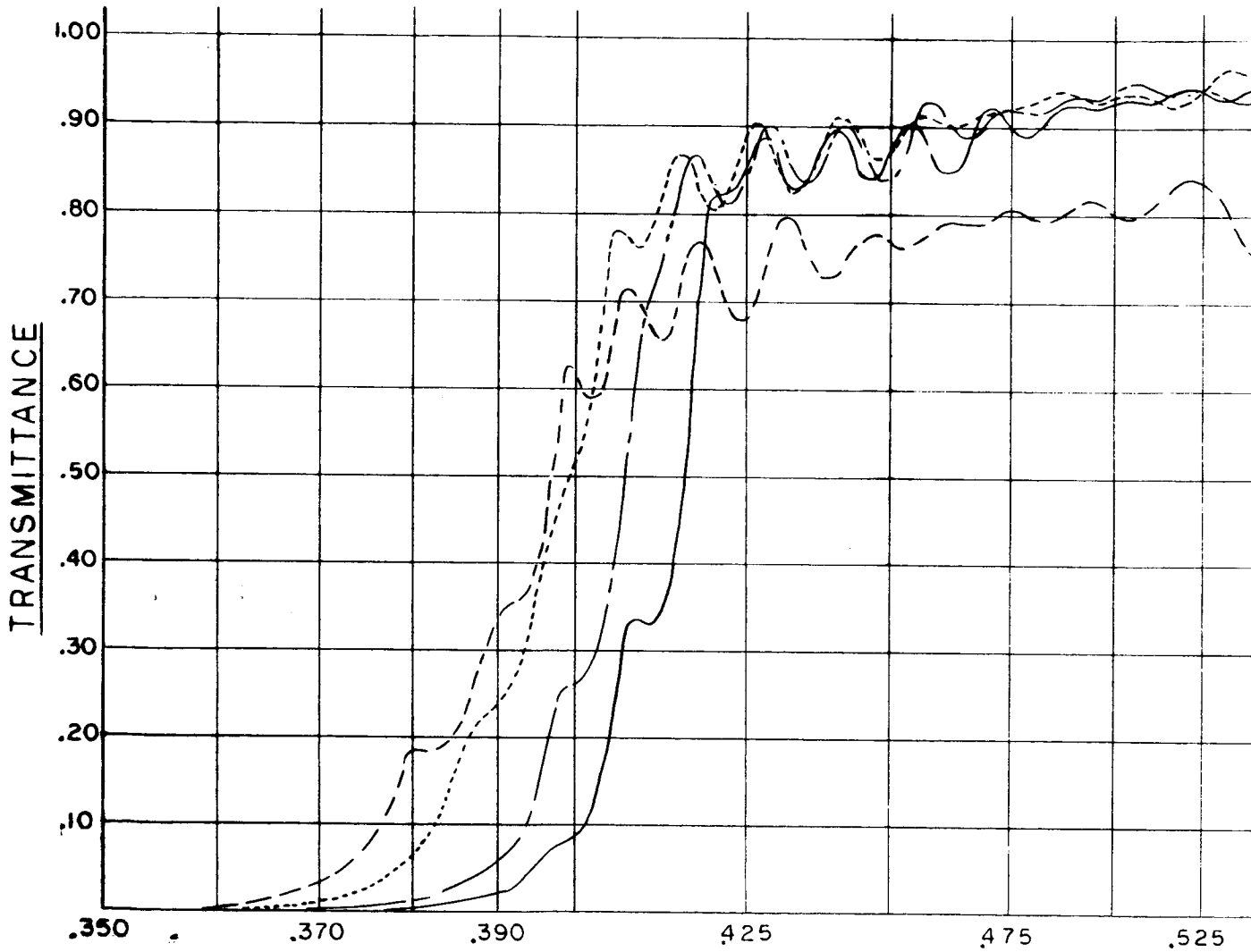

BLUE- RED FILTER ANGLE C

5-7

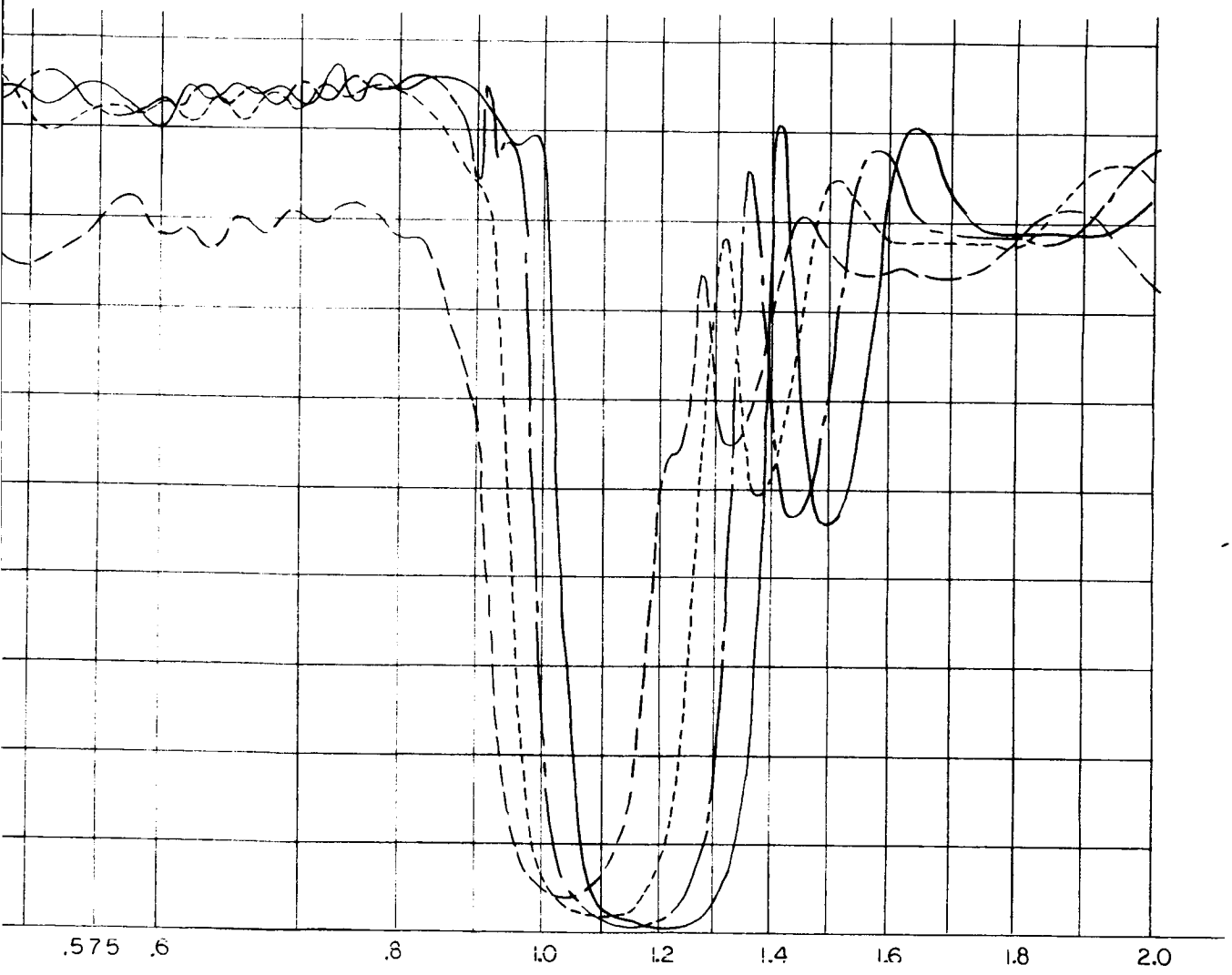

RONS

INCIDENT FLUX NORMAL TO FILTER
30° OFF-NORMAL INCIDENT FLUX
45° OFF-NORMAL INCIDENT FLUX
60° OFF NORMAL INCIDENT FLUX

F INCIDENCE EFFECTS

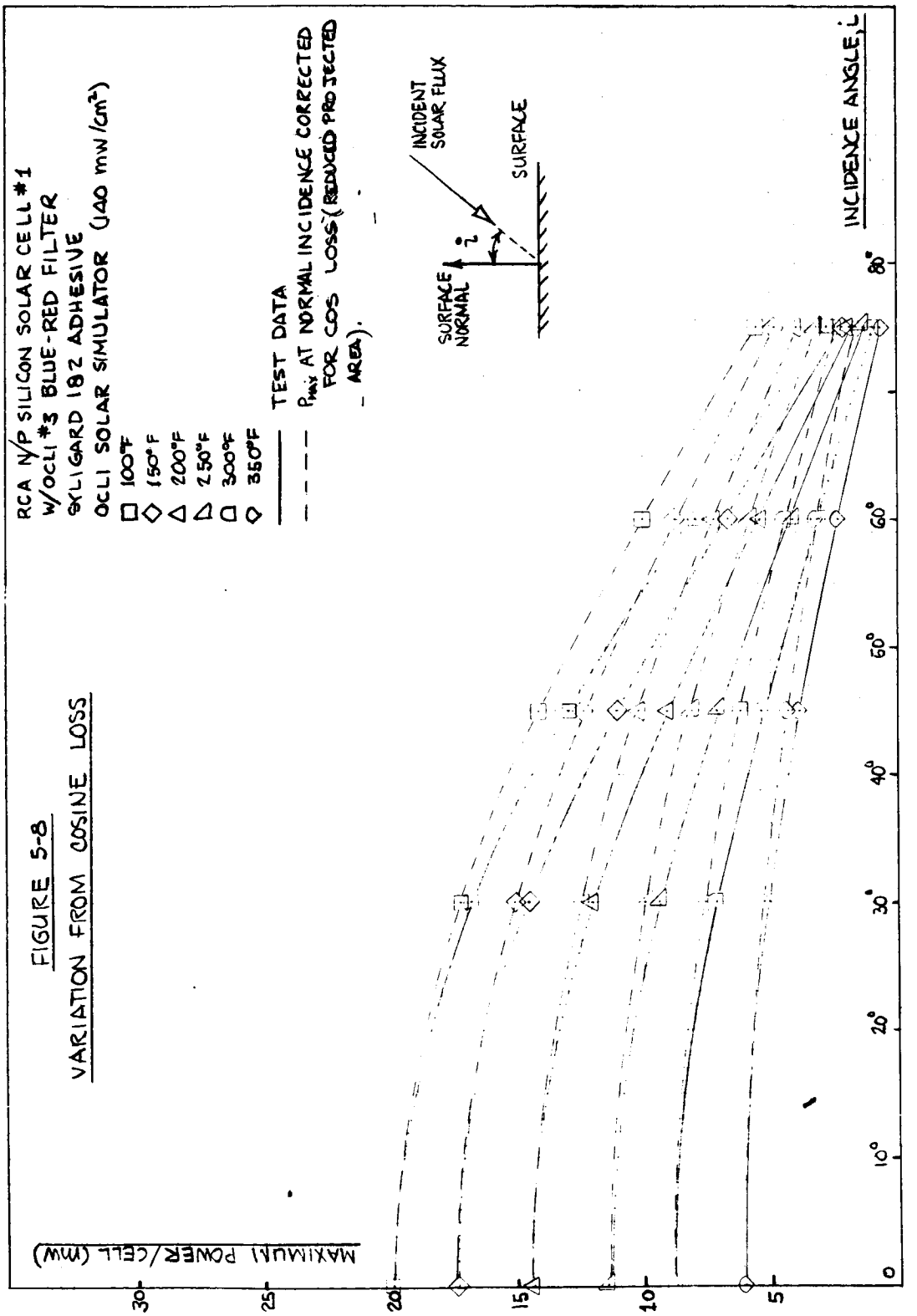

FIGURE 5-8
VARIATION FROM COSINE LOSS

probably due to the polarization effects and increased mismatch of optical layers. A filter cut-on shift to lower wavelengths can be extremely detrimental to the performance of an array, since the optical adhesives are UV sensitive (see Section 5.4).

The incidence angle effects discussed above are increased by the adhesive and represent a strong argument for the configuration shown by Figure 4-2. It is imperative that the incidence angle be kept less than approximately 30°.

TABLE 5-1

FILTER COMPARISON

Filter No.	1	2	3
λcut-on (Microns)*	0.5	0.71	0.42
λcut-off (Microns)*	0.82	1.06	1.02
IR Suppression	Tripleband	Tripleband	Singleband
Availability	6 Weeks	6 Weeks +	2 Weeks
Relative Cost	4.5**	4.5**	1.0
Flight Proven	No	No	Yes

* 50% Transmission Point
** Plus Developmental Cost

c. Temperature Effects. Individual layers of the multilayer metallic oxide filter have indices of refraction which are linear functions of temperature. Since the filter characteristic is derived from the multiple quarter wavelength path through each layer, the perfect thickness for a layer can only be achieved at a particular temperature.

d. Optimization. The filter design problem is one of specifying the optimum orientation angle and temperature so as to minimize power degradation during the mission. This problem is further complicated by a degree of interaction of the temperature effect and incidence angle shift. Filters with large temperature differences which are designed to minimize the wavelength shift are very orientation-angle sensitive. Conversely, filters designed to minimize orientation angle effects are quite temperature sensitive.

5.4 CELL COVER GLASS OPTICALLY TRANSMISSIVE ADHESIVES

There is a paucity of data concerning adhesive transmission characteristics under high intensity illumination. Three distinct problems occur with typical adhesives under such conditions: loss of adhesive strength; alteration of transmission characteristics due to thermal and ultraviolet radiation; and nuclear radiation effects accompanied by an increased thermal absorptance.

a. Ultraviolet Degradation. Preliminary accelerated high temperature ultraviolet exposure tests of several silicon-based optically transmissive cover slide adhesives in a simulated space environment have been conducted at Philco[9]. These tests indicate a slight transmission characteristic shift towards the shorter wavelengths, an a small transmission degradation after 1000 hours exposure to an average intensity of about 5.5 suns in the ultraviolet region. (It should be noted that duplication of the UV portion of the solar spectrum is the laboratory is difficult[10].)

b. Pyrolitic Effects. Transmission degradation and increased absorptance result from exposure of the optical adhesives used in the cell stack to thermal radiation. However, the thermal limitations of these adhesives are not well established.

c. Radiation Effects. Particle radiation encountered in the natural space environment is absorbed by the adhesive; this absorption causes transmission-degrading structural changes. A primary reaction appears to be cross-linking.

d. Synergystic Effects. The combined effect of radiation and elevated temperature on an adhesive which has experienced structural change caused by UV exposure is not well known. It is known that the combined effects cannot be obtained by adding the separate effects of each parameter. Data are conspicuously scarce in this area.

e. Alternates to Adhesive Attachments. There are several alternate procedures currently under investigation that are intended to eliminate the optical adhesive. These include direct fusion of quartz covers to the solar cell, coatings, and mechanical installation (applicable to large area filters).

5.5 PARTICLE RADIATION DAMAGE

The major power degradation hazard encountered on space probe missions is solar flare radiation -- specifically, solar protons. Exposure to a solar flare event can severely curtail the power output from a solar array if the associated shielding is inadequate. However, it is impractical to shield the cells from all radiation; the current design philosophy is to neglect shielding considerations for electron energies above 1 MEV or proton energies above 10 MEV. Shielding is accomplished with a thickness of highly transmissive low α/ϵ material such as fused silica.

Radiation effects are discussed in more detail in Appendix E.

5.6 DISCUSSION

Both the solar cell and the filter selected as a result of the photovoltaic analysis are essentially off-the-shelf production items. Although methods of improving the solar array performance are suggested, the thermal and photovoltaic feasibility of the mission has been established using components that are presently available at a reasonable cost. It is particularly interesting to note that, of the three filters considered, the best performance was obtained from the filter with the lowest cost.

6.0 SOLAR ARRAY POWER OUTPUT PROGRAM

System power and electrical output are considered below in terms of the active control parameter (shield position) and the solar distance.

6.1 SYSTEM SELECTION

Configuration 2, as illustrated in Figure 4-2, is used as the model for the system power program analysis. The shield angle (2θ) is used as the specification of the shield position.

6.2 POWER ANALYSIS

a. Analysis. The maximum power output per unit projected area of the solar array was determined as described below:

$$\frac{\mathbb{P}}{A_p} = S Z \eta_s \eta_T \eta_{FB} \qquad (6\text{-}1)$$

where

$\mathbb{P}$ = power output

A_p = projected surface area = $2rh \sin \theta$

S = incident solar flux

Z = packing factor -- the fraction of the total spacecraft surface (excluding ends) covered with solar cells

η_S = bare solar cell conversion efficiency at air mass zero and 28°C

η_T = cell temperature efficiency

= $1 - 0.00545\ (T - 301^{\circ}K)$ for 10.7% N/P silicon cells

η_{FB} = efficiency ratio, filtered to bare cell

$$= \frac{\int_{\lambda_1}^{\lambda_2} \tau_\lambda r_\lambda^* S_\lambda d\lambda}{\int_0^{\infty} r_\lambda^* S_\lambda d\lambda}$$

τ_λ = spectral transmittance of filter

r_λ^* = normalized solar cell spectral response.

$$= \frac{(r_\lambda)_{max}}{r_\lambda}$$

S_λ = spectral solar intensity distribution

It is apparent from equation (6-1) that cell stack temperature is a very influential parameter in the performance of the solar array.

The thermal analysis of Section 3.0, together with accurate thermal absorptance (α_{ZT}) values for the cell stacks with the filters under consideration, will provide a better estimate of the operating temperatures of the cells. The cell stack absorptance can, in the present case, be represented as the difference between the total absorptance of the cell stack and the energy converted by the cell into electricity:

$$\alpha_{ZT} = \alpha_{ZA} - \eta_{FB}\,\eta_T \tag{6-2}$$

An analytic approach leading to equation (6-2), and utilizing commonly measured parameters, is developed in Appendix G. The main equations from this development are the following:

$$\alpha_{ZA} = 0.05 \sum_{\lambda=0}^{\infty} \left[1-(\rho_{ZA})_\lambda\right] (1+A_\lambda) \tag{6-3}$$

$$\eta_{FB} = \frac{\sum_{\lambda=0}^{\infty} \left[1-(\rho_{ZA})_\lambda\right] r_\lambda^* S_\lambda}{\sum_{\lambda=0}^{\infty} r_\lambda^* S_\lambda} \tag{6-4}$$

The reflectivity values ($[\rho_{ZA}]_\lambda$) are given by Figures 5-4, 5-5, and 5-6. The data for filter 3 (Figure 5-4) is based on spectrophotometer measurements of a fabricated filter; the data for filters 1 and 2 (Figures 5-5 and 5-6) is based on computer calculations

which assumed negligible absorption in the multilayer filter. A correction (A_λ), shown in Figure 6-1, accounts for termination of the filter in an adhesive (with an index of refraction of 1.52) rather than air as used in the reference data. The normalized cell spectral response is given in Figure 6-2. Johnson's data were used for the solar spectral distribution. The solution of equation (6-3) considered the solar spectrum in 5% energy increments.

The cell stack temperature is obtained from a trial and error solution using the absorptivity given by equation (6-2) as α_{s1} in equations (3-1), (3-2), and (3-3). Thus,

$$q_{s1} = A_{p1} S_d \alpha_{ET} \tag{3-1}$$

and

$$T_2^4 = \frac{\epsilon_E A q_{s1} + \left[A(\epsilon_{13}+\epsilon_E) + \epsilon'_{13}A'\right] q_{s2}}{\sigma A\left\{A\left[\epsilon_E(\epsilon_{13}+\epsilon_{23})+\epsilon_{13}\epsilon_{23}\right]+\epsilon'_{13}A'(\epsilon_E+\epsilon_{23})\right\}} \tag{3-2}$$

$$T_1^4 = \frac{\epsilon_E+\epsilon_{23})A\sigma T_2^4 - q_{s2}}{\epsilon_E A} \tag{3-3}$$

The results of the preliminary thermal analysis in Section 3.0 were used as a first cut at cell stack temperatures.

Results from the thermal analysis described above were used in equation (6-1) to obtain the power output of the array.

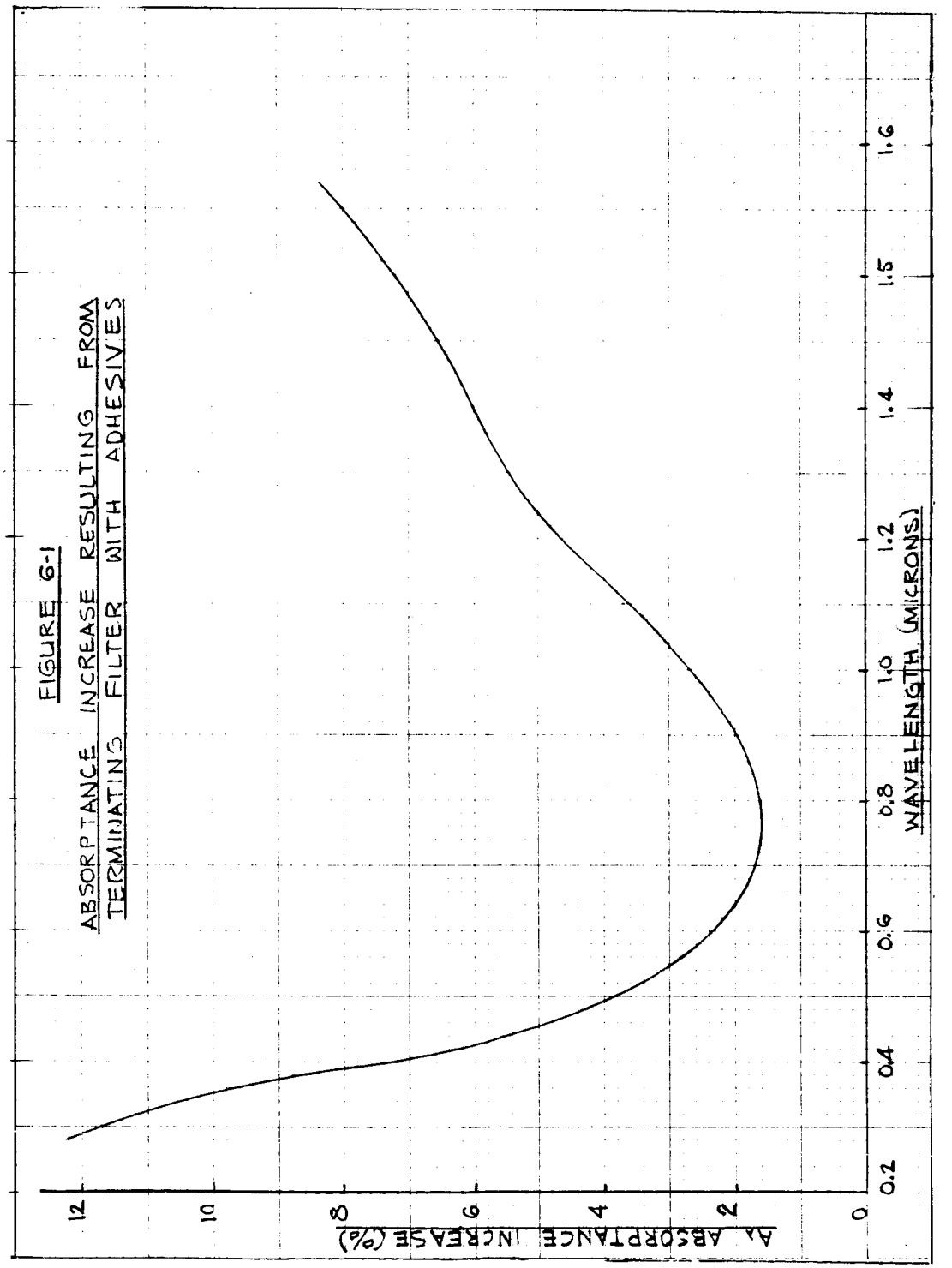

FIGURE 6-1

ABSORPTANCE INCREASE RESULTING FROM TERMINATING FILTER WITH ADHESIVES

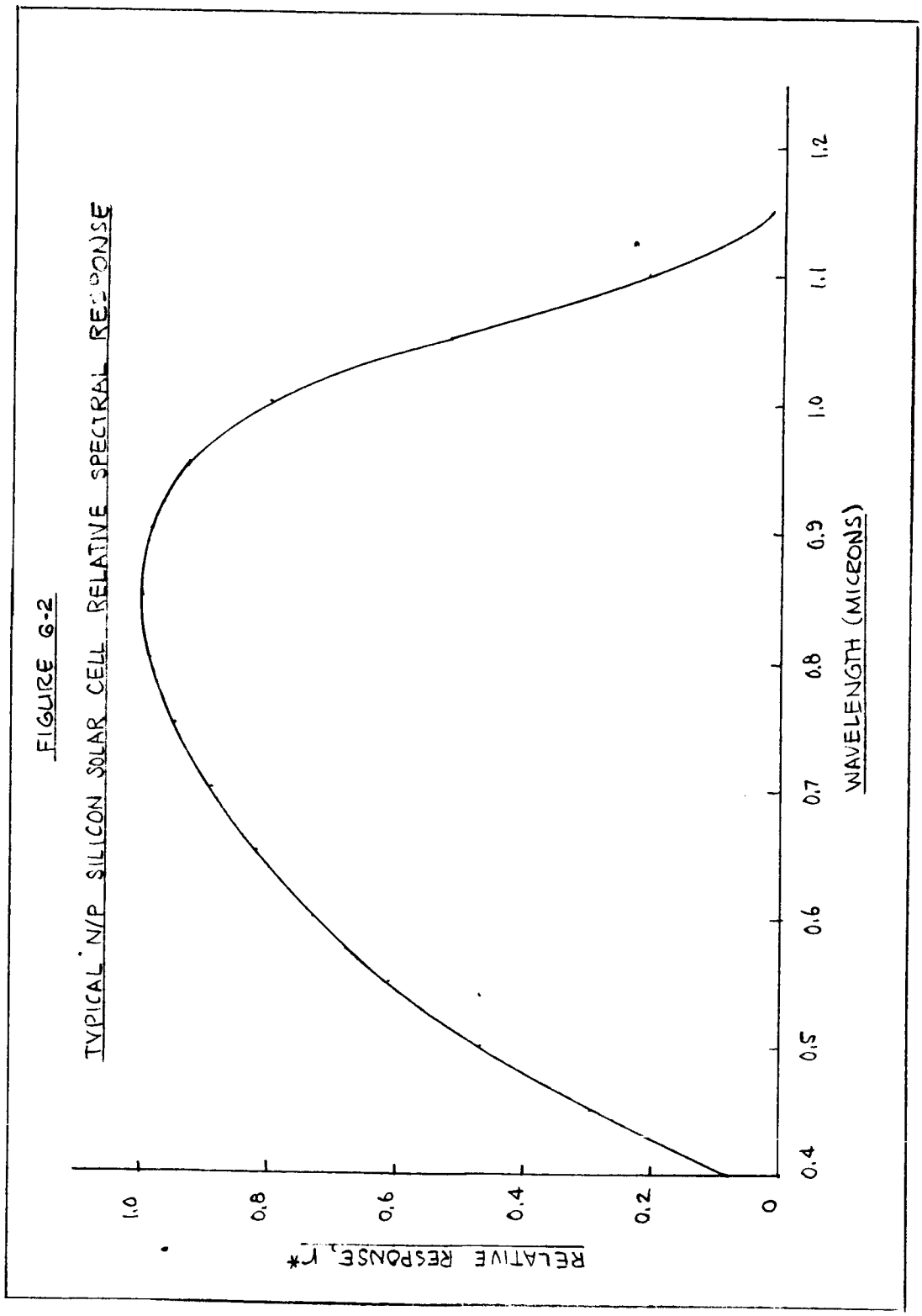
FIGURE 6-2
TYPICAL N/P SILICON SOLAR CELL RELATIVE SPECTRAL RESPONSE
RELATIVE RESPONSE, r*
1.0
0.8
0.6
0.4
0.2
0
0.4
0.5
0.6
0.7
0.8
0.9
1.0
1.1
1.2
WAVELENGTH (MICRONS)

b. Results. The power analysis was based on the use of the N/P silicon solar cell described in Section 5.1(a) with each of the three filters described in Section 5.3 (a).

Values of α_{ZA} were obtained for each filter using equation (6-3) with Figures 5-4, 5-5, and 5-6 for $(\rho_{ZA})_\lambda$ and Figure 6-1 for A_λ. The results of this computation were:

Filter	α_{ZA}
1	0.405
2	0.258
3	0.682

The efficiency ratio, η_{FB}, was also computed for each filter. Figures 5-4, 5-5, and 5-6 were again used for $(\rho_{ZA})_\lambda$; r_λ* was obtained from Figure 6-2, and S_λ from the Johnson data. The results of this calculation, using equation 6-4, were

Filter	η_{FB}
1	0.598
2	0.458
3	0.901

η_T was obtained from

$$\eta_T = 1 - 0.00545\ (T_1 - 301) \qquad (6\text{-}5)$$

with T_1 in $^\circ$K. Z and η_S were given the following constant values:

$$Z = 0.85$$
$$\eta_S = 0.107$$

The following values were used for the solar constant:

AU	S(mw/cm^2)
1	140
0.4	875
0.2	3500

Using the absorptivity equations:

$$(\alpha_{ZT})_1 = 0.405 - 0.598\,[1 - 0.00545(T-301)]$$

$$(\alpha_{ZT})_2 = 0.258 - 0.458\,[1 - 0.00545(T-301)]$$

$$(\alpha_{ZT})_3 = 0.682 - 0.901\,[1 - 0.00545(T-301)],$$

cell stack temperatures were calculated with each of the filters. These results are presented by Figures 6-3, 6-4, and 6-5. The maximum calculated cell temperature is approximately 190°F; the maximum temperature of the thermal shield will be about 380°F.

Using the power equations:

$$P = (2rh \sin\theta)\ S\ (0.107)\ \eta_{FB}\,[1 - 0.00545(T-301)]$$

$$P_1 = 223\ S \sin\theta\,[1 - 0.00545(T-301)]$$

$$P_2 = 171\ S \sin\theta\,[1 - 0.00545(T-301)]$$

$$P_3 = 336\ S \sin\theta\,[1 - 0.00545(T-301)],$$

the power output of the solar array was computed with each of the three filters and for three solar distances (1, 0.4, and 0.2 AU). These results are presented in Figures 6-6, 6-7, and 6-8.

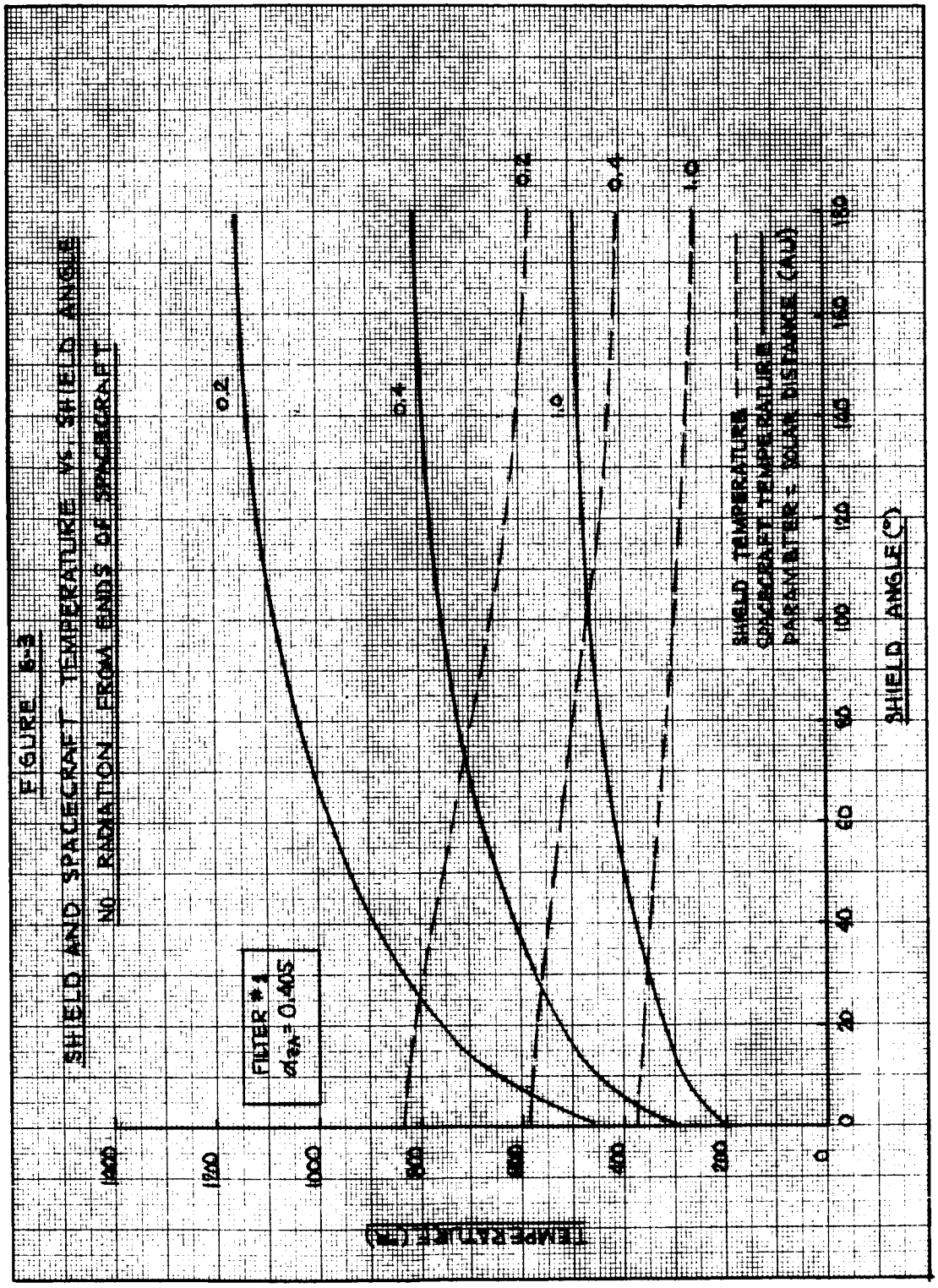
FIGURE 6-3
SHIELD AND SPACECRAFT TEMPERATURE VS. SHIELD ANGLE
NO RADIATION FROM ENDS OF SPACECRAFT
FILTER #1
α_{SA} = 0.405
0.2
0.4
1.0
0.2
0.4
1.0
SHIELD TEMPERATURE
SPACECRAFT TEMPERATURE
PARAMETER = SOLAR DISTANCE (AU)
TEMPERATURE (°R)
SHIELD ANGLE (°)
1400
1200
1000
800
600
400
200
0
0
20
40
60
80
100
120
140
160
180

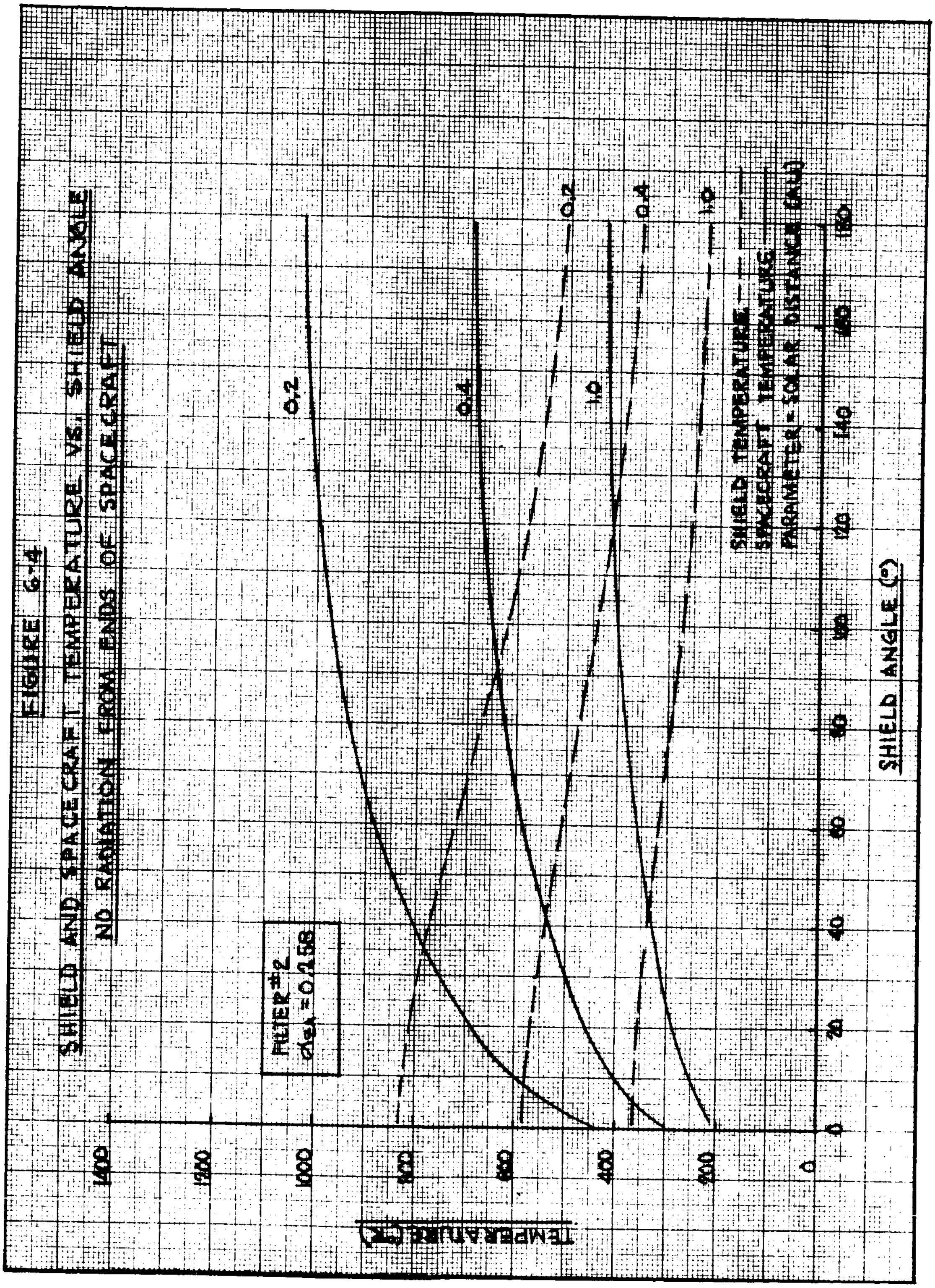

FIGURE 6-4
SHIELD AND SPACECRAFT TEMPERATURE VS. SHIELD ANGLE
NO RADIATION FROM ENDS OF SPACECRAFT

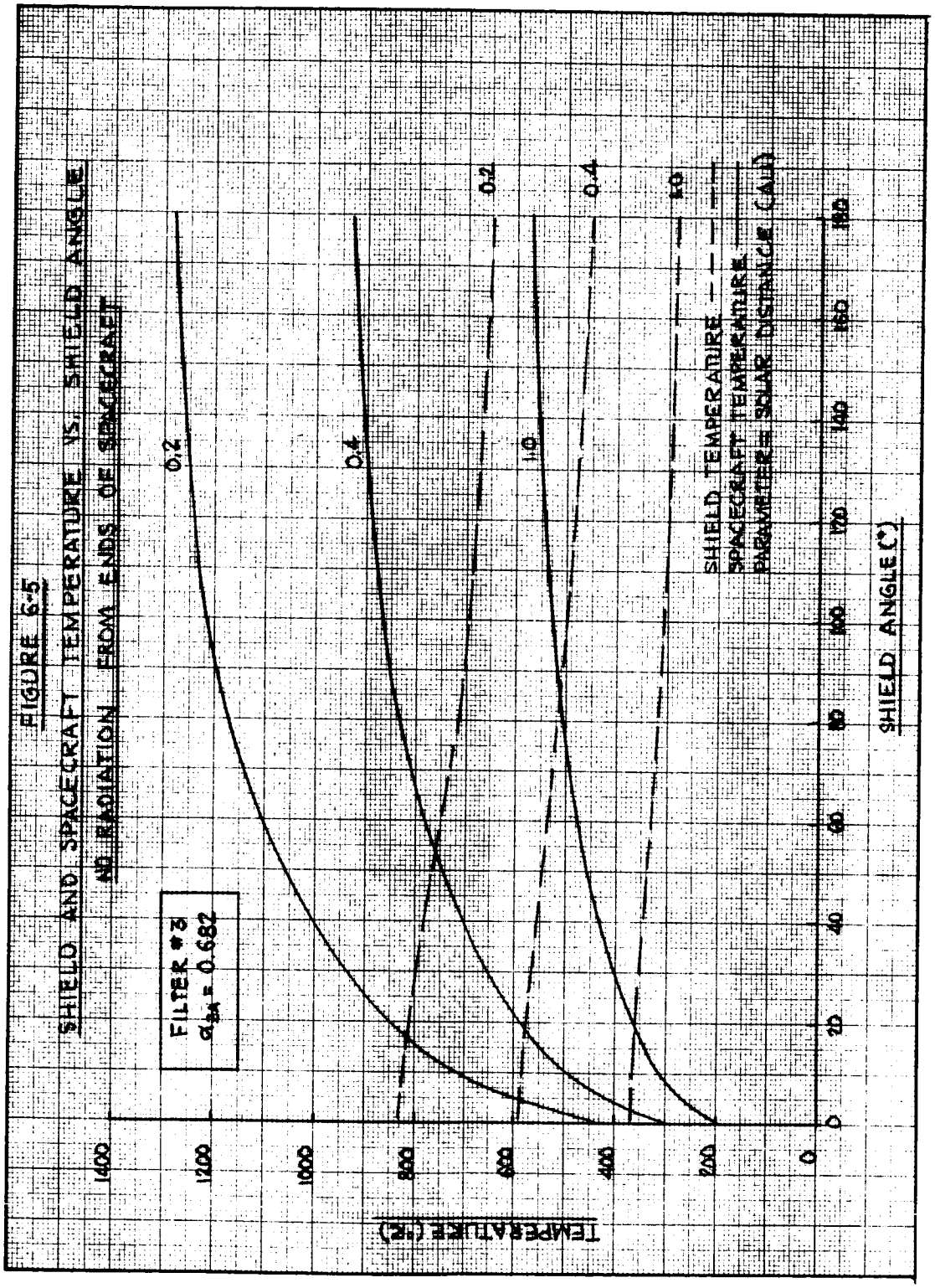
FIGURE 6-5
SHIELD AND SPACECRAFT TEMPERATURE VS. SHIELD ANGLE
AS RADIATION FROM ENDS OF SPACECRAFT
FILTER #3
α_{sh} = 0.682
0.2
0.4
1.0
0.2
0.4
1.0
SHIELD TEMPERATURE
SPACECRAFT TEMPERATURE
PARAMETER = SOLAR DISTANCE (A.U.)
TEMPERATURE (°R)
SHIELD ANGLE (°)
1400
1200
1000
800
600
400
200
0
0
20
40
60
80
100
120
140
160
180

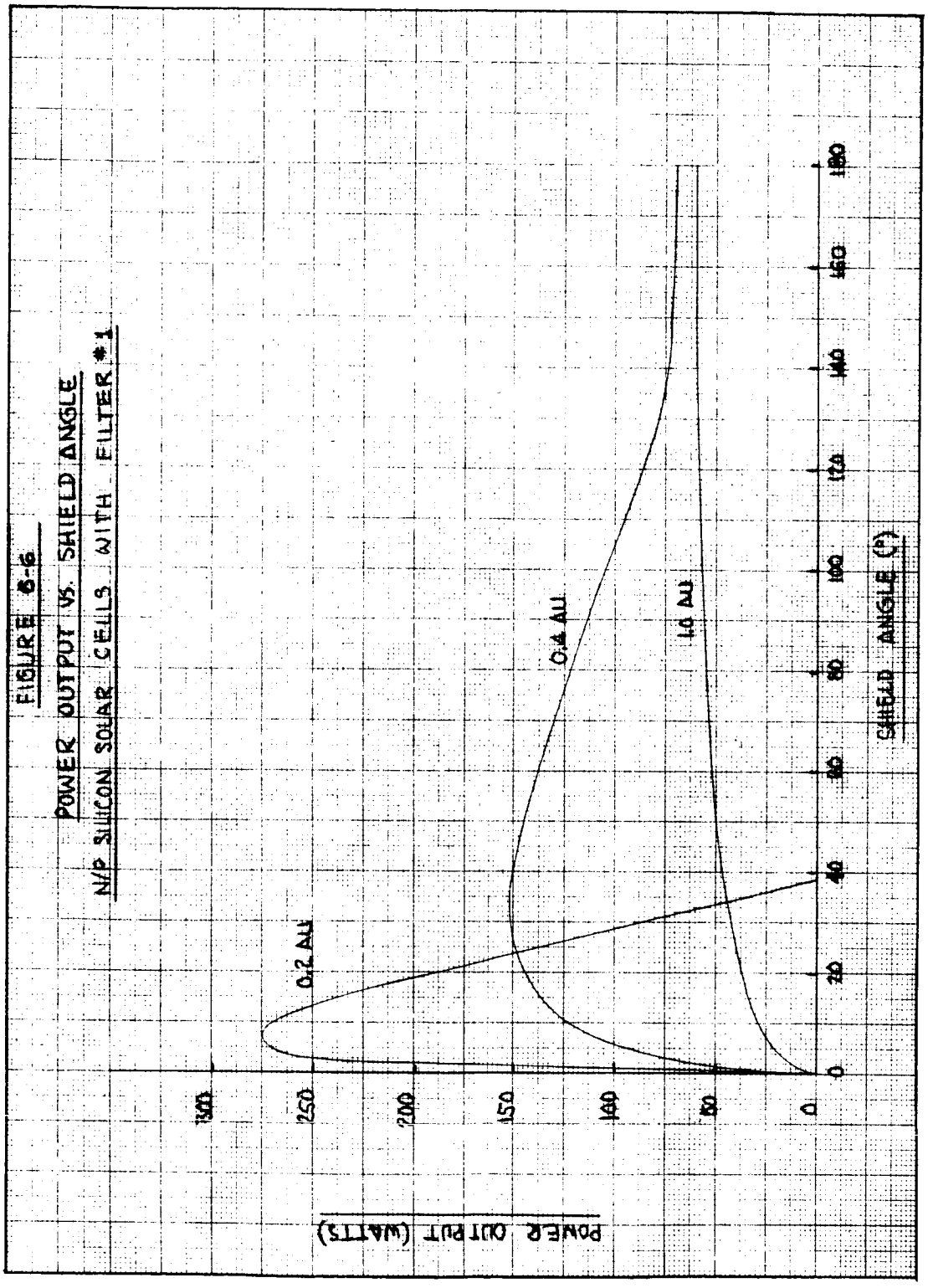
FIGURE 6-6
POWER OUTPUT VS. SHIELD ANGLE
N/P SILICON SOLAR CELLS WITH FILTER #1
POWER OUTPUT (WATTS)
SHIELD ANGLE (°)
0.2 AU
0.4 AU
1.0 AU
0
20
40
60
80
100
120
140
160
180
50
100
150
200
250
300

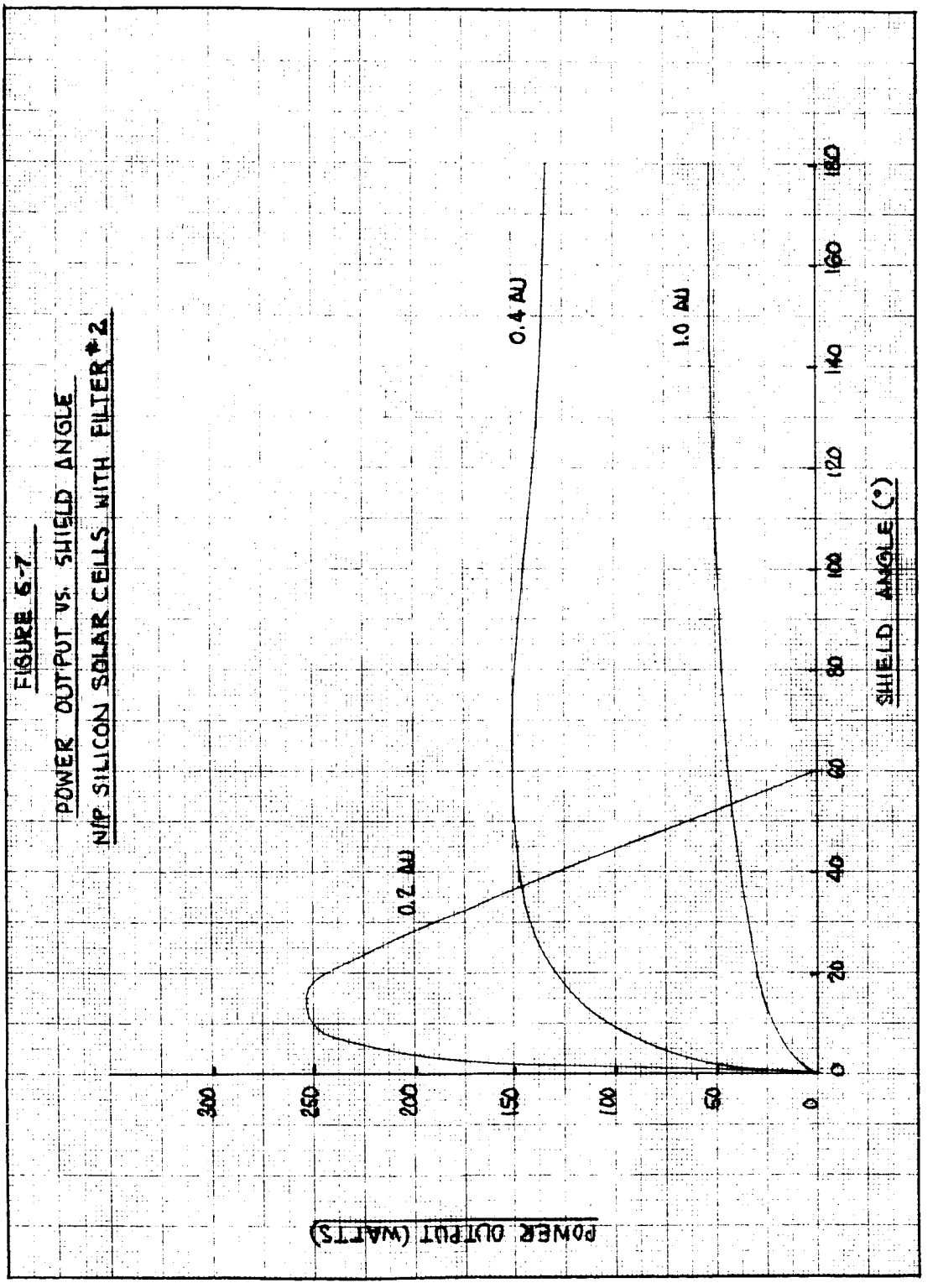
FIGURE 6-7
POWER OUTPUT VS. SHIELD ANGLE
N/P SILICON SOLAR CELLS WITH FILTER #2
0.2 AU
0.4 AU
1.0 AU
POWER OUTPUT (WATTS)
SHIELD ANGLE (°)
300
250
200
150
100
50
0
0
20
40
60
80
100
120
140
160
180

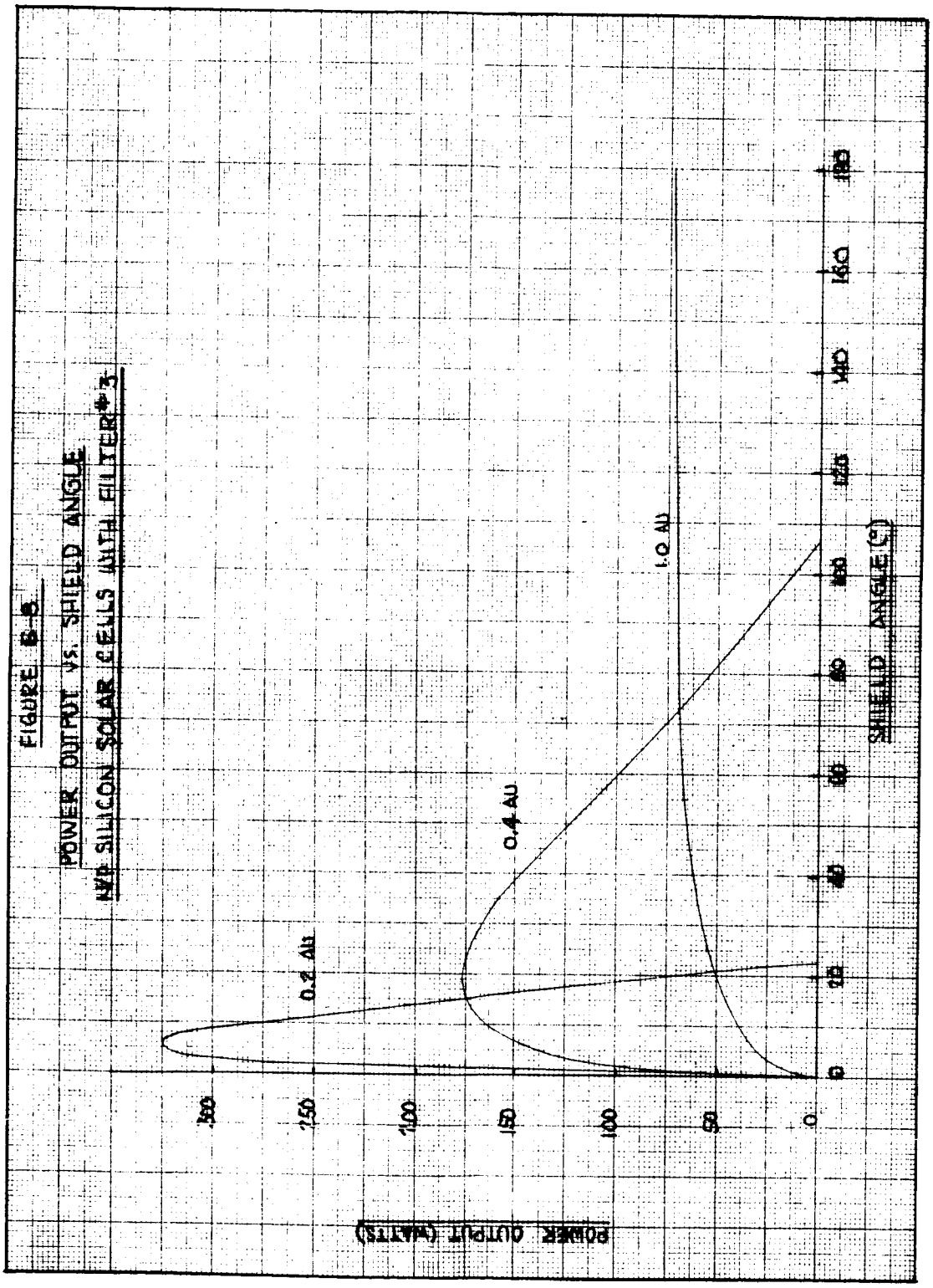

FIGURE 6-8
POWER OUTPUT VS. SHIELD ANGLE
NVP SILICON SOLAR CELLS WITH FILTER #3

Figures 6-6, 6-7, and 6-8 may be cross-plotted to obtain other useful results. Figures 6-9, 6-10, and 6-11 show the shield angle required for maximum and minimum (60 watts) power from 1.0 to 0.2 AU. Figure 6-12 provides the maximum power available from the array, for each of the filters, as a function of solar distance.

These results show that the minimum power of 60 watts can be maintained for all systems considered, and under all conditions, with the exception of operation with filter 2 at 1 AU where the corresponding power is about 52 watts. A maximum power of 325 watts at 0.2 AU can be obtained (filter 3).

FIGURE 6-9

SHIELD ANGLE vs. SOLAR DISTANCE

N/P SILICON SOLAR CELLS WITH FILTER # 1

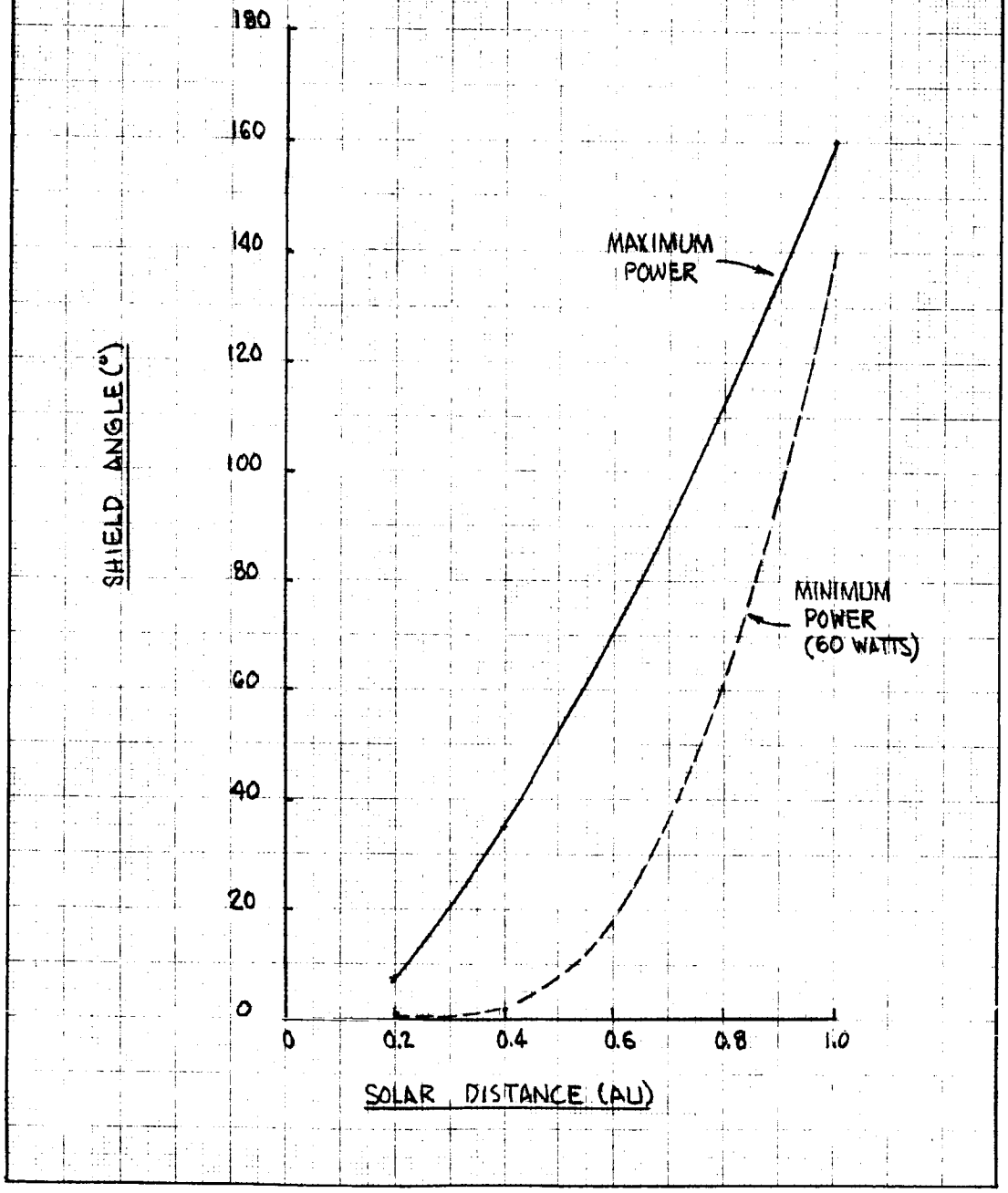

FIGURE 6-10

SHIELD ANGLE VS. SOLAR DISTANCE
N/P SILICON SOLAR CELLS WITH FILTER #2

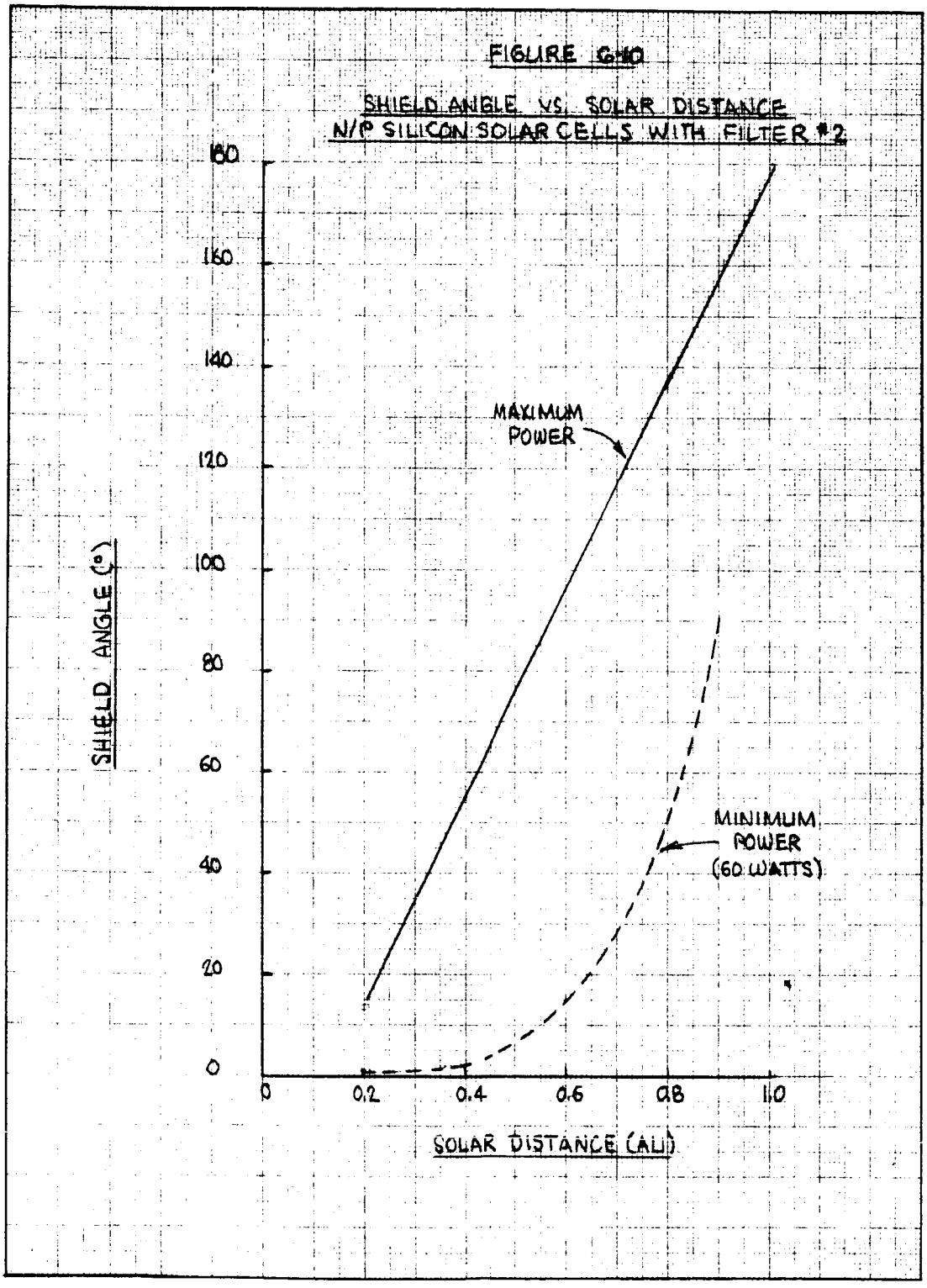

FIGURE 6-11

SHIELD ANGLE VS. SOLAR DISTANCE

N/P SILICON SOLAR CELLS WITH FILTER #3

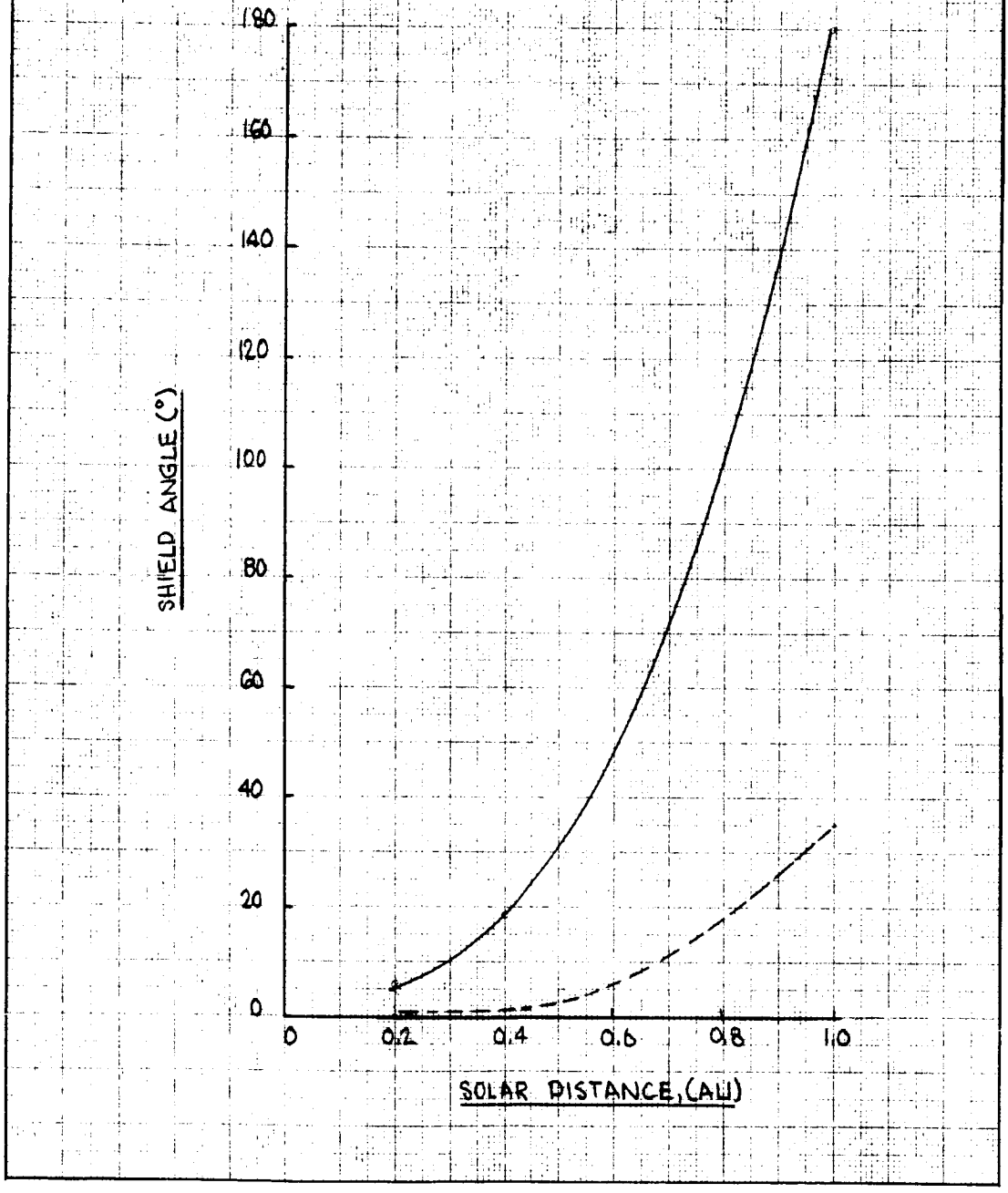

FIGURE 6-12

MAXIMUM POWER OUTPUT

vs.

SOLAR DISTANCE

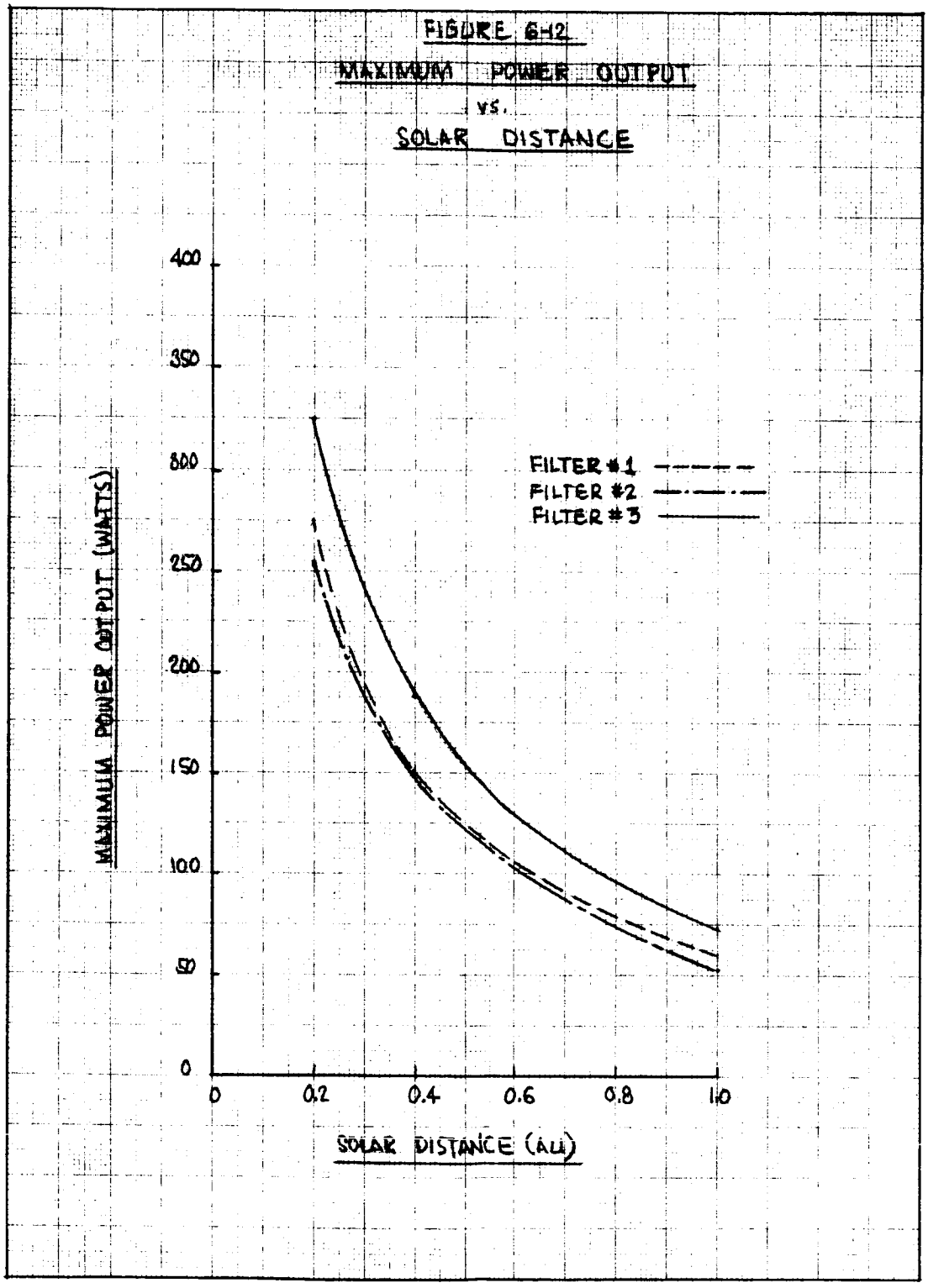

6.3 VOLTAGE-CURRENT ANALYSIS

Voltage-current curves have been obtained for the solar array with each of the three filters and as a function of shield angle and solar distance. The results of this calculation are given by Figures 6-13, 6-14, and 6-15. Appendix H provides details of the analysis from which the curves were obtained.

The given voltage-current results do not include efficiency or degradation losses. Factors causing these losses are given in Table 6-1; the assigned numerical values are approximate, based on past experience and engineering judgement. The cumulative effect of these losses can be applied to the maximum power point with the resulting degradation of the V-I curve. Degradation of 10 Ω-cm N/P silicon solar cells resulting from electron irradiation[11] is illustrated in Figure 6-16.

TABLE 6-1

ESTIMATED EFFICIENCY/DEGRADATION LOSSES
FOR N/P SILICON SOLAR CELL ARRAY

	Approximate Efficiency Factor
• Assembly losses (wiring, etc.)	0.94
• Diode losses	0.97
• Random open circuit	0.94
• UV adhesive transmission degradation	0.90
• Solar flare degradation (estimated from Fig. F-1)	0.88
• Micrometeorite erosion on cover glass	0.98
• Operating off maximum power point	0.95

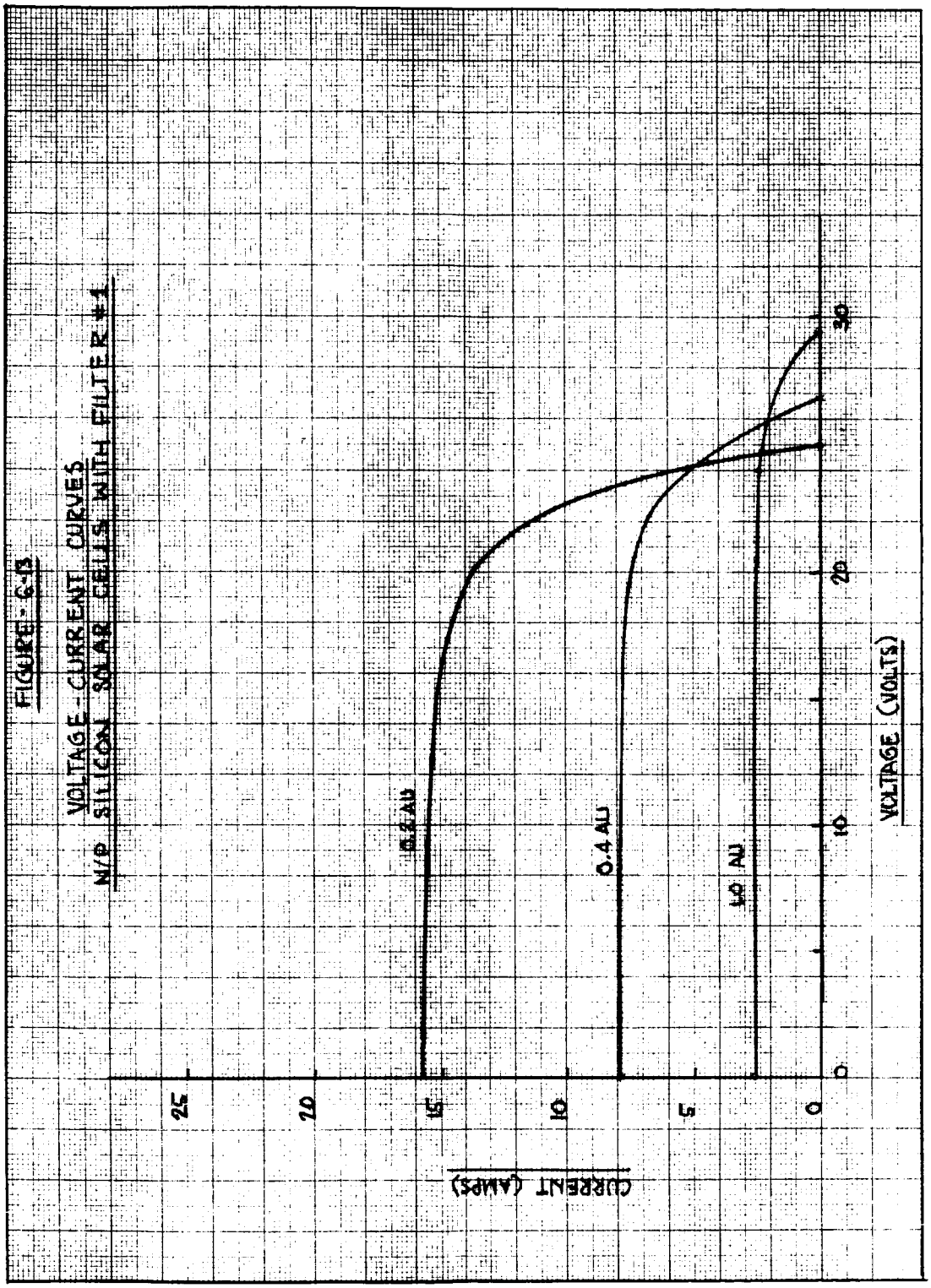

FIGURE - 6-13

VOLTAGE - CURRENT CURVES
N/P SILICON SOLAR CELLS WITH FILTER #1

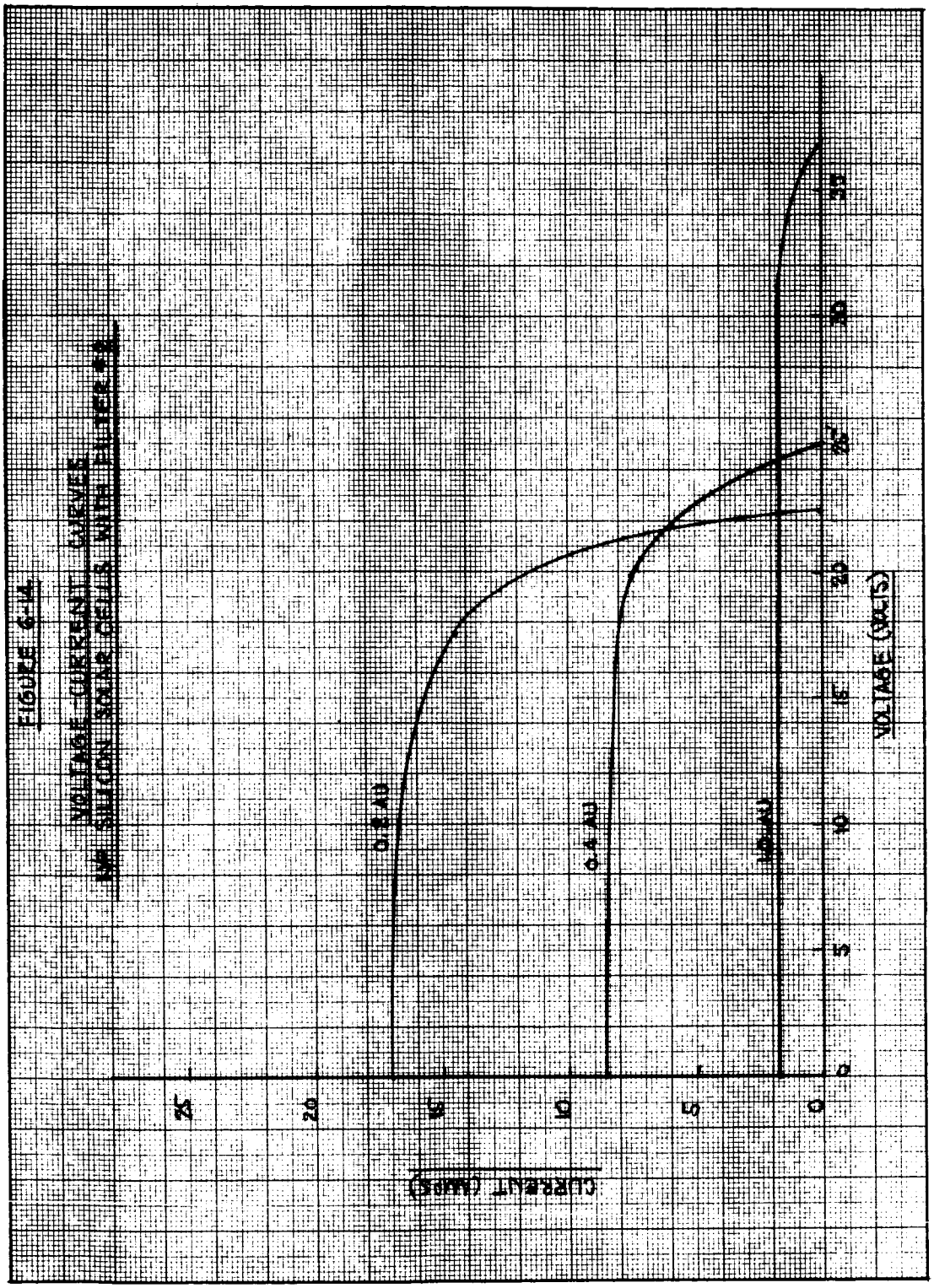
VOLTAGE-CURRENT CURVES
FOR SILICON SOLAR CELLS WITH FILTER #2
0.8 AU
0.4 AU
0 AU
VOLTAGE (VOLTS)
CURRENT (AMPS)
0
5
10
15
20
25
30
0
5
10
15
20
25

FIGURE 6-14

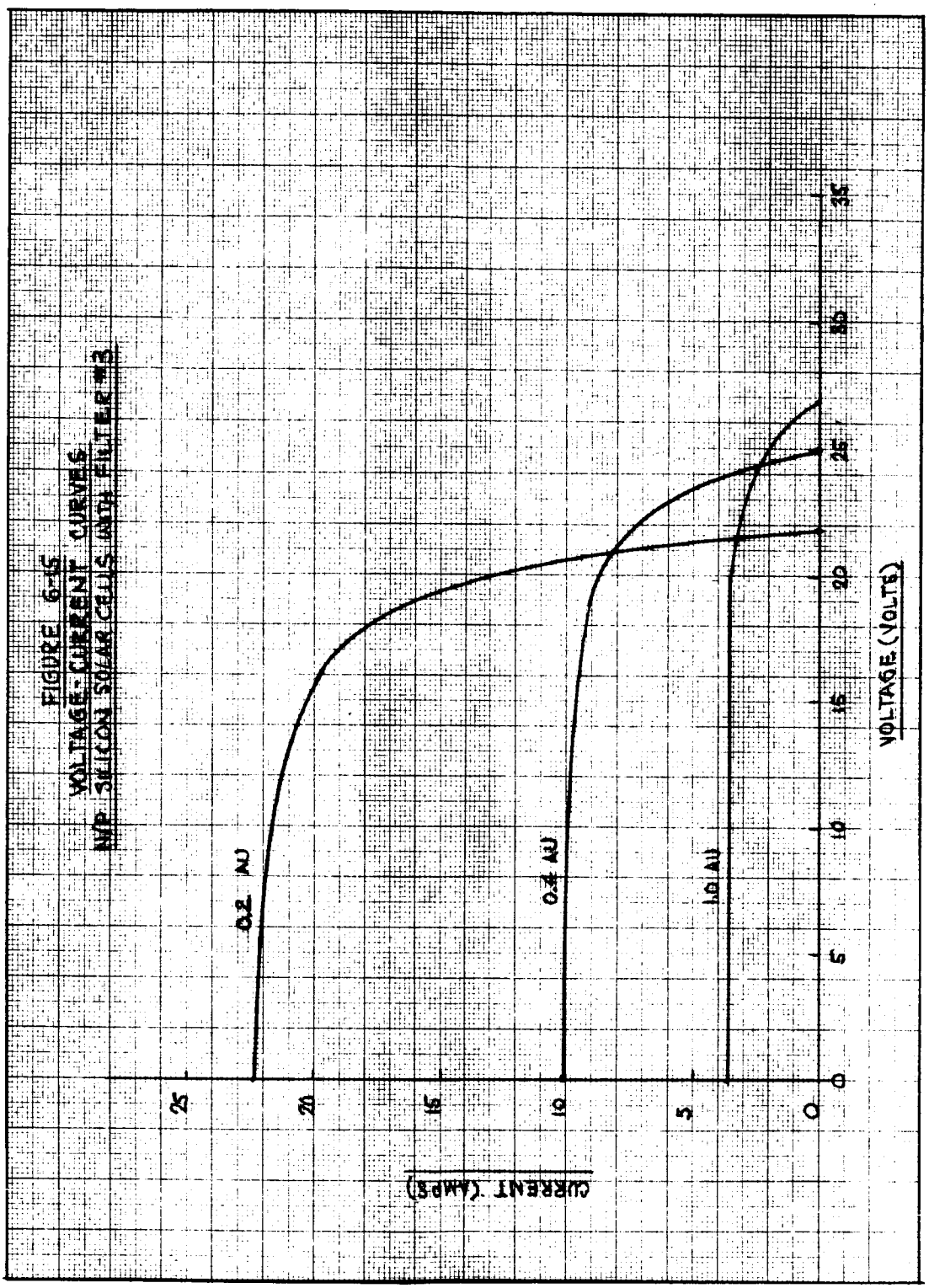
FIGURE 6-15
VOLTAGE-CURRENT CURVES
N/P SILICON SOLAR CELLS WITH FILTER #3
0.2 AU
0.4 AU
1.0 AU
CURRENT (AMPS)
VOLTAGE (VOLTS)
25
20
15
10
5
0
0
5
10
15
20
25
30
35

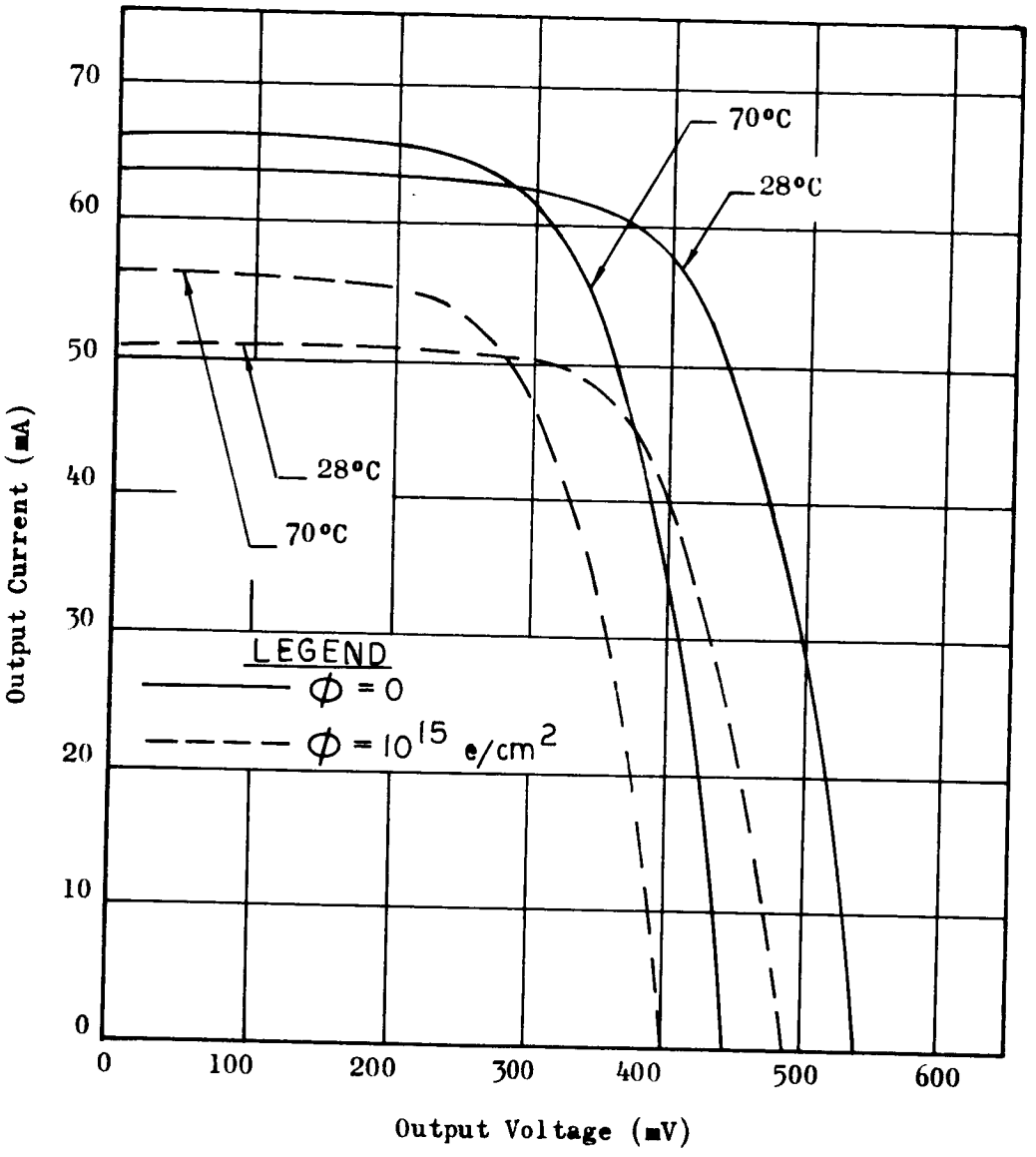

Figure 6-16

Current vs Voltage For N/P
10 Ohm-Cm Silicon Cells Before
And After 1 MEV Electron Irradiation

Source: Ref. No. 11

6.4 DISCUSSION

A number of assumptions and simplifications have been made to facilitate the power and voltage analysis of the system. Consequently, the given results should be considered as a good first approximation of the system performance.

In the present analysis, there are uncertainties resulting from a lack of knowledge of actual component (adhesives, filters, cover glasses) performance in a space environment (i.e., a vacuum with combined UV, particle, and thermal radiation).

Refinements which could be incorporated in the analysis include: using a larger number of iterations on temperature as described in Section 6.2(a); accounting for temperature dependent properties such as the shift in the spectral response, r^*_λ, with temperature; including incidence angle effects as indicated by Figure 5-7; allowing for the effects of UV and particle radiation (Figure 5-9 and Appendix E, for example); and allowing for other losses as indicated by Table 6-1. To perform such a detailed analysis, a computer code developed for this specific purpose would be required.

7.0 CONCLUSIONS AND RECOMMENDATIONS

As a result of the work reported herein, the following conclusions and recommendations are made.

7.1 Conclusions

a. Using a positionable despun thermal shield to expose body-mounted N/P Silicon solar cells at near normal (0^{o}) incidence angles, a 0.2 AU mission is feasible in terms thermal and photovoltaic performance for the spacecraft configuration specified.

b. A currently available and reliable full-cell-response bandwidth blue-red filter with a single IR suppression band (filter #3) would perform satisfactorily on the stated mission. This was the least expensive filter considered.

c. A minimum power of 60 watts and a minimum voltage of 24 volts can be maintained throughout the mission. Switching may be required to maintain the minimum voltage near the sun.

d. Near the sun, a considerable power surplus is available. A maximum power of 325 watts obtains at 0.2 AU.

e. Shield angles near the sun are small, thereby minimizing the effective exposure of the cells. Thus, incidence angle effects and solar array temperatures are minimized and photovoltaic operation is optimized.

f. As a result of the spacecraft spin rate, the solar array be essentially be isothermal.

g. The maximum temperature of the solar array will be approximately $190^{o}F$. The maximum temperature of the thermal shield will be about $380^{o}F$.

7.2 Recommendations

a. The shield configuration illustrated by Figure 4-2 should be adopted. This configuration, using two counter-rotating despun shields rotating about the spacecraft spin axis, provides the performance optimization noted in 7.1(e), above.

b. The recommended cell for the solar array is a 1 x 2 cm N/P silicon solar cell with a 10.7% conversion efficiency at 28°C and air mass zero. Should a new photovoltaic design be contemplated, a size increase to 2 x 2 cm is recommended.

c. Filter 3 is recommended (Table 5-1). This is a full-cell-response bandwidth (0.4 to 1.1 μ) blue-red filter with a single IR suppression band. For improved performance, the same filter with triple suppression should be investigated.

d. Should further and more detailed analysis of this concept be desired, it is recommended that a computer code be developed specifically for that purpose. In this manner, many of the approximations and assumptions required to facilitate the present effort would be eliminated, and a more rigorous analysis would obtain.

8.0 REFERENCES

1. Charnes, A. and Raynor, S., Solar Heating of a Rotating Cylindrical Space Vehicle, ARS Journal, May 1960.

2. Luft, W., Advanced Energy Conversion, Vol. 5, pp. 21-41, Pergammon Press, 1965.

3. Loferski, J. J., Recent Research on Photovoltaic Solar Energy Converters, Proc. of the IEEE, May, 1963.

4. Cherry, W. R., Solar Cells and the Applications Engineer, Astronautics and Aerospace Engineering, May, 1963.

5. Personal Communications: Frank Mihm, Heliotck Corp., Sunnyvale, Calif. and John Fairbanks, Philco Corp., WDL, Palo Alto, Calif., August, 1965.

6. Wolf, M., and Rauschenbach, H., Series Resistance Effects on Solar Cell Measurements, Advanced Energy Conversion, Vol. 3, pp. 455-479, Pergammon Press, 1963.

7. Neustien, J., Selected Notes on Space Power Systems, Electro-Optical Systems, Inc., Presented at Stanford University, 23 Feb., 1965.

8. Thelan, A., Multilayer Filters With Wide Transmittance Bands, Journal of the American Optical Society, Vol. 53, No. 11, Nov., 1963.

9. Fairbanks, J. W. and Hillesland, H,; Unpublished Test Data; Philco Corp., WDL, Palo Alto, California

10. Arveson, J.C., Neel, C. B., and Shaw, C. C.; Preliminary Results From A Round-Robin Study of UV Degradation of Spacecraft Thermal Control Coatings; NASA SP-55; Symposium on Thermal Radiation of Solids; San Francisco, Calif.; March, 1964.

11. Martin, J. H.; Teener, J. W., and Ralph, E.L., Some Effects of Electron Irradiation and Temperature on Solar Cell Performance, Heliotek Technical Paper B101A, 21 May, 1963.

12. McAdams, W. H., Heat Transmission, McGraw-Hill Book Co., Inc., 1954.

13. Cooley, W. C. and Janda, R. J.; Handbook of Space Radiation Effects; NASA SP-3003, Office of Scientific and Technical Information, NASA, Washington, D.C.; 1963.

14. Fairbanks, J. W. and Piccianno, W.,; Comet and Close-Approach Asteroid Mission Study, Vol. 7, Power, WDL-TR2366, Philco Corp., WDL, Palo Alto, Calif., January, 1965.

15. P. Rappaport, Solar Cells 1963 -- A Status Report, RCA Direct Energy Conversion (Company Borchure), RCA Laboratories, Princeton, N. J., April, 1964.

9.0 BIBLIOGRAPHY

1. Baker, J. K., Temperature Control Techniques for Solar Energy Converters, Tech. Report ADS-TR-61-689, Feb., 1962.

2. Kuyminski, H. W., McKendry, F. J., Oblinger, C.R., and Topfer, A. R., Development of Improved Gaillium Arsenide Solar Cells, Contract NAS 5-9006, RCA, Direct Energy Conversion Department, Mountaintop, Pa., February, 1965.

3. Loferski, J. J., Theoretical Considerations Governing the Choice of the Optimum Semiconductor for Photovoltaic Solar Energy Conversion, Journal of Applied Physics, Vol. 27, No. 7, July 1956.

4. Johnston, P.A., Laboratory Experiments on the Performance of Silicon Solar Cells at High Solar Intensities and Temperatures, NASA TN D-2733, Ames Research Center, Moffett Field, Calif., March, 1965.

5. Wise, J. F., Radiation Effects on Solar Cells, Technical Memorandum ASRPP TM 63-41, Aeronautical Systems Division, Air Force Systems Command, Wright-Patterson Air Force Base, Ohio, June, 1963.

APPENDICES

APPENDIX A

DEVELOPMENT OF EQUATIONS FOR SHIELD AND SPACECRAFT TEMPERATURE

THERMAL BALANCE

Using the assumptions stated in Section 3.0, the thermal balance on nodes 1 and 2 may be written as follows:

$$q_{s1} - \epsilon_{13} A \sigma T_1^4 - \epsilon'_{13} A' \sigma T_1^4 - \epsilon_{12} A \sigma T_1^4 + \epsilon_{21} A \sigma T_2^4 = 0$$

$$q_{s2} - \epsilon_{21} A \sigma T_2^4 - \epsilon_{23} A \sigma T_2^4 + \epsilon_{12} A \sigma T_1^4 = 0$$

or

$$q_{s1} - \left[A(\epsilon_{13}+\epsilon_{12}) + \epsilon'_{13}A'\right] \sigma T_1^4 + \epsilon_{21} A \sigma T_2^4 = 0 \qquad \text{(A-1)}$$

$$q_{s2} - (\epsilon_{21} + \epsilon_{23}) A \sigma T_2^4 + \epsilon_{12} A \sigma T_1^4 = 0 \quad . \qquad \text{(A-2)}$$

Solving (A-1) and (A-2) simultaneously for σT_2^4, we obtain,

$$\sigma T_2^4 = \frac{\epsilon_{12} A q_{s1} + \left[A(\epsilon_{13}+\epsilon_{12}) + \epsilon'_{13}A'\right] q_{s2}}{A\left\{A\left[\epsilon_{13}(\epsilon_{21}+\epsilon_{23}) + \epsilon_{12}\epsilon_{23}\right] + \epsilon'_{13}A'(\epsilon_{21}+\epsilon_{23})\right\}} \qquad \text{(A-3)}$$

which, upon substitution into (A-1), yields

$$\sigma T_1^4 = \frac{(\epsilon_{21} + \epsilon_{23}) A \sigma T_2^4 - q_{s2}}{\epsilon_{12} A} \qquad \text{(A-4)}$$

In equations (A-1) and (A-2), it was assumed that the proximity of the shield to the satellite yields a geometric configuration factor of unity and that the emittance terms ϵ_{12} and ϵ_{21} are effective emittances -- i.e., functions of the surface areas and emittances of the nodes. The area A' is the area of the ends of the cylinder ($2\pi r^2$) while ϵ'_{13} is the hemispherical emittance of these surfaces. The area A is one-half the surface of revolution of the cylinder (πrh). Thus, A is also the surface area of either side of the shield.

The effective emittances may be expressed[13] as

$$\epsilon_E = \epsilon_{12} = \epsilon_{21} = \left[\frac{1}{\frac{1}{\epsilon_1} + \frac{1}{\epsilon_2} - 1}\right] \tag{A-5}$$

Equations (A-3) and (A-4) may now be slightly simplified:

$$\sigma T_2^4 = \frac{\epsilon_E A q_{s1} + \left[A(\epsilon_{13} + \epsilon_E) + \epsilon'_{13} A'\right] q_{s2}}{A\left\{A\left[\epsilon_E(\epsilon_{13} + \epsilon_{23}) + \epsilon_{13}\epsilon_{23}\right] + \epsilon'_{13} A'(\epsilon_E + \epsilon_{23})\right\}} \tag{A-6}$$

$$\sigma T_1^4 = \frac{(\epsilon_E + \epsilon_{23}) A \sigma T_2^4 - q_{s2}}{\epsilon_E A} \tag{A-7}$$

PROJECTED AREAS

Configuration 2, as illustrated by Figure 3-1, was used as the model for the thermal analysis. The projected areas of the spacecraft and thermal shield (as viewed along a spacecraft-sun line perpendicular to the spacecraft spin axis) are determined below for this model.

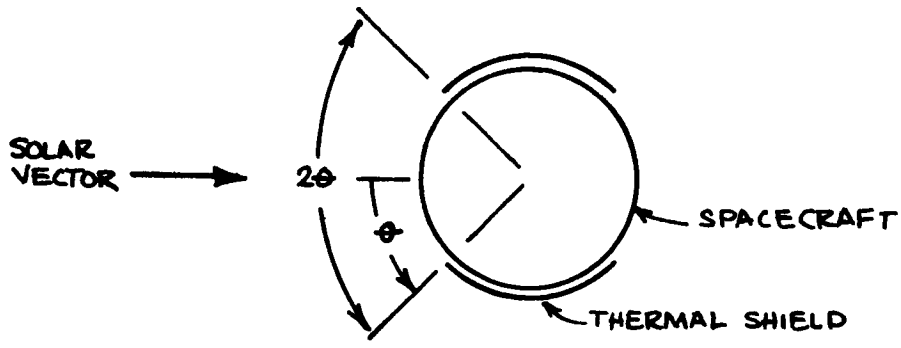

For the satellite:

$$A_{P_1} = 2rh \sin\theta \qquad \text{(A-8)}$$

For the shield:

$$A_{P_2} = 2h\,(r - r\sin\theta)$$

$$= 2hr\,(1 - \sin\theta) \qquad \text{(A-9)}$$

APPENDIX B

NUMERICAL EVALUATION OF TEMPERATURE GRADIENTS DUE TO THE SPINNING OF THE SPACECRAFT

The following parameters apply to the case being considered:

$r = 1.5$ ft.

$\alpha = 0.56$

$S = 442$ Btu/hrft^2

$t = 0.00167$ ft (0.020 in.)

$k = 100$ Btu/hrft$^\circ$ R

$V = 60$ RPM $= 2\pi\,(1.5)\,(60)\,(60) = 3.39 \times 10^4$ ft/hr

$\epsilon = 0.875$

Using these values,

$$d = \frac{k}{\rho c_p} = 2.7 \text{ ft}^2/\text{hr}$$

$$\sigma T_o^4 = \frac{\alpha S}{\pi \epsilon} = 90.1$$

$$T_o = 479^\circ R$$

$$\rho_o = \left[\frac{16 r^2 \pi \alpha S}{t k T_o}\right]^{1/2} = 18.7$$

$$V_o = \frac{V \pi r}{d \rho_o} = 3160$$

Obviously, $V_o^2 >> 1$ and $V_o \rho_o >> \pi^2$. Thus, the simplified form of the solution may be applied.

For the region in which $3/4 < \eta < 1$,

$$T = T_o \left\{1 + \frac{\rho_o}{16 V_o}\left[2(\eta - 1) + \frac{\rho_o}{2 V_o}(\eta - 1)^2 - \sin(2\pi\eta - \phi)\right]\right\}$$

where

$$\phi = \tan^{-1} \frac{(\rho_o/2\pi)^2 + 1}{2V_o(\rho_o/2\pi)}$$

In the present case, $\rho_o/2\pi = 2.98$ and

$$\phi = \tan^{-1} 5.25 \times 10^{-4}$$

$$\phi \approx 0^o$$

Thus,

$$T = T_o\left\{1 + \frac{\rho_o}{16V_o}\left[2(\eta-1) + \frac{\rho_o}{2V_o}(\eta-1)^2 - \sin(2\pi\eta)\right]\right\}$$

Inserting the values of the parameters given above

$$T = T_o\left\{1 + 7.4\times10^{-4}(\eta-1) + 1.1\times10^{-6}(\eta-1)^2 - 3.7\times10^{-4}\sin 2\pi\eta\right\}$$

which is equation (2-7).

APPENDIX C

RADIAL TEMPERATURE GRADIENTS IN THE THERMAL SHIELD

The temperature drop in the thermal shield has been determined for shield angles of 0° and 180°. A detailed analysis for the 180° case is given below; the 0° case is similar. Results for both cases are presented in Table 3-1.

Using the assumptions of Section 3.0, and neglecting axial and circumferential gradients in the thermal shield, the following thermal network may be drawn:

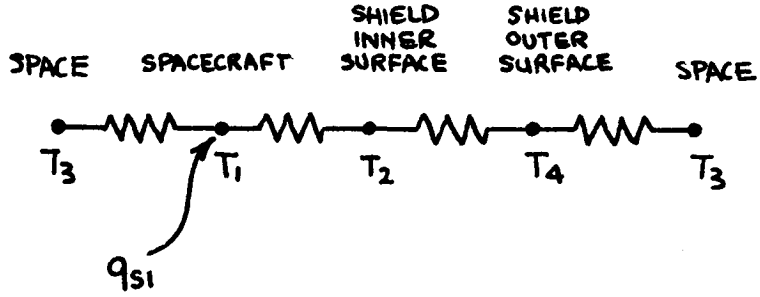

The thermal balance equations are*

$$q_{s1} - \sigma \epsilon_{13} A_1 T_1^4 - \sigma \epsilon_E A_1 (T_1^4 - T_2^4) = 0 \qquad \text{(Node 1)}$$

$$\sigma \epsilon_E A_1 (T_1^4 - T_2^4) - \sigma \bar{\epsilon} A_1 (T_2^4 - T_4^4) = 0 \qquad \text{(Node 2)}$$

$$\sigma \bar{\epsilon} A_1 (T_2^4 - T_4^4) - \sigma \epsilon_{43} A_1 T_4^4 = 0 \qquad \text{(Node 3)}$$

---

* Parameters are as defined in Section 3.0. $\bar{\epsilon}$ is the effective emissivity of the superinsulation shield -- corresponding to an effective thermal conductivity of 0.005 Btu/hr ft^2($^{\circ}$F/in).

or

$$(\epsilon_{13}+\epsilon_E)\,\sigma T_1^4 - \epsilon_E\,\sigma T_2^4 = q_{s1}/A$$

$$\epsilon_E\,\sigma T_1^4 - (\epsilon_E+\bar{\epsilon})\,\sigma T_2^4 + \bar{\epsilon}\,\sigma T_4^4 = 0$$

$$\bar{\epsilon}\,\sigma T_2^4 - (\bar{\epsilon}+\epsilon_{43})\,\sigma T_4^4 = 0$$

In matrix notation

$$\begin{bmatrix} (\epsilon_{13}+\epsilon_E) & -\epsilon_E & 0 \\ \epsilon_E & -(\epsilon_E+\bar{\epsilon}) & \bar{\epsilon} \\ 0 & \bar{\epsilon} & -(\bar{\epsilon}+\epsilon_{43}) \end{bmatrix} \begin{bmatrix} \sigma T_1^4 \\ \sigma T_2^4 \\ \sigma T_4^4 \end{bmatrix} = \begin{bmatrix} q_{s1}/A \\ 0 \\ 0 \end{bmatrix}$$

Using Cramer's Rule, we have

$$\sigma T_1^4 = \frac{\begin{vmatrix} q_{s1}/A & -\epsilon_E & 0 \\ 0 & -(\epsilon_E+\bar{\epsilon}) & \bar{\epsilon} \\ 0 & \bar{\epsilon} & -(\bar{\epsilon}+\epsilon_{43}) \end{vmatrix}}{\begin{vmatrix} (\epsilon_{13}+\epsilon_E) & -\epsilon_E & 0 \\ \epsilon_E & -(\epsilon_E+\bar{\epsilon}) & \bar{\epsilon} \\ 0 & \bar{\epsilon} & -(\bar{\epsilon}+\epsilon_{43}) \end{vmatrix}}$$

$$= \frac{q_{s1}/A\,\left[\epsilon_E(\bar{\epsilon}+\epsilon_{43})+\bar{\epsilon}\,\epsilon_{43}\right]}{\epsilon_E\,\bar{\epsilon}\,(\epsilon_{13}+\epsilon_{43})+\epsilon_{13}\,\epsilon_{43}(\epsilon_E+\bar{\epsilon})}$$

and, similarly

$$\sigma T_2^4 = \frac{q_{s1}/A \left[\epsilon_E (\bar{\epsilon} + \epsilon_{43})\right]}{\epsilon_E \bar{\epsilon} (\epsilon_{13} + \epsilon_{43}) + \epsilon_{13} \epsilon_{43} (\epsilon_E + \bar{\epsilon})}$$

$$\sigma T_4^4 = \frac{q_{s1}/A (\bar{\epsilon} \epsilon_E)}{\epsilon_E \bar{\epsilon} (\epsilon_{13} + \epsilon_{43}) + \epsilon_{13} \epsilon_{43} (\epsilon_E + \bar{\epsilon})}$$

The parameters used in the computation were

ϵ_{13} = 0.875

ϵ_E = 0.0496

$\bar{\epsilon}$ = 0.005

ϵ_{43} = 0.80

A = 11.78 ft^2

As shown by Table 3-1, the effect of considering the temperature drop through the shield is to increase the temperature extremes the spacecraft will experience. The upper limits are increased only slightly while the lower limits drop significantly.

APPENDIX D

THIN FILM SOLAR CELLS

The attractiveness of thin film solar cells lies in the possibility of achieving reasonabley efficient cells with large area and low weight, resulting in increased power to weight ratio and decreased production and assembly costs. To date, attention has centered on the compounds: cadium telluride (CdTe), cadmium sulfide (CdS), and gallium arsenide (GaAs). Since the heteroepitaxial growth of highly perfect single crystal thin films presents a formidable problem, the great majority of work has been in the development of polycrystalline thin film solar cells. A notable exception is discussed in (b), below.

(a). Polycrystalline Thin Film Solar Cells. Thin film polycrystalline CdS and CdTe solar cells have shown considerable promise. Large area (56 cm^2) CdTe cells with conversion efficiencies approaching 5% have been reported. CdS cells, 3 x 3 in., have shown an average efficiency of 3% and smaller area cells have demonstrated efficiencies up to 6%. Comparable success with polycrystalline thin film GaAs cells has not been realized.

Although preliminary and incomplete investigation has indicated that both CdTe and CdS cells possess promising radiation resistance performance characteristics, environmental deterioration may be a serious drawback to their use. Encapsulation retards this effect, but offers only a partial solution to the problem since darkening of the encapsulating material results following ultra-violet exposure.

(b). Single Crystal Thin Film GaAs Solar Cells. Large area polycrystalline thin films can be grown quite readily. However, the inherently poor crystalline quality of such a film makes the achievement of solar cells with efficiencies exceeding 5 to 6% very doubtful. Perfection of the film will lead to considerably higher efficiencies.

Recently, the Philco Corporation has succeeded in growing, on germanium (Ge) substrates, thin films of GaAs with crystalline characteristics as good as, or exceeding, those of commercially available bulk GaAs. Small area solar cells have been produced successfully from this material and have demonstrated performance characteristics comparable to those from bulk GaAs. Since the GaAs film thickness is approximately 10 microns, and since the Ge substrate is relatively inexpensive, further development should result in single crystal thin film GaAs solar cells retaining all the advantages of the bulk GaAs cells, but at a small fraction of their cost.

APPENDIX E

RADIATION EFFECTS

Certain radiation effects on solar array components are discussed below.

a) Radiation Resistance

The relative radiation resistance between N/P and P/N silicon solar cells is illustrated in Figure E-1 using a criterion of critical flux under electron bombardment[2] (critical flux is defined as the particle dose causing a 25% power reduction). N/P cells demonstrated about 30 to 100 times more resistance to electrons (in the energy range: $0.2 < E_p < 0.8$ MEV) than similar P/N cells[3]. Irradiation with proton fluxes ($8 < E_p < 20$ MEV) indicated that the P/N cells decayed 3 to 10 times more than the N/P.

Threshold energy is the lowest particle energy which causes damage to a solar cell. The threshold energy for P/N cells is approximately 170 KEV electrons; the corresponding value for N/P cells is about 250 KEV electrons[4].

Up to a certain dosage, GaAs solar cells have a higher radiation resistance to high energy particles. GaAs provides nearly an order of magnitude improved resistance to high energy particles until the proton flux reaches a level of approximately 3×10^{12} protons/cm^2 for 17 MEV protons, at which level it experiences a catastrophic degradation (Figure E-2). Thus, the specification of cover slide thickness is critical for GaAs.

b) Radiation Damage

In silicon solar cells, radiation damage causes dislocations in the silicon material; thereby, reducing the minority carrier lifetime. In turn, this reduces response to long wavelength radiation (Figure E-3) and short circuit current. A cell utilizing filter 1, with a transmission cut-off at

FIGURE E-1

COMPARISON OF N/P AND P/N SILICON SOLAR CELLS

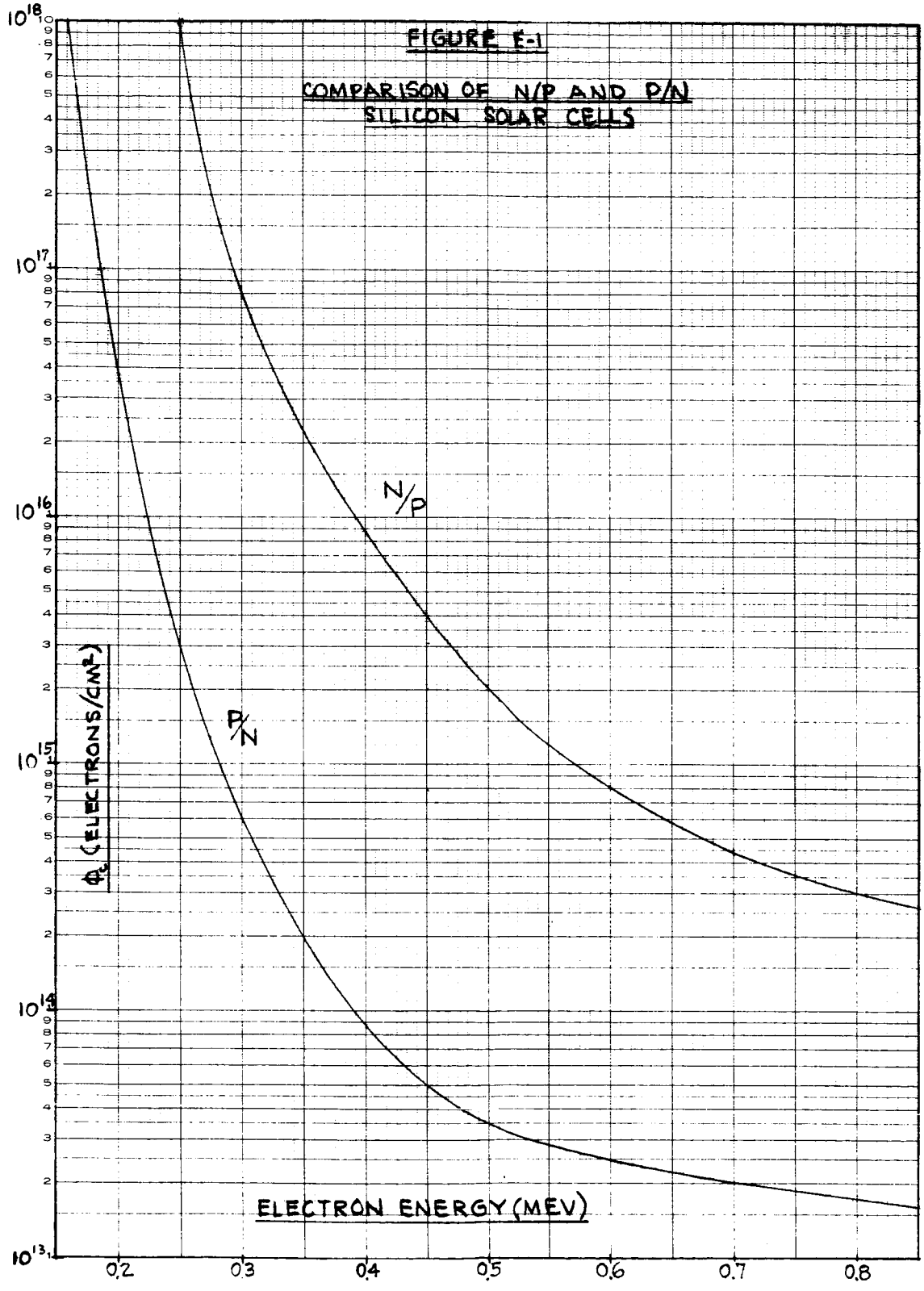

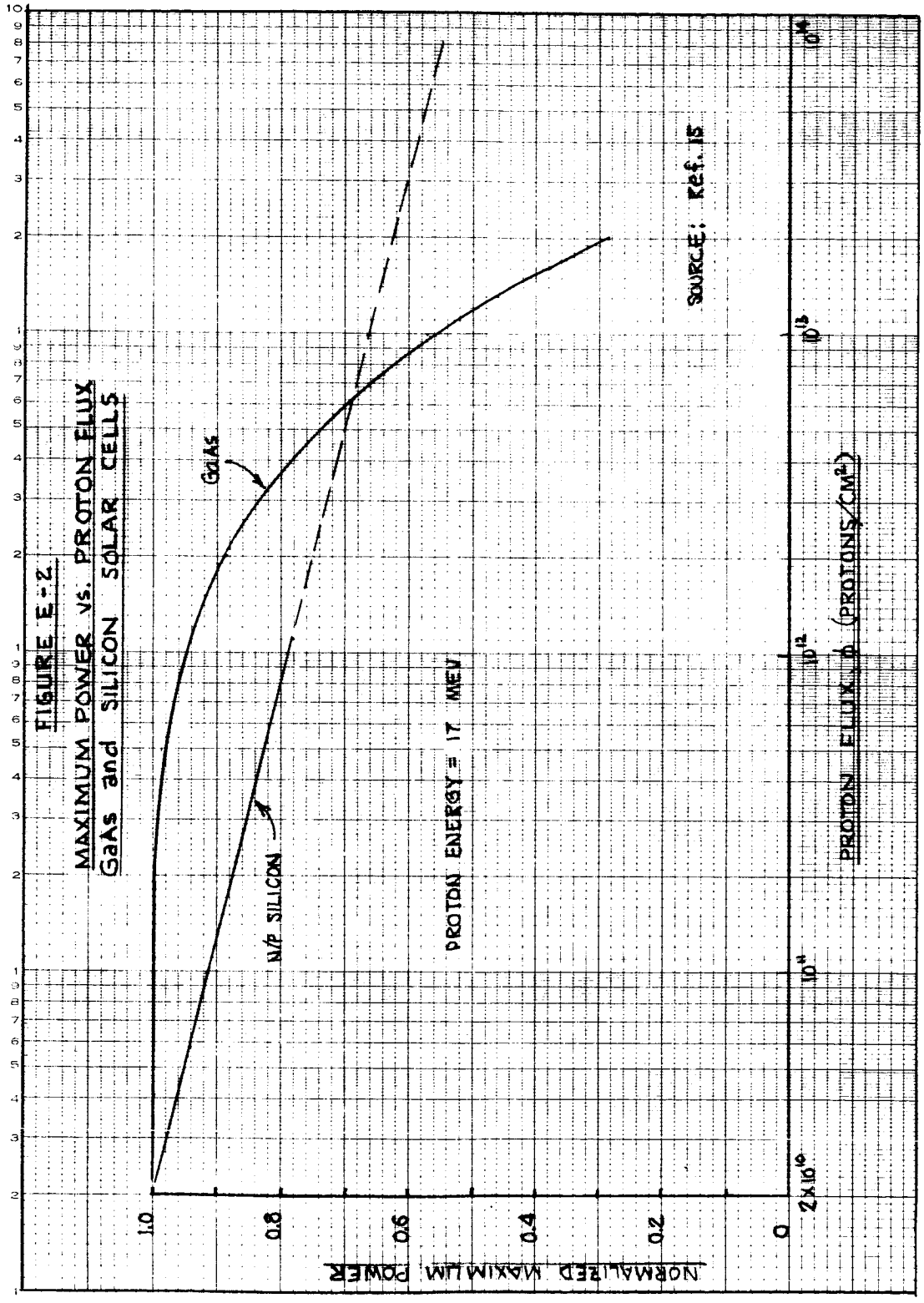
FIGURE E-2
MAXIMUM POWER vs. PROTON FLUX
GaAs and SILICON SOLAR CELLS
GaAs
N/P SILICON
PROTON ENERGY = 17 MEV
SOURCE: Ref. 15
NORMALIZED MAXIMUM POWER
PROTON FLUX, Φ (PROTONS/CM²)
1.0
0.8
0.6
0.4
0.2
0
2 X 10¹⁰
10¹¹
10¹²
10¹³
10¹⁴

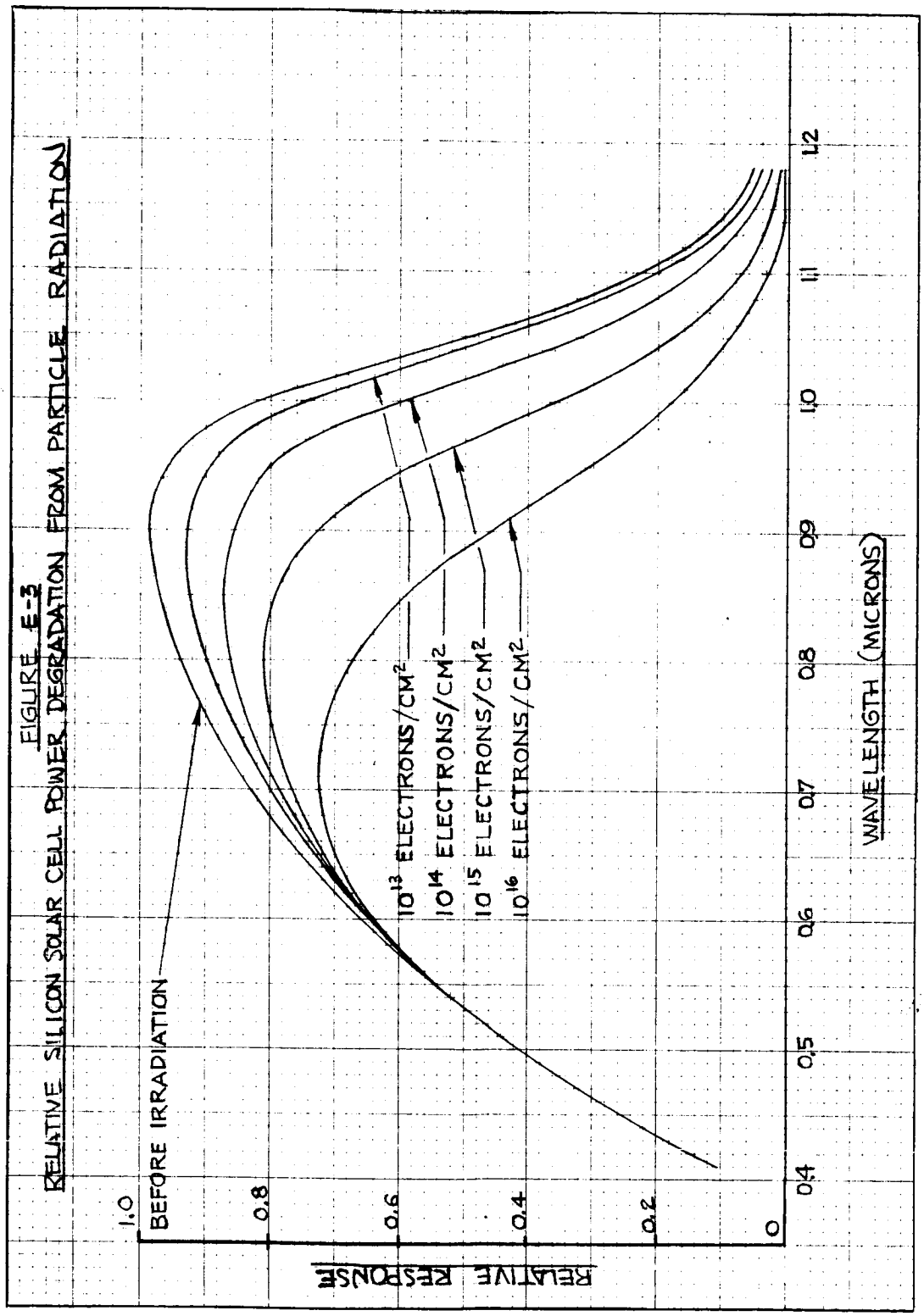
FIGURE E-3
RELATIVE SILICON SOLAR CELL POWER DEGRADATION FROM PARTICLE RADIATION
RELATIVE RESPONSE
1.0
0.8
0.6
0.4
0.2
0
BEFORE IRRADIATION
10^{13} ELECTRONS/CM^2
10^{14} ELECTRONS/CM^2
10^{15} ELECTRONS/CM^2
10^{16} ELECTRONS/CM^2
0.4
0.5
0.6
0.7
0.8
0.9
1.0
1.1
1.2
WAVELENGTH (MICRONS)

0.82 μ, will be less susceptible to power degradation than a cell with either a full-cell-response bandwidth filter or a narrow bandpass filter predominately in the longer wavelength response region.

Electron and proton radiation will effect the cover slide material, the multilayer interference filter, and the optical adhesive. The major radiation effect on the cover slides and adhesives appears to be in the form of color-absorbing structural defects which decrease the transmitted energy to the cell. A particle radiation dose of 10^6 ergs/gm turns most glasses brown in the visible portion of the spectrum and develops additional absorption bands in the UV region. A dose of 10^8 ergs/gm severely downgrades the coverglass slide transmissivity and significantly increases the thermal absorptance of the cell stack. A mission in an environment of peak solar activity for a year might encounter a dose as high as 10^7 ergs/gm*; however, this is improbable, and several years of exposure would probably be necessary before cover slide transmission degradation would become significant. Some optical adhesives exhibit a spectrally selective radiation degradation to the transmissive characteristic which is unfortunately severe and nonuniform in the cell's response wavelengths.

---

* A giant solar flare would give a dose of approximately 10^7 ergs/gm; an "average" solar flare would result in a dose between 10^5 and ^{6} ergs/gm. See Appendix F.

APPENDIX F

CALCULATIONS OF SOLAR CELL POWER DEGRADATION DUE TO PARTICLE RADIATION

The degradation of solar cell power as a result of exposure to particle radiation from a giant solar flare environment is estimated below.

a) Results of Degradation Calculations

Figure F-1 shows the maximum power ratio, P_m/P_{mO}, for N/P solar cells after the total irradiation of one giant solar flare (July 14, 1959) calculated without omnidirectional corrections. This calculation, depicted in the solid line curve, is based on work described in Reference 14 and was calculated manually using three residual spectrum points and normally incident irradiation. The broken-line curves are based on detailed computer calculations and include all the known omnidirectional corrections and effects. The current situation, however, is that only one point (20-mil silicon dioxide shield) has been rigorously computer calculated. The shape of the curve between 15 and 100 mils has only been estimated, based on the old curve, and must be considered with appropriate uncertainty.

b) Method of Calculation and Description of Computer Program

The COMPOSER (Computer Processing of Space Environmental Radiation) program is a collection of digital computer subroutines connected to provide an efficient calculation of space radiation problems. Entrance to the electron or proton shielding routines may be made either with a list of monoenergetic energy groups containing a certain number of charged particles, or with an interpolation subroutine. The latter approach may be accomplished very quickly, and the resulting inaccuracies are usually within the uncertainties involved with space radiation spectra. Three to ten data points are read off the given integral spectrum and given as inputs to the interpolation routine. Working in groups of three (starting with the low-energy point) the computer fits a hyperbola to the data points.

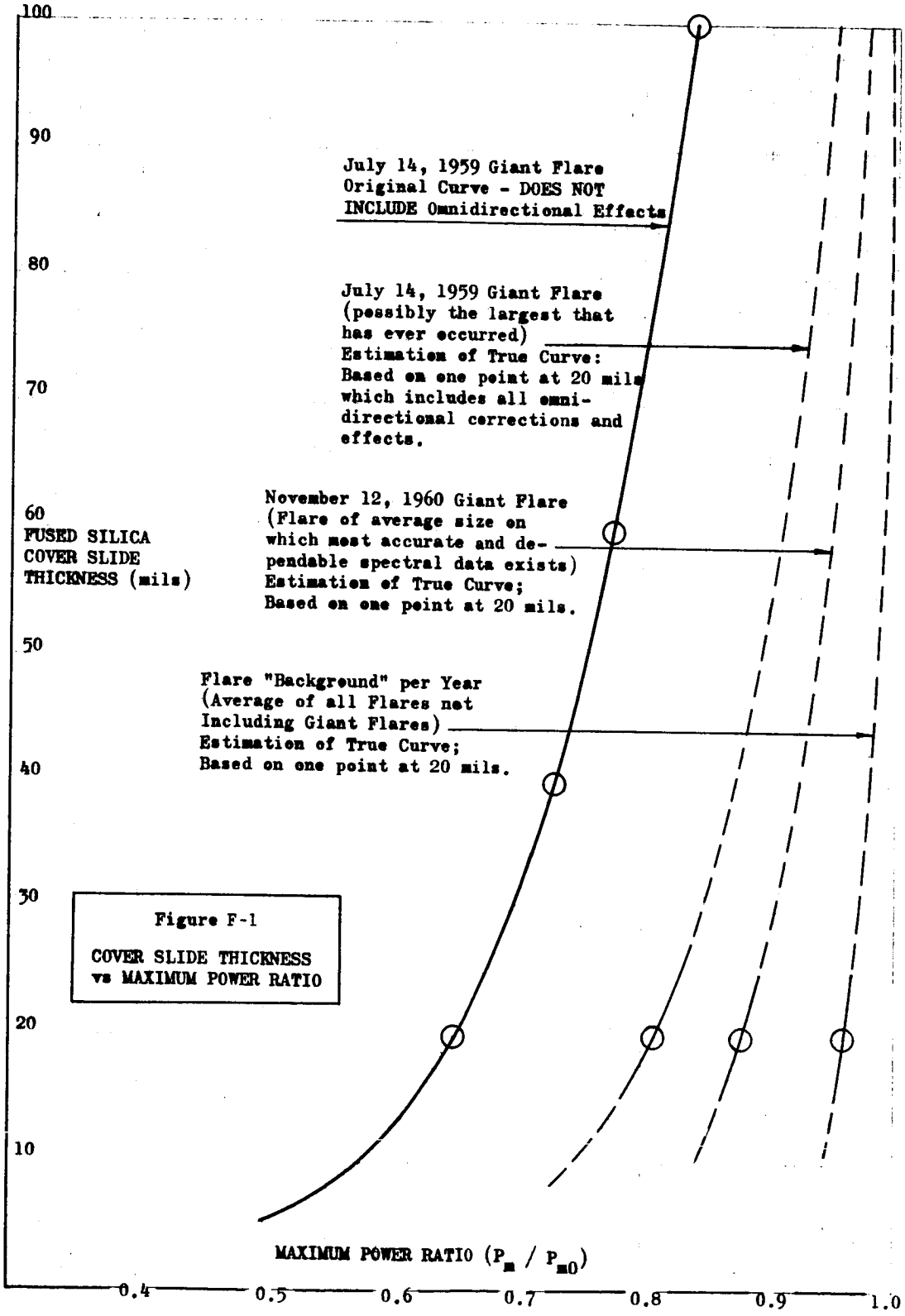

Figure F-1

COVER SLIDE THICKNESS vs MAXIMUM POWER RATIO

There will thus be a discontinuity in the slope every three points. The spread in energy between the first and last data point is divided, linearly or logarithmically, into 200 (or less) intervals. Values of integral intensity are then derived from the hyperbolas and listed beside the midpoint energy of the interval. The difference between the integral intensitities at the endpoints of each interval is calculated and is a measure of the number of particles in that interval. The shielding routine uses this number, and treats this group of particles as monoenergetic, with an energy equal to the midpoint energy.

The shielding routine calculates the energy of particles which penetrate a layer of shield whose extent is less than the cutoff range of the incident radiation. Secondary interactions and nuclear events are not included beyond those which are inherent in range-energy data. From range-energy curves, we can obtain $R = R(E)$ and the inverse relation, $E = E(R)$. If particles of energy E_o are incident on a shield layer of thickness, t, and density, ρ, with range-energy relations R vs E, then the emerging energy, E_1, after shielding is expressed:

$$E_1 = E\left(R(E_o) - t\rho\right) .$$

The value of E_1 is set identically to zero if $t\rho \geq R(E_o)$, indicating that all particles are stopped in that layer. The number of particles emerging with energy E is assumed equal to the number originally incident with energy E_o. The computer carries out a sequence of these calculations until each layer of shield between space and a selected internal point (the sensitive layer of the solar cell) has been treated. Values of the range-energy relations for aluminum and fused silica used in this program are as follows:

$$E(R) = 28.4\, R^{0.593} \qquad R(E) = 3.52 \times 10^{-3}\, E^{1.685}.$$

The shielding routine uses each energy group from the interpolation subroutine in an equivalent manner. The solar cell is assumed shielded by six concentric regions of the cover glass, and back-shielded by 3.0 cm of aluminum representing the vehicle. Any radiation penetrating the various regions is multiplied by the fraction of solid angle associated with that region. Since the sensitive layer in the solar cell is approximately planer, the distribution is proportional to $\sin\theta \cos\theta \, d\theta$. The resultant 200 x 7 intensity groups are sorted by the computer in order of increasing energy, collected in new groups (distributed either linearly or logarithmically), and printed-out opposite the mid-point energy of the new groups. A sum of intensities between energies E and E(max) is also made and provides the integral spectrum output of the shielding routine. Figure F-2 shows the external spectrum assumed for the July 14, 1959 giant solar flare, and the spectrum beneath the silica as calculated by COMPOSER.

According to data, such as that of Cooley and Janda[15], the ratio of maximum power after irradiation to maximum initial power, P_m/P_{mO}, is related to the ratio of final to initial diffusion lengths in the n layer, the junction, and the p layer. The p layer, or the minority carrier diffusion length, dominates since the junction is small and the n layer is heavily doped and thus much less sensitive. The radiation is producing traps (irregulatities in the crystal structure) which are most effective in reducing cell output when they are formed immediately below the junction in the base region. This region has been referred to as the "sensitive layer". The initial diffusion length, L_o, is a property of the particular solar cell, and is usually in the range of 150 - 275 microns. The effect of proton irradiation on diffusion length is determined approximately from the following relation:

$$L^{-2} = L_o^{-2} + \sum_E k_p (E) \, N(E)$$

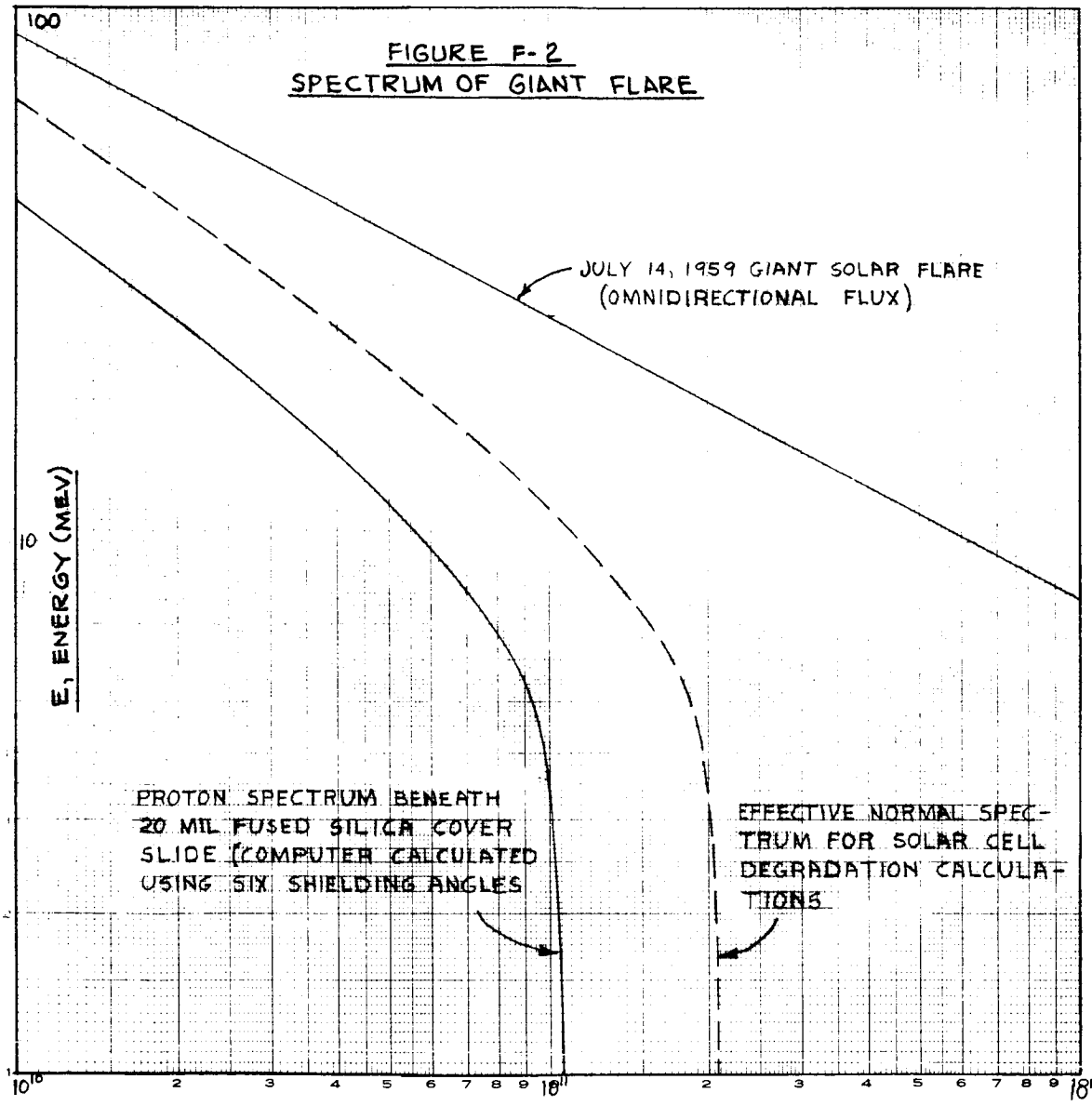

FIGURE F-2
SPECTRUM OF GIANT FLARE

where L is the final diffusion length, $k_p(E)$ the experimentally determined energy-dependent damage coefficient, and N(E) the total number of protons incident on a square centimeter with energy E.

The COMPOSER program has fit all of Cooley's empirical curves with functional relations that are correct to 0.1% in the regions of interest. Differential spectral data are utilized directly from the shielding subroutine and the maximum power ratio calculated as a function of time.

c) Omnidirectional Effects and Corrections

Omnidirectional spectral data has been divided by a factor of 2 to produce the number of protons incident on both sides of a planer square centimeter. The radiation, after shielding, which finally reaches the sensitive layer of the cell has been doubled. This can be shown to take into account the situation that radiation traversing the sensitive layer at an angle spends more time in the layer (thus causing more damage) than radiation incident normally.

d) Limitations on Accuracy

There is scatter over a factor of 2 in proton damage data. Data in Cooley and elsewhere comes from many space program investigations and represents cells from many manufacturers. A factor of 2, either in the damage coefficient or in intensity of irradiation, propagates to a 3% uncertainty in the resulting ratio of maximum power points. Thus, an equally thorough analysis made elsewhere could differ by $\pm$3-5%. There appears to be little justification, however, for any alternative theoretical treatments; and the next degree of certainty can only come from component irradiation or telemetry data.

There are also limitations to directly using maximum power point ratios to predict end-of-mission available power, especially when long mission times or extremely intense radiation is involved. The design of a solar array power system for a vehicle must take into consideration far more than

simply maximum power degradation. Temperature variations, for instance, radically reshape I-V curves over an orbit, and power control units usually operate at constant voltage, constant current, or constant load off the array output. Thus, in general the ratio P_m/P_{m0} a function of cover slide thickness is a good theoretical estimation of power. For a particular spacecraft, orbital conditions and power control parameters can be included for a higher degree of accuracy.

APPENDIX G

DETERMINATION OF THE THERMAL ABSORPTANCE VALUE FOR THE SOLAR CELL-ADHESIVE-FILTER COMBINATION

The efficiency of silicon solar cells is approximately an inverse function of temperature, approaching zero at 868°R (209°C). Thus, under very intense insolance it is necessary to utilize some thermal control technique for solar array operation. The most influential thermal design parameter for the solar cell-filter-adhesive combination (the cell stack) is the ratio, α/ε. A low value is desirable.

Consider the thermal absorptance of the cell stack

$$\alpha_{Zt} = \alpha_{ZA} - \eta_F \qquad \text{(G-1)}$$

where

α = absorptivity, the fraction of the incident radiation absorbed

η = solar cell conversion efficiency.

with the subscripts

Z = cell stack

A = total

F = filtered (filter bonded to surface)

t = thermal

The total absorptivity of the cell stack can be defined as

$$\alpha_{ZA} \quad \frac{\int_0^\infty (\alpha_{ZA})_\lambda S_\lambda \, d\lambda}{\int_0^\infty S_\lambda d\lambda} \qquad \text{(G-2)}$$

Applying conservation of energy with the assumption of an opaque cell stack

$$(\alpha_{ZA})_\lambda = 1 - (\rho_{ZA})_\lambda \qquad \text{(G-3)}$$

where

S_λ = solar spectral distribution (power per unit area per unit wavelength band) Johnson's curve is used herein.

ρ = reflectivity, the fraction of incident energy reflected.

λ = wavelength

An approximate solution can be obtained by integrating over finite intervals as follows:

$$\alpha_{ZA} = \frac{\sum_{\lambda=0}^{\infty} \left[1 - (\rho_{ZA})_\lambda\right] S_\lambda d\lambda}{\sum_{\lambda=0}^{\infty} S_\lambda d\lambda} \qquad \text{(G-4)}$$

If we consider equal increments of available solar energy, equation (G-4) becomes

$$\alpha_{ZA} = \frac{\Delta S_\lambda}{S} \sum_{\lambda=0}^{\infty} \left[1 - (\rho_{ZA})_\lambda\right] \qquad \text{(G-5)}$$

Using 5% solar energy increments

$$\alpha_{ZA} = 0.05 \sum_{\lambda=0}^{\infty} \left[1 - (\rho_{ZA})_\lambda\right] \qquad \text{(G-6)}$$

However, since the filter is terminated in an optical adhesive with an index of refraction of about 1.52, a resulting increase in thermal absorptance is encountered. This spectral increase in absorptance due to the filter-cell-adhesive interfaces can be represented by A_λ and accounted for as follows:

$$\alpha_{zA} = 0.05 \sum_{\lambda=0}^{\infty} \left[1 - (\rho_{zA})_\lambda\right] (1 + A_\lambda) \qquad \text{(G-7)}$$

which is also used as equation (G-3). A_λ is given by Figure G-1.

Solar energy converted by the solar cell into electricity can be accounted for in the total absorptance in order to obtain a thermal absorptance value. The solar cell conversion efficiency can be represented as follows:

$$\eta_F \cong \frac{\int_0^\infty \tau_\lambda r_\lambda S_\lambda \, d\lambda}{\int_0^\infty S_\lambda \, d\lambda} \qquad \text{(G-8)}$$

where

η_F = photovoltaic conversion efficiency of the filtered solar cell

τ_λ = spectral transmittance of the filter

r_λ = spectral response of the solar cell

The spectral response of the solar cell can be expressed as follows:

$$r_\lambda = (r_\lambda)_{max} \left(\frac{r_\lambda}{r_{\lambda_{max}}} \right) = (r_\lambda)_{max} \, r_\lambda^* \qquad \text{(G-9)}$$

Most solar cell manufacturers define flight quantity cells with a narrow tolerance normalized spectral response and a bare cell conversion efficiency at air mass zero and under 140 mw/cm^2. The bare cell efficiency η_B, can be expressed as:

$$\eta_B = \frac{(r_\lambda)_{max} \int_0^\infty r_\lambda^* S_\lambda d\lambda}{\int_0^\infty S_\lambda d\lambda} \qquad \text{(G-10)}$$

Substituting and re-arranging

$$\eta_F \cong \frac{\eta_B \int_0^\infty \tau_\lambda r_\lambda^* S_\lambda d\lambda}{\int_0^\infty r_\lambda^* S_\lambda d\lambda} \qquad \text{(G-11)}$$

Considering equal wavelength intervals

$$\eta_F \cong \eta_B \frac{\sum_{\lambda=0}^{\infty} \tau_\lambda r_\lambda^* S_\lambda}{\sum_{\lambda=0}^{\infty} r_\lambda^* S_\lambda} \qquad \text{(G-12)}$$

r_λ^* is given by Figure G-2; ρ_λ is given by Figures 5-4, 5-5, and 5-6 for the three filters considered.

Assuming the absorptivity of the periodic multilayers is negligible (considered valid by OCLI), then τ_λ can be determined as follows

$$\tau_\lambda = 1 - \rho_\lambda \qquad \text{(G-13)}$$

The bare cell efficiency, η_B, is essentially linearly temperature dependent. Current Hoffman empirical data indicates η_B may be represented as

$$\eta_B = 0.10 \left[1 - 5.45 \times 10^{-3} \, (T - 301^\circ K)\right] \qquad \text{(G-14)}$$

It should be noted that the bare cell efficiency approaches zero at $484^\circ K$ if a reasonable extrapolation of linear test data is made.

Equation (6-4) obtains directly from equations (G-12) and (G-13).

APPENDIX H

DETERMINATION OF VOLTAGE-CURRENT CURVES

This appendix presents an outline of the method by which the voltage-current curves were developed for various cell-filter combinations. Calculations are presented in tabular form.

Figure H-1 is a typical V-I curve for a single 10% efficient Hoffman silicon N/P solar cell. These data apply exactly to the present study when losses in wiring, connections, etc., are 0.7%.

The V-I data are for 28°C, and are corrected for temperature effects using the data from Figure H-2. Thus,

$$(I_{sc})_T = \frac{(I_{sc})_T}{(I_{sc})_{28}} \; (I_{sc})_{28} = I_{sc}^* \; (I_{sc})_{28} \qquad \text{(H-1)}$$

$$(I_{mp})_T = \frac{(I_{mp})_T}{(I_{mp})_{28}} \; (I_{mp})_{28} = I_{mp}^* \; (I_{mp})_{28} \qquad \text{(H-2)}$$

$$(V_{oc})_T = \frac{(V_{oc})_T}{(V_{oc})_{28}} \; (V_{oc})_{28} = V_{oc}^* \; (V_{oc})_{28} \qquad \text{(H-3)}$$

$$(V_{mp})_T = \frac{(V_{mp})_T}{(V_{mp})_{28}} \; (V_{mp})_{28} = V_{mp}^* \; (V_{mp})_{28} \qquad \text{(H-4)}$$

where the subscript refers to the cell temperature (^{o}C) and I_{sc}*, I_{mp}*, V_{oc}*, V_{mp}*, $(I_{sc})_{28}$, $(I_{mp})_{28}$, $(V_{oc})_{28}$, and $(V_{mp})_{28}$ are given (Figures H-2 and H-1).

A voltage-current curve was obtained for the solar array with each of the three filters considered and at solar distances of 1.0, 0.4, and 0.2 AU. The calculation is illustrated by example below for filter 1 and solar distances of 1.0 and 0.2 AU.

Beginning with filter 3 and a solar distance of 1 AU, we obtain a temperature at the maximum power point (Figures 6-5 and 6-8).

$$T @ \mathcal{P}_{max} = 580^{o}R = 322^{o}K = 49^{o}C$$

From Figures H-1 and H-2 it follows that, for a single cell

$$I_{sc} = 1.0 \ (I_{sc})_{28}$$

$$= (1.0) \ (62.8) = 62.8 \text{ ma}$$

$$I_{mp} = 0.98 \ (I_{mp})_{28}$$

$$= 0.98 \ (57) = 55.8 \text{ ma}$$

$$V_{oc} = 0.91(V_{oc})_{28}$$

$$= 0.91(545) = 495 \text{ mv}$$

$$V_{mp} = 0.89 \ (V_{mp})_{28}$$

$$= 0.89 \ (445) = 396 \text{ mv}$$

To obtain values for entire array, notice that the cells are arranged in series strings of 54. Thus,

$$(V_{oc})_{Total} = 54\ V_{mp}$$
$$= (54)(0.485) = \underline{26.8\ \text{Volts}}$$

$$(V_{mp})_{Total} = 54\ V_{mp}$$
$$= (54)(0.396) = \underline{21.4\ \text{Volts}}$$

At 1 AU the maximum power is 72 watts. Thus,

$$(I_{mp})_{Total} = \frac{P_{max}}{V} = \frac{72}{21.4} = \underline{3.36\ \text{amps}}$$

The short-circuit current is obtained as follows:

$$(I_{sc})_{Total} = \left(\frac{I_{sc}}{I_{mp}}\right)_{single\ cell} (I_{mp})$$

$$= \left(\frac{62.8}{55.8}\right)(3.36) = \underline{3.72\ \text{amps}}$$

Calculations at solar distances other than 1 AU are somewhat different since the data of Figure H-1 are specifically for a solar intensity corresponding to 1 AU. This is illustrated below with filter 3 at 0.2 AU.

$T @ P_{max} = 580^{\circ}R = 322^{\circ}K = 49^{\circ}C$

$I_{sc} = (1.01)(62.8) = 63.5$ ma

$I_{mp} = (0.95)(57) = 54.1$ ma

$V_{oc} = (0.74)(545) = 403$ mv

$V_{mp} = (0.74)(455) = 337$ mv

The above values apply at 1 AU with the temperature corresponding to the 0.2 AU maximum power point. Voltages are functions only of temperature, hence,

$$(V_{oc})_{\text{Total, 0.2 AU}} = (54)(0.403) = \underline{21.8 \text{ Volts}}$$

$$(V_{mp})_{\text{Total, 0.2 AU}} = (54)(0.337) = \underline{16.8 \text{ Volts}}$$

Current is a function of the incident solar intensity. This is reflected in the increased power output of the solar array. Thus,

$$P_{max} \text{ @ 0.2 AU} = 325 \text{ Watts}$$

and

$$(I_{mp})_{\text{Total, 0.2 AU}} = \frac{325}{16.8} = \underline{19.3 \text{ amps}}$$

As before,

$$(I_{sc})_{\text{Total, 0.2 AU}} = \frac{63.5}{54.1} (19.3) = \underline{22.4 \text{ amps}}$$

Table H-1 summarizes the V-I calculations for all of the cases considered, including results. These results are plotted in Figures 6-13, 6-14, and 6-15.

FIGURE H-1

TYPICAL VOLTAGE vs. CURRENT CURVE

HOFFMAN 10% EFFICENT N/P SILICON SOLAR CELL

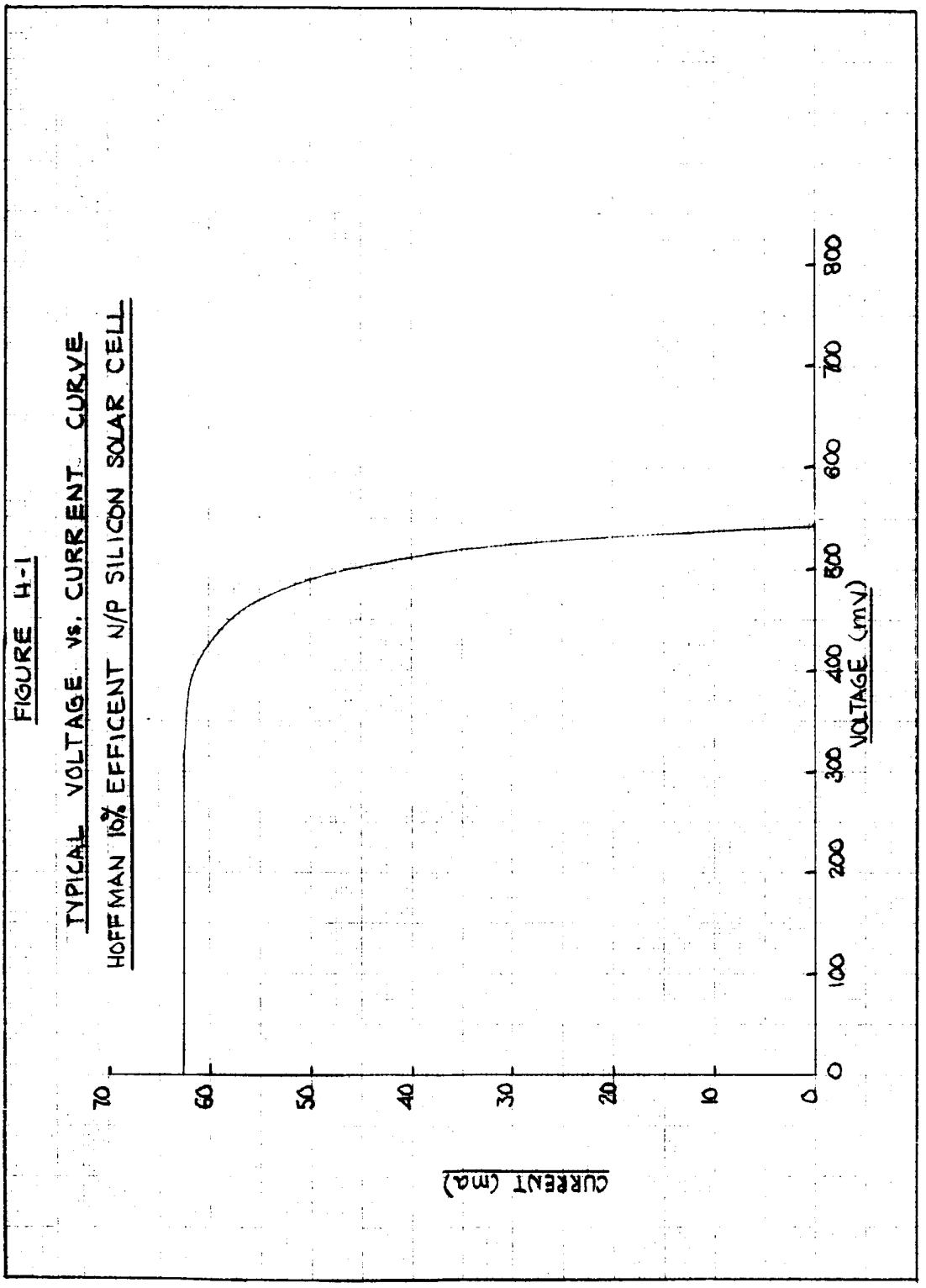

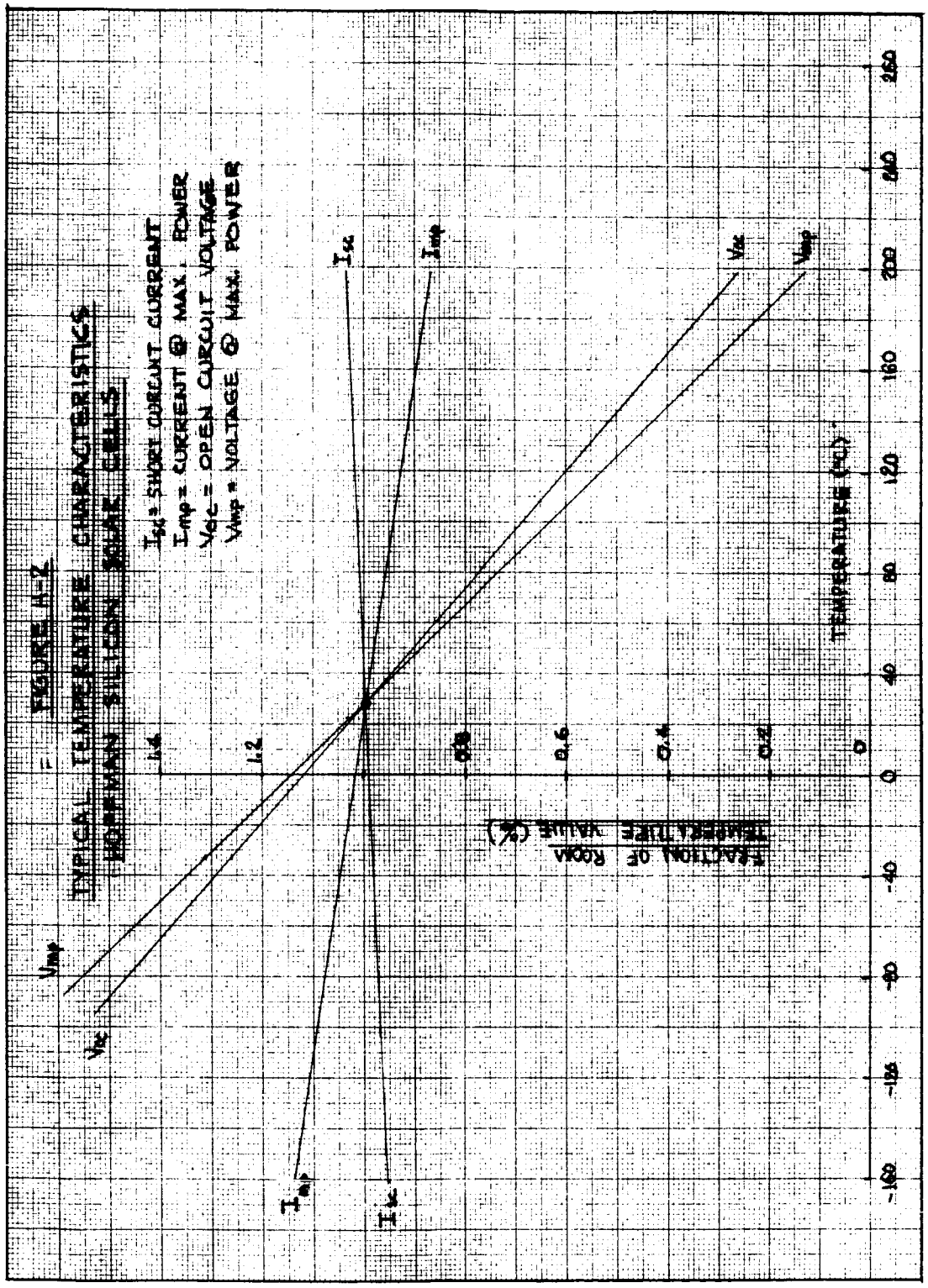
FIGURE H-2
TYPICAL TEMPERATURE CHARACTERISTICS
HOFFMAN SILICON SOLAR CELLS
I_{sc} = SHORT CIRCUIT CURRENT
I_{mp} = CURRENT @ MAX. POWER
V_{oc} = OPEN CIRCUIT VOLTAGE
V_{mp} = VOLTAGE @ MAX. POWER
FRACTIONAL OF ROOM TEMPERATURE VALUE (%)
TEMPERATURE (°C)
1.4
1.2
1.0
0.8
0.6
0.4
0.2
0
-40
-80
-120
-160
200
160
120
80
40
0
I_{mp}
I_{sc}
V_{mp}
V_{oc}

TABLE H-1

CALCULATION OF VOLTAGE-CURRENT CURVES

FILTER	AU	P_{MAX} (WATTS)	TEMP @ P_{MAX} °R	TEMP @ P_{MAX} °C	I_{sc}^*	I_{mp}^*	V_{oc}^*	V_{mp}^*	V_{oc} (VOLTS)	V_{mp} (VOLTS)	I_{mp} SINGLE CELL (mA)	I_{mp} TOTAL ARRAY (A)	I_{sc} SINGLE CELL (mA)	I_{sc} TOTAL ARRAY (A)
1	0.2	275	600	61	1.0	0.97	0.85	0.83	25	19.9	55.2	13.8	62.8	15.7
	0.4	152	580	49	1.0	0.98	0.91	0.89	26.8	21.4	55.8	7.1	62.8	7.98
	1.0	60	490	-1	1.0	1.0	1.0	1.0	29.4	24	57	2.5	62.8	2.76
2	0.2	253	640	83	1.01	0.95	0.76	0.73	22.3	17.5	54.1	14.5	63.5	17
	0.4	150	600	61	1.0	0.97	0.85	0.83	25	19.9	55.2	7.5	62.8	8.54
	1.0	53	430	-34	0.98	1.04	1.26	1.32	37	31.7	59.2	1.67	61.5	1.73
3	0.2	325	650	88	1.01	0.95	0.74	0.70	21.8	16.8	54.1	19.3	63.5	22.4
	0.4	175	600	61	1.0	0.97	0.85	0.83	25	19.9	55.2	8.8	62.8	10
	1.0	72	580	49	1.0	0.98	0.91	0.89	26.8	21.4	55.8	3.36	62.8	3.72